UAB
Universitat Autònoma de Barcelona

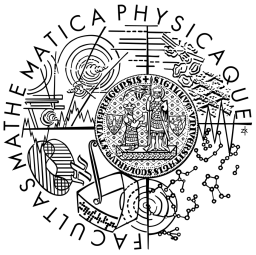
Design and characterisation of topologically protected photonic edge modes

Ondřej Novák

ADVERTIMENT. L'accés als continguts d'aquesta tesi queda condicionat a l'acceptació de les condicions d'ús establertes per la següent llicència Creative Commons:  https://creativecommons.org/licenses/?lang=ca

ADVERTENCIA. El acceso a los contenidos de esta tesis queda condicionado a la aceptación de las condiciones de uso establecidas por la siguiente licencia Creative Commons:  https://creativecommons.org/licenses/?lang=es

WARNING. The access to the contents of this doctoral thesis it is limited to the acceptance of the use conditions set by the following Creative Commons license:  https://creativecommons.org/licenses/?lang=en



FACULTY
OF MATHEMATICS
AND PHYSICS
Charles University

DOCTORAL THESIS

RNDr. Ondřej Novák

Design and characterisation of topologically protected photonic edge modes

Institute of Physics

Supervisor of the doctoral thesis: RNDr. Martin Veis, Ph.D.
Gervasi Herranz, Ph.D.

Study programme: Quantum Optics and Optoelectronics

Prague 2025

I declare that I carried out this doctoral thesis on my own, and only with the cited sources, literature and other professional sources. I understand that my work relates to the rights and obligations under the Act No. 121/2000 Sb., the Copyright Act, as amended, in particular the fact that the Charles University has the right to conclude a license agreement on the use of this work as a school work pursuant to Section 60 subsection 1 of the Copyright Act.

In ..... date ....

Author's signature

To Martin Veis and Gervasi Herranz, for guiding the light of my curiosity, and to my loved ones, for being its constant source.

Title: Design and characterisation of topologically protected photonic edge modes

Author: RNDr. Ondřej Novák

Institute: Institute of Physics

Supervisor: RNDr. Martin Veis, Ph.D.
Gervasi Herranz, Ph.D., Institute of Physics,
Institute of Materials Science of Barcelona

Abstract: This thesis presents a complete framework for designing and characterizing topologically protected interface modes in two-dimensional photonic crystals. The work introduces automated tools for band connection and eigenmode symmetry classification that ensure consistent identification of topological transitions across complex parameter spaces. Using these methods, the thesis demonstrates the formation of interface-localized modes arising from the obstructed atomic limit in a C_4-symmetric dielectric lattice, realized in indium phosphide at telecommunication wavelengths. The results show that these modes originate from a mismatch in Wannier center positions, remain confined within few lattice periods, and exhibit robustness to structural defects. The study further quantifies the trade-off between mode dispersion and band-gap size and identifies the minimum number of unit cells required for stable, unidirectional transport. The proposed generative approach to geometry design establishes a foundation for data-driven inverse methods in topological photonics. The developed framework enables scalable, fully automated, and fabrication-compatible design of symmetry-protected photonic interfaces for integrated optical platforms.

Keywords: Photonic Crystal, Topological Photonics, OAL, Integrated Photonics, Eigenmode Symmetry

Název práce: Návrh a charakterizace topologicky chráněných fotonických rozhranních módů

Autor: RNDr. Ondřej Novák

Ústav: Fyzikální ústav Univerzity Karlovy

Vedoucí bakalářské práce: RNDr. Martin Veis, Ph.D.
Gervasi Herranz, Ph.D., Fyzikální ústav Univerzity Karlovy,
Institut de Ciència de Materials de Barcelona

Abstrakt: Tato disertační práce představuje ucelený rámec pro návrh a charakterizaci topologicky chráněných rozhraní v dvojrozměrných fotonických krystalech. Práce zavádí automatizované nástroje pro budování pásové struktury a klasifikaci symetrií vlastních módů, které zajišťují konzistentní identifikaci topologických přechodů v komplexních parametrických prostorech. Pomocí těchto metod je demonstrována tvorba rozhraním lokalizovaných módů vznikajících z obstructed atomic limitu v C_4-symetrické dielektrické mříži realizované v fosfidu india při telekomunikačních vlnových délkách. Výsledky ukazují, že tyto módy vznikají z nesouladu v pozicích Wannierových center, zůstávají lokalizované v rámci několika elementárních buněk a vykazují odolnost vůči strukturálním poruchám. Studie dále kvantifikuje kompromis mezi disperzí módu a velikostí zakázaného pásma a určuje minimální počet elementárních buněk potřebný pro stabilní jednosměrný přenos. Navržený generativní přístup k návrhu geometrie vytváří základ pro datově řízené inverzní metody v topologické fotonice. Vyvinutý rámec umožňuje škálovatelný, plně automatizovaný a technologicky kompatibilní návrh symetrií chráněných fotonických rozhraní pro integrované optické platformy.

Klíčová slova: Fotonické Krystaly, Topologická Fotonika, OAL, Integrovaná Fotonika, Symetrie Vlastních Módů

Contents

I Theoretical background **7**

1 Introduction **8**
1.1 Photonic Eigen-problem 9
1.2 Types of photonic topology 11
1.2.1 Chern topology 11
1.2.2 Valley-Chern topology 15
1.2.3 Obstructed Atomic Limit 17
1.3 Current state of the art 17

2 Simulation techniques **20**
2.1 MIT photonic bands 20
2.1.1 MPB bandstructure 25
2.1.2 MPB eigenmodes 27
2.1.3 MPB interface 28
2.2 FDTD method 30
2.2.1 FDTD in topological simulations 32
2.2.2 FDTD transmission simulation 33
2.2.3 FDTD bandstructure simulations 35

II Research findings **39**

3 Exploration of Chern Topologies for IR Photonics **40**
3.1 Band connection procedure 41
3.1.1 The need for the automated band connection 41
3.1.2 Algorithm for automated band connection 42
3.2 Problem of scale 46
3.2.1 Material parameter scan around a reference Chern crystal 47
3.2.2 Effect of field–material overlap 47
3.2.3 Metamaterials as an alternative route 49
3.2.4 Shift of focus to dielectric topological platforms 49

4 Automated Detection of Band-Symmetry Inversions **52**
4.1 Band-symmetry recognition procedure 52
4.1.1 Amplitude invariance via the sign function 53
4.1.2 Comparator-based mode recognition 53
4.1.3 Predefined comparators from group theory 54
4.1.4 Comparator generation from the dataset 54
4.1.5 Identifying band-symmetry inversion 54

5 Search for Eigenmode Inversions in C_4 Lattices **56**
5.1 Early versions of the mode clasification 61
5.2 Unit cell design 62
5.3 Lattice-parameter matching using fractional ratios in photonic crystals 71
5.4 Generative geometry approach to unit-cell design 73

5.4.1 Mathematical formulation 74
5.4.2 Algorithmic implementation 75
5.4.3 Results and limitations 76

6 Topological modes characterization **77**
6.1 Classifying the type of topological modes 80
6.2 Edge modes vs boundary size 82
6.3 Defect states 89
6.4 Band-gap vs mode dispersion 94

Conclusion **97**

Bibliography **100**

List of Figures **109**

List of Abbreviations **119**

List of Publications **120**

Part I

Theoretical background

1 Introduction

In material science, topology revolves around establishing and preserving a certain invariant that remains unchanged under adiabatic modifications, such as reshaping the system's geometry, provided the band gap does not close. This conserved invariant ensures the appearance of compensation states at the boundary where the topological system meets a non-topological one, thereby guaranteeing robust interface modes.

Topology in material sciences and photonics relies on the notion of a topological invariant [1, 2, 3], a mathematical quantity that remains unchanged under adiabatic alterations of a system's parameters [4, 5]. Adiabatic in this case means, that no band-gap in the system (atomic or photonic) is closed or reopened [6]. Examples of such alterations include reshaping or deforming the lattice structure or the crystal unit cell. The unchanging nature of the topological invariant ensures that a system, once in a specific topological phase, stays in that phase unless it passes through a band-gap closure, which signifies a topological phase transition.

One of the most compelling consequences of having a non-trivial topological invariant is the appearance of boundary states at the interface between a topological system and a system with a different or trivial topology [7, 8]. This phenomenon is commonly referred to as the bulk-boundary correspondence. By virtue of the topological mismatch at the interface, localized states necessarily emerge in the gap, effectively "compensating" for the disparity in topological invariants across the boundary. These interfacial modes are typically protected against certain types of disorder, scattering, or imperfections that would otherwise disrupt wave propagation in conventional materials [9, 10, 11, 12].

Although the essential concepts of topological invariants and boundary-state protection remain consistent, many nuanced variations have been explored. Quantum Hall systems, for instance, rely on an integer Chern number that arises when time-reversal symmetry is broken [13], while quantum spin [14] or valley Hall [15, 16] systems preserve time-reversal symmetry and employ other topological indices like the $\mathbb{Z}_2$ invariant or valley Chern numbers. Higher-order topological phases extend these principles by hosting states localized at corners or hinges, rather than at edges [17, 18], and non-Hermitian topological phases incorporate the effects of gain and loss, altering how invariants and edge states manifest [19]. Despite these differences, the unifying principle is that a robust, gap-preserving topological invariant underpins the stable, often one-way boundary or interface modes that make topological materials and photonic systems so promising for practical applications in waveguiding, spintronics, and quantum information processing.

In this chapter, we lay the foundation for the concepts addressed in this work. Since each type of topology requires a slightly different mathematical formulation, we will begin by examining Chern topology, the earliest observed topological phenomenon, and from there, expand our discussion to include Obstructed atomic limit (OAL) topological phases as well as Valley-Chern topology.

We will focus on two-dimensional systems, where the interface of the structure defines a line suitable for wire-like applications. Photonic crystals serve as our

chosen platform for topological design because they closely resemble atomic crystals, in which the Hall and spin-Hall effects were originally discovered.

1.1 Photonic Eigen-problem

Suppose the system under investigation is a two-dimensional photonic crystal composed of linear, isotropic, lossless, and dispersionless materials with no charges. Under these assumptions, the propagation of electromagnetic waves within the crystal is governed by Maxwell's equations:

$$\begin{aligned} \operatorname{rot} \boldsymbol{H} - \partial_t \boldsymbol{D} &= 0 \\ \operatorname{div} \boldsymbol{D} &= 0 \\ \operatorname{rot} \boldsymbol{E} + \partial_t \boldsymbol{B} &= 0 \\ \operatorname{div} \boldsymbol{B} &= 0 \end{aligned} \tag{1.1}$$

Assuming a time-harmonic dependence of the form $\mathbf{E}(\mathbf{r}, t) = \mathbf{E}(\mathbf{r})e^{-i\omega t}$ and $\mathbf{H}(\mathbf{r}, t) = \mathbf{H}(\mathbf{r})e^{-i\omega t}$, and applying the usual constitutive relations ($\mathbf{D} = \epsilon_0 \varepsilon_r \mathbf{E}$, $\mathbf{B} = \mu_0 \mu_r \mathbf{H}$), while working with non-magnetic media, thus $\mu_r = 1$ the Maxwell equations reduce to:

$$\operatorname{rot} \boldsymbol{H}(\boldsymbol{r}) + i\omega\varepsilon_0\varepsilon_r(\boldsymbol{r})\, \boldsymbol{E}(\boldsymbol{r}) = 0, \tag{1.2}$$

$$\operatorname{div} \Big[\varepsilon(\boldsymbol{r})\, \boldsymbol{E}(\boldsymbol{r})\Big] = 0, \tag{1.3}$$

$$\operatorname{rot} \boldsymbol{E}(\boldsymbol{r}) - i\omega\mu_0\, \boldsymbol{H}(\boldsymbol{r}) = 0, \tag{1.4}$$

$$\operatorname{div} \boldsymbol{H}(\boldsymbol{r}) = 0. \tag{1.5}$$

Plugging 1.4 into 1.2 and using the definition of the speed of light in vacuum, $c = (\varepsilon_0\, \mu_0)^{-\frac{1}{2}}$, yields a wave equation for $\boldsymbol{H}$. Conversely, substituting 1.2 into 1.4 produces the corresponding wave equation for $\boldsymbol{E}$.

$$\nabla \times \left[\frac{1}{\varepsilon_r(\boldsymbol{r})} \nabla \times \boldsymbol{H}(\boldsymbol{r})\right] = \left(\frac{\omega}{c}\right)^2 \boldsymbol{H}(\boldsymbol{r}), \tag{1.6}$$

$$\nabla \times \nabla \times \boldsymbol{E}(\boldsymbol{r}) = \left(\frac{\omega}{c}\right)^2 \varepsilon_r(\boldsymbol{r})\, \boldsymbol{E}(\boldsymbol{r}). \tag{1.7}$$

Note that $\boldsymbol{r}$ is a real-space coordinate within the elementary cell. Equation 1.6 is commonly used to derive the system's eigenmodes because it takes the form of an eigenproblem [20]. The fields $\boldsymbol{E}$ and $\boldsymbol{H}$ remain vectorial here, but because we are dealing with two-dimensional systems, the Maxwell equations decouple into transverse electric (TE) and transverse magnetic (TM) modes, owing to the lack of variation in the z direction [21]. The equations for TE modes involve only (E_x, E_y, H_z), while those for TM modes involve (H_x, H_y, E_z). Consequently, Equation 1.6 reduces to a scalar equation for TE modes, since the only nonzero component of the magnetic field is H_z. The same applies to Equation 1.7 in the TE case, where the only variable is E_z.

Solving Equation 1.7 directly is more difficult because it is not a Hermitian eigenvalue problem but rather a generalized eigenvalue equation, due to the presence of $\varepsilon_r(\boldsymbol{r})$ on the right-hand side [20]. It is therefore more straightforward to solve Equation 1.6 to obtain the eigenmodes and then retrieve the electric field from the magnetic field.

For TE modes, Equation 1.6 reduces to:

$$\hat{\boldsymbol{A}}(\boldsymbol{r})H_z(\boldsymbol{r}) = \hat{a}H_z(\boldsymbol{r}) \tag{1.8}$$

$$\hat{\boldsymbol{A}}(\boldsymbol{r})[\#] = \nabla \times \left[\frac{1}{\varepsilon_r(\boldsymbol{r})}\nabla \times \#\right] \tag{1.9}$$

$$\hat{a} = \left(\frac{\omega}{c}\right)^2 \tag{1.10}$$

The equation 1.8 is clearly an eigenproblem for the operator $\hat{\boldsymbol{A}}(\boldsymbol{r})$ with eigenvalues $\hat{a}$. We use $\hat{a}$ to avoid confusion when introducing the lattice parameter a. Since $\varepsilon_r(\boldsymbol{r})$ is periodic with period $\boldsymbol{a}_u$, the lattice constant of the photonic crystal (PC) elementary cell, $\hat{\boldsymbol{A}}(\boldsymbol{r})$ also inherits this periodicity. As a result, the solution $H_z(\boldsymbol{r})$ must likewise be periodic with period $\boldsymbol{a}_u$.

$$H_z(\boldsymbol{r}) = H_z(\boldsymbol{r} + \boldsymbol{a}_u), \tag{1.11}$$

which means, that the solution can be written in a form of Bloch function, using the Bloch theorem [22]:

$$H_{z,\boldsymbol{k}}(\boldsymbol{r}) = e^{i\boldsymbol{k}\cdot\boldsymbol{r}}u_{\boldsymbol{k}}(\boldsymbol{r}), \tag{1.12}$$

where $\boldsymbol{k}$ is the reciprocal-space vector that indexes the solution, and $u_{\boldsymbol{k}}(\boldsymbol{r})$ is a function that shares the periodicity of the photonic crystal's unit cell $\boldsymbol{a}_u$. Solving Equation 1.8 with a solution of the form described in equation 1.12 for a given $\boldsymbol{k}$ yields a set of eigenvalues that vary continuously as $\boldsymbol{k}$ changes, thereby forming the photonic band structure [23].

Nevertheless, the more crucial aspect for this thesis lies in the periodic function $u_{\boldsymbol{k}}(\boldsymbol{r})$. As an eigenstate corresponding to a particular eigenvalue, the symmetry properties of $u_{\boldsymbol{k}}(\boldsymbol{r})$, along with its evolution throughout the Brillouin zone, determine the topological character of the system.

The periodical function $u_{\boldsymbol{k}}(\boldsymbol{r})$ is in this work obtained by MIT photonic bands (MPB) [24], which is a commonly used tool in the literature. We also use the Finite Difference Time Domain (FDTD) method [25, 26, 27] since in contrast to MPB can deal with materials with loss, but is significantly more difficult and expensive to use. Another tool commonly used in literature, but not in thesis is COMSOL multiphysics [28].

An example of the eigenvalues obtained as a solution to Eq. 1.8 using MPB is shown in Figure 1.1. Equation 1.8 is solved for $\boldsymbol{k}$ vectors along the $\Gamma - K - M - \Gamma$ path in the Brillouin zone. The dots represents eigenvalues $\hat{a}$. In this example, the photonic crystal consists of a set of rods arranged in a two-dimensional triangular lattice. We used a relative permittivity of $\varepsilon_r = 10$ and a rod radius of $r_{\text{rod}} = 0.3075 \cdot a$, where a is the lattice period. The specific value of r_{rod} is arbitrary.

Notably, the units on the y-axis are scaled by the lattice parameter a, and the frequency is expressed as $\frac{\omega a}{2\pi c} = \frac{a}{\lambda}$, a common convention for representing the energy axis in photonic band structures. This representation is particularly convenient because it allows the targeted wavelength for a given application to be adjusted simply by tuning the lattice parameter, provided that the material parameters remain sufficiently close to their original values.

The thick blue bands indicate regions where no solutions exist for Eq. 1.8, corresponding to photonic band-gap regions.

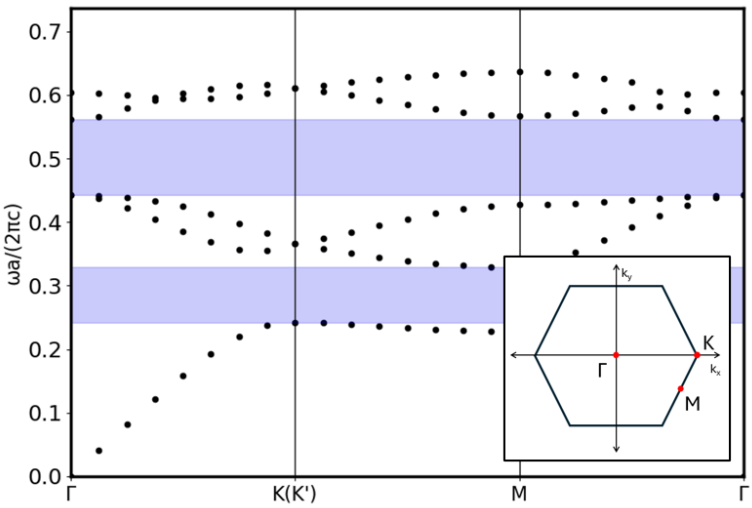


Figure 1.1 An example of an unconnected photonic band structure obtained using MPB is shown for a system of rods arranged in a triangular lattice with a relative permittivity of $\varepsilon = 10$ and a rod radius of $r_{\text{rod}} = 0.3075 \cdot a$. The calculation is performed for TM modes for the first five eigenvalues.

1.2 Types of photonic topology

In the following sections, we will discuss various types of topologically protected edge states and the underlying mechanisms. A key characteristic of topological protection is that it is not a local phenomenon. Local disturbances do not affect these modes. This implies that the entire geometry of the photonic crystal contributes to the formation of topological modes. However, the only region where the mode manifests is at the edge of the photonic crystal. This edge can interface either another photonic crystal that is topologically trivial or another topologically trivial system. An example of this configuration is depicted in Figure 1.2.

1.2.1 Chern topology

Chern topology is defined by a topological invariant known as the *Chern number* [29], which characterizes individual bands within the photonic band structure.

If there is a difference in Chern numbers around a photonic band gap, a surface chiral mode is created to compensate for this difference [30]. This behavior mimics the quantum Hall effect [31], as shown in Figure 1.3a.

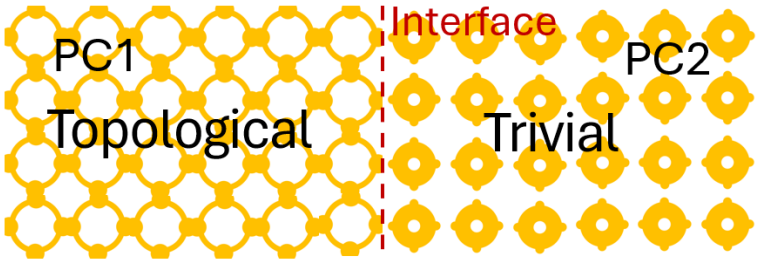


Figure 1.2 Interface between the topological and trivial photonic crystal

Since time-reversal symmetry is broken for this mode, meaning there is no counter-propagating mode, the resulting propagation is unidirectional. This unidirectional propagation is illustrated in Figure 1.3b.

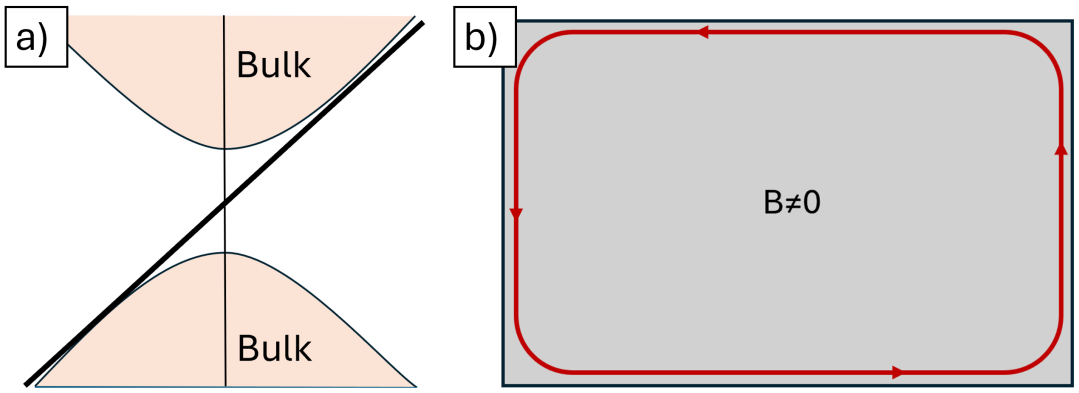


Figure 1.3 **a)** An illustration of a band structure in a quantum Hall system showing a single gapless edge mode. **b)** An illustration of a two-dimensional electron system with an external magnetic field, which induces a chiral edge state by breaking time-reversal symmetry.

To compute the Chern number for a photonic system, it is first essential to define the *Berry phase* and *Berry curvature*. The Berry phase, also known as the Berry–Pancharatnam–Zak phase, is a geometric phase acquired by an eigenstate during adiabatic evolution along a closed path γ in reciprocal space [20, 32, 4, 33, 34].

The Berry phase is typically defined through the *Berry connection* $\boldsymbol{A}_n(\boldsymbol{k})$, where the index n denotes the band:

$$\boldsymbol{A}_n(\boldsymbol{k}) = i \langle u_{n,\boldsymbol{k}} | \nabla_{\boldsymbol{k}} | u_{n,\boldsymbol{k}} \rangle \tag{1.13}$$

Following the procedure outlined in the referenced literature, the Berry phase can be expressed as:

$$\phi_{n,\gamma} = \oint_{\gamma} \boldsymbol{A}_n(\boldsymbol{k}) \cdot d\boldsymbol{k} = \iint_{S(\gamma)} \left[\nabla_{\boldsymbol{k}} \times \boldsymbol{A}_n(\boldsymbol{k})\right] ds = \iint_{S(\gamma)} \boldsymbol{\Omega}_n(\boldsymbol{k}) ds, \tag{1.14}$$

where $\boldsymbol{\Omega}_n(\boldsymbol{k})$ represents the Berry curvature of the n-th band at a specific $\boldsymbol{k}$ point, and $S(\gamma)$ denotes the surface enclosed by the closed path γ around the k

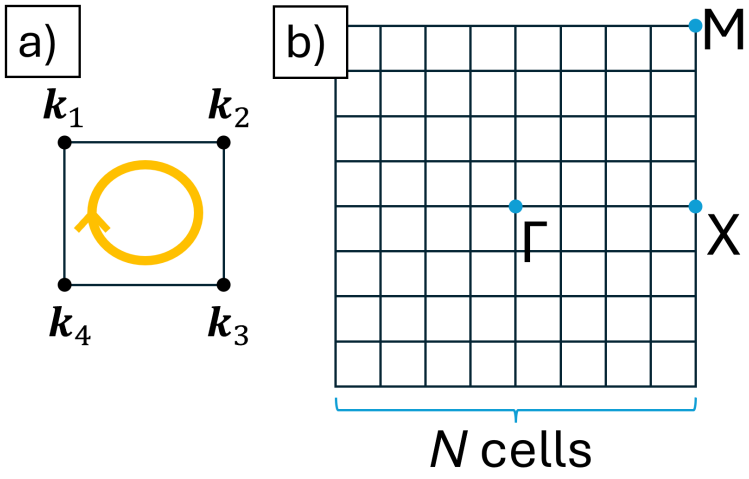


Figure 1.4 Discretization of the Brillouin zone for Berry phase calculations. **a)** A single plaquette, whose edges define the path γ. **b)** Discretization of the Brillouin zone into an $N \times N$ grid of plaquettes.

point. The Stokes theorem [35] is applied to transform the path integral into a surface integral.

The Chern number is then determined as the total Berry curvature integrated over the entire Brillouin zone [36, 37]:

$$C_n = \frac{1}{2\pi} \iint_{BZ} \boldsymbol{\Omega}_n(\boldsymbol{k}) d\boldsymbol{k} \tag{1.15}$$

The periodic functions $u_{n,\boldsymbol{k}}$ at specific k-points can be efficiently computed using MPB. However, performing direct closed-path integration is impractical. Blanco de Paz [20] proposed an elegant solution by discretizing the Brillouin zone using an orthogonal grid, which forms rectangular plaquettes that serve as the surfaces S enclosed by the closed paths γ.

Consider one such plaquette with corner positions $[\boldsymbol{k}_1, \boldsymbol{k}_2, \boldsymbol{k}_3, \boldsymbol{k}_4]$ as depicted in figure 1.4a. The Berry phase associated with the path enclosing this plaquette can then be expressed as:

$$\phi = -\Im \log \left[\langle u_{\boldsymbol{k}_1}(\boldsymbol{r}) | u_{\boldsymbol{k}_2}(\boldsymbol{r}) \rangle \langle u_{\boldsymbol{k}_2}(\boldsymbol{r}) | u_{\boldsymbol{k}_3}(\boldsymbol{r}) \rangle \langle u_{\boldsymbol{k}_3}(\boldsymbol{r}) | u_{\boldsymbol{k}_4}(\boldsymbol{r}) \rangle \langle u_{\boldsymbol{k}_4}(\boldsymbol{r}) | u_{\boldsymbol{k}_1}(\boldsymbol{r}) \rangle \right] \tag{1.16}$$

The imaginary part of the logarithm is used to extract the phase of the complex notation. The bracket notation represents the scalar products of the periodic functions, scaled by the size of the plaquette:

$$\langle u_{\boldsymbol{k}_1}(\boldsymbol{r}) | u_{\boldsymbol{k}_2}(\boldsymbol{r}) \rangle = \sum_{i,j} u^*_{k_1}(i,j) u_{k_2}(i,j) S \tag{1.17}$$

,

where the indices i, j represent the real-space coordinates at which the periodic function is evaluated. Since the periodic function obtained from MPB is already discretized in real space, these indices correspond to the discrete sampling points within the computational domain.

The Chern number is then obtained by summing the Berry phases of all plaquettes within the Brillouin zone:

$$C_n = \frac{1}{2\pi} \sum_{j \in BZ} \phi_{j,n} \tag{1.18}$$

The Chern number takes integer values and becomes nonzero when time-reversal symmetry (TRS) is broken, typically due to the presence of a magnetic field.

The Chern number directly predicts the existence of topologically protected edge modes, analogous to those observed in the quantum Hall effect. Consider a photonic crystal with a photonic band gap bounded by two isolated bands that do not intersect any others, and place the PC in air. If these two bands exhibit nontrivial topology, characterized by a nonzero Chern number, topologically protected edge modes will emerge at the interface within the band gap. The number of such edge modes is given by the absolute value of the difference between the Chern numbers of the two bands.

A challenge arises when bands near the band gap of interest are intersected by other bands. In such cases, the Chern number must be computed for the entire system of intersecting bands rather than for individual bands. This issue is addressed in [38, 39], where the degeneracies introduced by band crossings are resolved by employing overlap matrices. These matrices are incorporated into a modified Berry phase formulation:

$$\phi_{cross} = -\Im \log \left[\det(S_{\boldsymbol{k}_1\boldsymbol{k}_2} S_{\boldsymbol{k}_2\boldsymbol{k}_3} S_{\boldsymbol{k}_3\boldsymbol{k}_4} S_{\boldsymbol{k}_4\boldsymbol{k}_1}) \right], \tag{1.19}$$

where the $n \times n$ overlap matrices $S_{\boldsymbol{k}\boldsymbol{k}'}$ are defined as:

$$S_{\boldsymbol{k}\boldsymbol{k}'} = \begin{pmatrix} \langle u^1_{\boldsymbol{k}}(\mathbf{r}) \mid u^1_{\boldsymbol{k}'}(\mathbf{r}) \rangle & \langle u^1_{\boldsymbol{k}}(\mathbf{r}) \mid u^2_{\boldsymbol{k}'}(\mathbf{r}) \rangle & \cdots & \langle u^1_{\boldsymbol{k}}(\mathbf{r}) \mid u^n_{\boldsymbol{k}'}(\mathbf{r}) \rangle \\ \langle u^2_{\boldsymbol{k}}(\mathbf{r}) \mid u^1_{\boldsymbol{k}'}(\mathbf{r}) \rangle & \langle u^2_{\boldsymbol{k}}(\mathbf{r}) \mid u^2_{\boldsymbol{k}'}(\mathbf{r}) \rangle & \cdots & \langle u^2_{\boldsymbol{k}}(\mathbf{r}) \mid u^n_{\boldsymbol{k}'}(\mathbf{r}) \rangle \\ \vdots & \vdots & \ddots & \vdots \\ \langle u^n_{\boldsymbol{k}}(\mathbf{r}) \mid u^1_{\boldsymbol{k}'}(\mathbf{r}) \rangle & \langle u^n_{\boldsymbol{k}}(\mathbf{r}) \mid u^2_{\boldsymbol{k}'}(\mathbf{r}) \rangle & \cdots & \langle u^n_{\boldsymbol{k}}(\mathbf{r}) \mid u^n_{\boldsymbol{k}'}(\mathbf{r}) \rangle \end{pmatrix} \tag{1.20}$$

Another challenge with intersecting bands is detecting them in the first place. When the photonic band structure is computed by solving the eigenvalue equation 1.8 using the Bloch ansatz 1.12, the result is a set of eigenvalues for each wavevector $\boldsymbol{k}$ that is evaluated. To accurately identify band crossings and anticrossings, the eigenvalues must first be correctly connected into continuous bands, which is a nontrivial problem [40]. This issue will be addressed in detail in Section 3.1.

Furthermore, a fundamental limitation of Chern photonic topology is its reliance on the breaking of time-reversal symmetry to generate nontrivial Chern numbers. As a result, it is restricted to magneto-optical materials that exhibit sufficiently strong off-diagonal components in their permeability tensor. However, significant off-diagonal components are typically observed only in the far-infrared to radio-wave region of the spectrum, which imposes constraints on the lattice size of photonic crystals, as it must correlate with the operational wavelength

[41, 42, 43]. Consequently, Chern photonic topology is not readily integrable into miniaturized optical systems and is primarily applicable in specific use cases or fundamental research on topological phenomena. A detailed discussion of these limitations will be provided in Section 3.

The Chern number can be determined by another property called the Wilson loop (or Wannier center flow). The Wilson loop tracks the position of the localized Wannier function across the Brillouin zone. The Wannier function is constructed from the Bloch functions and represents the position of atomic orbitals in solid-state physics or field lobes in photonics.

Starting from the periodic Bloch functions $u_{n\mathbf{k}}(\mathbf{r})$ introduced in Eq.1.12, the Wilson loop operator is constructed as a path-ordered product of overlap matrices along a discrete, closed path in reciprocal space [20]. Specifically, it is computed along the k_x-direction at fixed k_y, forming a closed loop across the Brillouin zone:

$$\mathcal{W}(k_y) = \lim_{N\to\infty} \prod_{j=0}^{N-1} F_{j,j+1}, \quad \text{where} \quad [F_{j,j+1}]_{mn} = \langle u_{m,\mathbf{k}_j} | u_{n,\mathbf{k}_{j+1}} \rangle. \tag{1.21}$$

Here, m, n index the selected bands, and the product is path-ordered in increasing k_x. The overlap matrices $F_{j,j+1}$ capture the parallel transport of Bloch states between neighboring $\mathbf{k}$-points. The Wilson loop operator $\mathcal{W}(k_y)$ has eigenvalues of unit magnitude, $\lambda_i(k_y) = e^{i\theta_i(k_y)}$, with the phases $\theta_i(k_y) \in [-\pi, \pi)$ representing the average positions of the hybrid Wannier centers along the real-space x-direction. Since the Wilson loop is computed over k_x, these phases provide a band-resolved measure of the bulk polarization along x.

The Chern number of a given band or set of bands can then be determined by the number of winding around 2π in a given direction. An example of various Wilson loops is shown in figure 1.5.

1.2.2 Valley-Chern topology

The Valley-Chern insulator is a system that possesses a valley degree of freedom. Unlike the Chern insulator, the total Chern number for all bands is zero, as the system does not break time-reversal symmetry. This removes the need for materials with strong magneto-optical response, which are too lossy at short wavelengths, and therefore allows dielectric implementations that operate in the near-infrared or visible spectral regions. The system typically exhibits opposite spatial modulation in the Berry curvature in specific regions. These regions give the "valley" part of the effect its name, and computing the Chern number of those valleys yields valley Chern numbers $\mathbb{C}_v$, which can take integer and half-integer values [20].

A canonical example of this effect in photonics is a design by Ma and Shvets [15], where the authors introduced a design based purely on silicon. In this case, the valleys are centered around the **K** and **K'** points. The idea in the paper is that the valley degree of freedom in the graphene-like material, in this case a hexagonal lattice, behaves as a spin-like binary degree of freedom. Specifically, in solid-state physics, the angular rotation of the electron wavefunction in the **K** or **K'** valleys generates an intrinsic magnetic moment that mimics the one

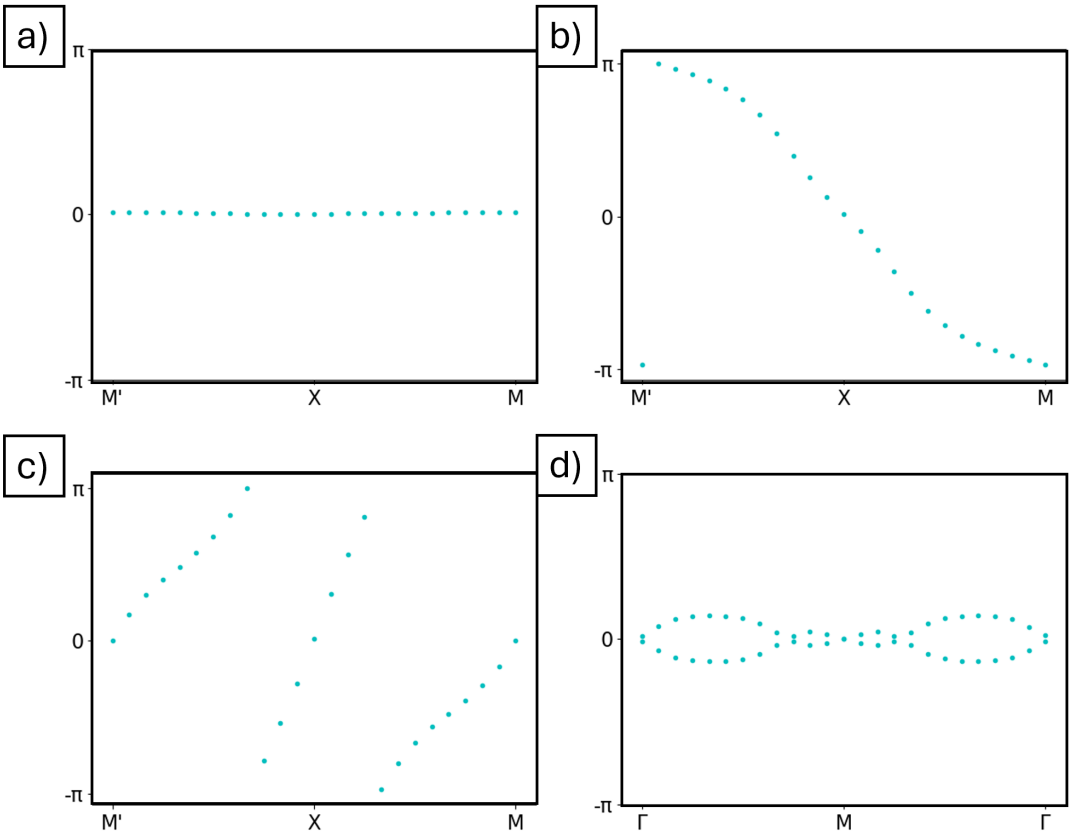


Figure 1.5 Example of Wilson loops. a) Wilson loop of a single trivial band, showing no winding, corresponding to a Chern number $\mathbb{C} = 0$. b) Wilson loop of a topologically non-trivial band where the Wannier centers wind in the negative direction, corresponding to $\mathbb{C} = -1$. c) Wilson loop of a topologically non-trivial band where the Wannier centers wind twice in the positive direction, corresponding to $\mathbb{C} = 2$. d) Wilson loops of a set of two bands, where the Wannier centers are slightly displaced but show no winding, corresponding to $\mathbb{C} = 0$.

produced by the electron spin. This similarity between the valley and spin degrees of freedom makes it possible to observe the quantum valley Hall effect, which is the valley-space counterpart of the quantum spin Hall effect. Therefore, the quantum valley Hall effect produces valley-locked chiral edge states that appear at two PC interfaces and are immune to scattering caused by non-magnetic defects, because each valley has an opposite pseudo-spin and non-magnetic defect scattering is not able to flip this pseudospin (chirality) of the two counterpropagating modes.

The Wilson loops in this case can start winding from the stationary position, but they also unwind, so the total number of π is zero.

Although we do not investigate this kind of system in this work, we mention this topological effect as it is currently very popular, as we demonstrate in section 1.3.

1.2.3 Obstructed Atomic Limit

The obstructed atomic limit represents a slightly different effect in which the resulting Chern numbers are not only zero, but unlike in the Valley-Chern topology, where the Wilson loops are winding yet cancel out, in the obstructed atomic limit there is no winding at all.

The effect can be identified based on the Wilson loop analysis. The Wilson loops of a system in the obstructed atomic limit phase are displaced around $\pm\pi$ and do not wind. This indicates that the Wannier centers (the lobes of the electromagnetic field) are positioned outside the "atomic" centers. This displacement creates a polarization mismatch at the interface, which gives rise to the topological modes.

These edge modes still exhibit bulk–edge correspondence since they originate from the Berry (Zak) phase. The Berry phase is related to the charge polarization $\sigma_{x,y} = P_{x,y}/2\pi$ [34, 44]. When the structure has inversion symmetry, the Zak phase can take only two values (0 or π) [45]. Consequently, the charge polarization is quantized to 0 or $\frac{1}{2}$, which is well-defined up to 1. This is because the Wilson loop is defined on $(-\pi, \pi]$, as it corresponds to the phase of the eigenvalues of the Wilson operator.

This approach is the one ultimately adopted in this thesis.

1.3 Current state of the art

Topological photonics is a broad and rapidly developing field, and a comprehensive overview is beyond the scope of this thesis. We therefore refer the reader to several recent reviews that provide a general introduction to the subject [46, 47, 48, 49]. In this section, we focus on developments that are directly relevant to this work, namely $\mathbb{Z}_2$ and OAL topologies, inverted eigenmode order edge states, lattice symmetry considerations, and design strategies compatible with integrated photonics.

Early efforts in topological photonics were largely inspired by Chern topology, which enables unidirectional and nonreciprocal edge transport [43]. However, Chern topological phases require time-reversal symmetry breaking, typically achieved using external magnetic fields, which strongly limits scalability and compatibility with nanophotonic platforms. This motivated a shift toward $\mathbb{Z}_2$ topologies, which preserve time-reversal symmetry and are analogous to quantum

spin Hall phases in condensed matter systems. In electronic systems, such phases arise naturally due to fermionic spin degrees of freedom. In photonics, however, the bosonic nature of light makes the realization of $\mathbb{Z}_2$ topology nontrivial.

A major breakthrough occurred in 2015, when Wu Et al. proposed a scheme to emulate pseudospin degrees of freedom in a purely dielectric photonic crystal with C_6 symmetry [50]. This work demonstrated that degenerate modes protected by lattice symmetry could mimic spin-like behavior, enabling $\mathbb{Z}_2$-type topological edge states without magnetic fields. This proposal triggered extensive research on hexagonal (C_6) lattices, where symmetry-protected Dirac points and band inversions can be engineered in a relatively straightforward manner.

Subsequent studies explored different realizations of inverted eigenmode order and $\mathbb{Z}_2$ topology in C_6-symmetric systems. Xu et al. demonstrated multiple band symmetry inversions using a simple ring-shaped unit cell and highlighted the role of accidental degeneracies in achieving topological modes [51]. Palmer later provided a deeper theoretical analysis of pseudospin-based $\mathbb{Z}_2$ topology by studying Berry curvature and the Wilson spectrum [52]. Huang introduced a rotatable six-triangle unit cell that enables a topological phase transition using a single dielectric material, achieving nearly perfect transmission and strong robustness against defects [53]. Jin showed that inverted eigenmode states remain robust against cavity defects and interface disorder in waveguide–resonator systems operating at visible wavelengths [54]. More recently, Du employed neural network-based optimization to reduce the accidental nature of band inversions in C_6 lattices [55], and He proposed helical edge states based on a ring unit cell for wavelength-division multiplexing and Y-splitting applications [56].

These works clearly demonstrate that inverted eigenmode order topological states in C_6-symmetric lattices are well understood and can exhibit excellent robustness and transmission properties. However, most photonic integrated circuits, including logic gates and routing architectures, are fabricated on orthogonal grids. As a result, square (C_4) symmetry is often more compatible with existing technologies, particularly for scalable and compact implementations of logical operations [57]. This motivates growing interest in extending $\mathbb{Z}_2$ and OAL topologies to C_4-symmetric lattices.

In this work, we focus on OAL topology in a C_4 lattice by inverting the natural order of the eigenmode symmetry. While the same conceptual approach has been extensively explored in C_6 lattices, its implementation in C_4-symmetric structures remains relatively underexplored and significantly more challenging due to stricter symmetry constraints and the reduced flexibility in engineering mode degeneracies.

Several attempts have been made to realize topological protection in C_4-symmetric photonic crystals. He reported a square-lattice design compatible with integrated photonic platforms [58]. Although topological edge states were demonstrated, the reported transmission was insufficient for practical use, with a 5% drop over a propagation distance of 20 unit cells (10 μm). Xiong designed a square-lattice photonic crystal supporting both edge and corner states [59], but the structure relies on two different materials and lacks explicit C_4 or mirror ($M_{x(y)}$) symmetry. Moreover, transmission properties were not characterized, as the work focused primarily on slow-light effects. More recently, Zhang proposed a Penrose-type lattice with effective eight-fold symmetry [60]. While conceptually interesting, the complexity of the unit cell raises fabrication challenges, and transmission

characteristics of the topological interface were not reported.

As a result, a single-material, easily fabricable, C_4-symmetric photonic crystal supporting robust and low-loss $\mathbb{Z}_2$ topological modes in the visible or near-infrared spectral region remains an open problem.

In parallel with structural design efforts, several methodological frameworks for identifying and characterizing topological phases in photonic crystals have been developed. Blanco provided a detailed tutorial on calculating Chern numbers, Berry curvature, and Wilson loops in two-dimensional photonic crystals [20], which forms the basis of the approach adopted in this thesis and described in Sections 1.1 and 1.2.1. This framework was later extended to three-dimensional systems [61]. Wang emphasized Wilson-loop-based methods and fragile topology [62], while Christiansen introduced topological optimization techniques that enable the simultaneous refinement of band gaps and transmission properties during the design process [63, 64].

Supportive techniques and applications have also progressed significantly. Kagami developed mode converters and vertical coupling schemes to interface conventional silicon waveguides with topological waveguides, improving integration with existing photonic platforms [65, 66]. Zhang experimentally demonstrated a complete set of topological photonic logic gates and characterized their extinction ratios, providing strong evidence for practical usability [67]. Topological photonic crystals have further been explored for slow-light applications, starting from robust optical delay lines [14] to topological cavities with broadband Purcell enhancement [68], and most recently to actively controlled slow-light devices on integrated chips [69].

In summary, while $\mathbb{Z}_2$ and inverted eigenmode order topologies in C_6-symmetric photonic crystals are well established, their extension to C_4-symmetric lattices remains limited by low transmission, material complexity, or fabrication challenges. The objective of this thesis is to address these bottlenecks by proposing and analyzing a C_4-symmetric photonic crystal design based on OAL topology that is compatible with integrated photonic technology and supports robust, low-loss topological edge states.

2 Simulation techniques

In this work, we primarily use two numerical methods. First, we employ MPB to obtain the eigenfunctions from equation 1.12 of an individual PC unit cell and to calculate the topological modes at the interface. Second, we use FDTD to compute the transmission properties of the interface. Both methods support Python integration, enabling an automated workflow. MPB is accessed through the Python-based MEEP library [27, 70], while for FDTD, we use Ansys/Lumerical, which provides Python integration via the Interconnect module.

In this chapter, we provide a brief introduction to both numerical methods and examine how they can be used to extract topological characteristics. To do this, we follow the work of Huang [53] and replicate his findings, originally obtained using COMSOL, using MPB and FDTD. This approach allows us to demonstrate the application and workflow of these methods. We selected this study because it contains band structure analysis, eigenmode analysis, and transmission analysis. Moreover, it employs a moderately complex geometry, making it well-suited for demonstration purposes. By using MPB and FDTD instead of COMSOL Multiphysics, we also illustrate the consistency between our tools and those used in the published literature. To prove this point, we consider in this section a photonic crystal which consists of a hexagonal arrangement of dielectric isosceles triangles in a triangular lattice. The triangles can rotate around the center of their base. The geometry is shown in Figure 2.1.

2.1 MIT photonic bands

The MIT Photonic Bands (MPB) solver is a free software package designed to compute electromagnetic eigenmodes and eigenfrequencies in periodic, wavelength-independent, anisotropic (ε and μ) media without losses. It is fully vectorial, with the only approximation arising from spatial discretization, which corresponds to the planewave cutoff. MPB also takes advantage of symmetries present in the

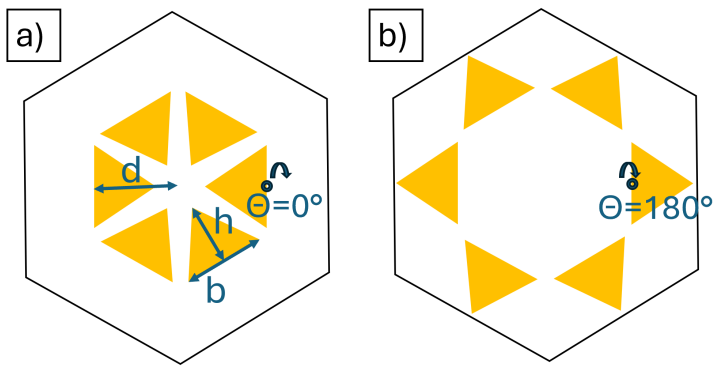


Figure 2.1 Geometry of the unit cell of the PC defined in [53]. Free parameters are displacement d, triangular base b, triangular height h and the rotation of triangles Θ. **a)** $\Theta = 0°$ **b)** $\Theta = 180°$

dielectric medium. It employs an iterative eigensolver based on a preconditioned conjugate-gradient method [71] to efficiently find eigenvalues [72].

To set up the MPB calculation, we must specify the lattice of the photonic crystal by defining the lattice basis vectors. All geometry is then constructed within this coordinate system. The photonic crystal we aim to describe has a triangular lattice, as shown in Figure 2.2. We have marked two red dots to illustrate the use of the new coordinate system. Placing objects at these marker points corresponds to coordinates $\boldsymbol{p}_1 = (1, -1)$ and $\boldsymbol{p}_2 = \left(0, -\frac{1}{2}\right)$.

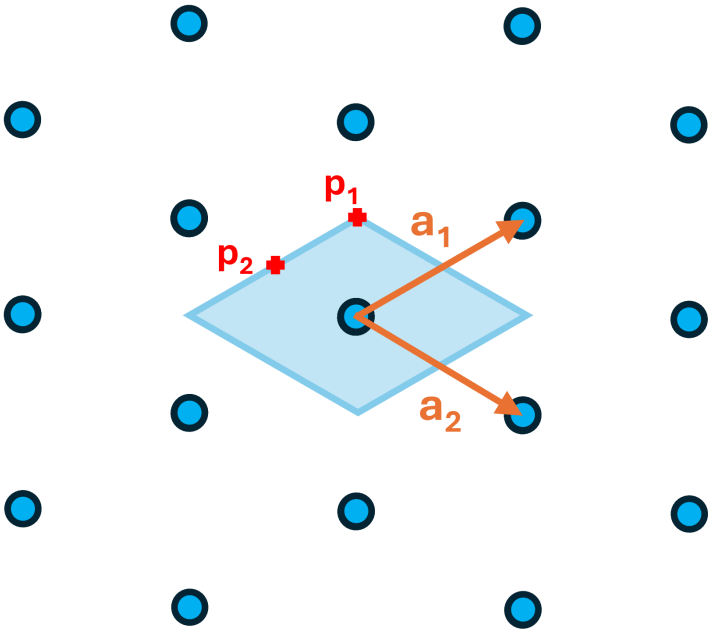


Figure 2.2 The depiction illustrates the MPB base vectors in real space. The vectors $\boldsymbol{a}_1 = a\left(\frac{\sqrt{3}}{2}, \frac{1}{2}\right)$ and $\boldsymbol{a}_2 = a\left(\frac{\sqrt{3}}{2}, -\frac{1}{2}\right)$ define a triangular lattice. Red markers indicate positions in the new basis with coordinates $\boldsymbol{p}_1 = (1, -1)$ and $\boldsymbol{p}_2 = \left(0, -\frac{1}{2}\right)$. The blue parallelogram represents the unit cell of the photonic crystal.

The basis vectors are then normalized to have a length of 1. MPB operates in scale-less units, returning frequency values in the form $\frac{\omega a}{2\pi c} = \frac{a}{\lambda}$, where a is the lattice constant.

MPB also requires the specification of $\boldsymbol{k}$-points. These must be provided in the reciprocal basis. For base vectors $\boldsymbol{a}1 = (a1x, a_{1y})$ and $\boldsymbol{a}2 = (a2x, a_{2y})$, the reciprocal lattice vectors can be written as [73]:

$$\mathbf{b}_1 = \frac{2\pi}{A}\begin{bmatrix} a_{2y} \\ -a_{2x} \end{bmatrix} \tag{2.1}$$

$$\mathbf{b}_2 = \frac{2\pi}{A}\begin{bmatrix} -a_{1y} \\ a_{1x} \end{bmatrix} \tag{2.2}$$

$$A = a_{1x}a_{2y} - a_{1y}a_{2x} \tag{2.3}$$

This yields the high-symmetry points $\boldsymbol{\Gamma} = (0, 0)$, $\boldsymbol{M} = \left(0, \frac{1}{2}\right)$, and $\boldsymbol{K} = \left(-\frac{1}{3}, \frac{1}{3}\right)$, as shown in Figure 2.3.

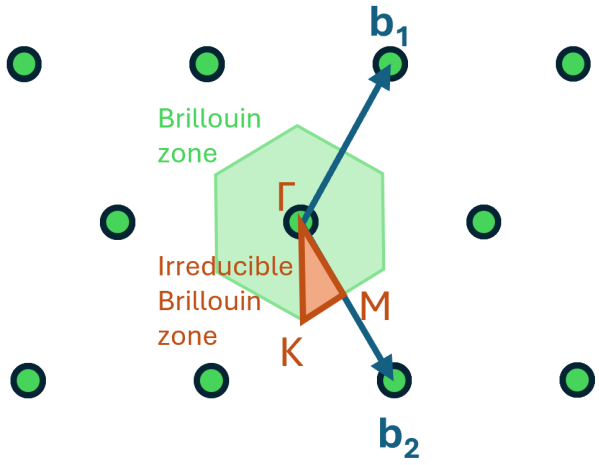


Figure 2.3 The formation of the Brillouin zone and the irreducible Brillouin zone based on the basis vectors defined in Figure 2.2. The reciprocal lattice vectors are $\boldsymbol{b}_1 = \frac{2\pi}{a}\left(\frac{1}{\sqrt{3}}, 1\right)$ and $\boldsymbol{b}_2 = \frac{2\pi}{a}\left(\frac{1}{\sqrt{3}}, -1\right)$. The high-symmetry points in this reciprocal space basis are $\boldsymbol{\Gamma} = (0, 0)$, $\boldsymbol{M} = \left(0, \frac{1}{2}\right)$, and $\boldsymbol{K} = \left(-\frac{1}{3}, \frac{1}{3}\right)$.

Now we can specify the lattice and the geometry to be calculated. First, we investigate an individual unit cell of the photonic crystal. The code is as follows:

```
# Library import (1)
import numpy as np
import meep as mp
from meep import mpb

# Extract variables (2)
H = params[0]    # height
D = params[1]    # displacement
B = params[2]    # base
theta = params[3]
mat1 = mp.Medium(epsilon=eps[0])

# Define the geometry lattice (3)
geometry_lattice = mp.Lattice(size=mp.Vector3(1, 1),
    basis1=mp.Vector3(math.sqrt(3)/2, 0.5),
    basis2=mp.Vector3(math.sqrt(3)/2, -0.5)
    )

# Create a function to add triangles to unit cell (4)
def add_triangle_2(H, L, B, theta, alpha, Cx, Cy):
    theta = 180-theta
    theta = theta/180*np.pi
    # Base vertex of the triangle in Cartesian:
    Dx = Cx + L*math.cos(alpha)
    Dy = Cy + L*math.sin(alpha)

    # Two base corners in Cartesian:
    Nx = Dx - (B/2.0)*math.sin(alpha + theta)
    Ny = Dy + (B/2.0)*math.cos(alpha + theta)

    Mx = Dx + (B/2.0)*math.sin(alpha + theta)
```

```
    My = Dy - (B/2.0)*math.cos(alpha + theta)

    # Apex in Cartesian:
    Ox = Dx + H*math.cos(alpha + theta)
    Oy = Dy + H*math.sin(alpha + theta)


    #  Transform each corner to the (u,v) basis.
    def to_lattice_coords(x, y):
        v = (2.0 / math.sqrt(3.0)) * y
        u = x - 0.5*v
        return (u, v)

    Nu, Nv = to_lattice_coords(Nx, Ny)
    Mu, Mv = to_lattice_coords(Mx, My)
    Ou, Ov = to_lattice_coords(Ox, Oy)

    geometry.append(
        mp.Prism(
            # Lattice coords => mp.Vector3(u, v, 0)
            vertices = [
                mp.Vector3(Nu, Nv),
                mp.Vector3(Mu, Mv),
                mp.Vector3(Ou, Ov)
            ],
            height=1,
            material=mat1
        )
    )

# Create and populate the geometry list (5)
geometry = []
for i in range(6):
    alpha=2*np.pi/6.*i
    add_triangle(H,L,B,theta,alpha,0,0)
```

The code can be understood as follows: **(1)** Import the `meep` library, which gives access to MEEP vectors used to define lattice and geometry objects, as well as the `mpb` module required for the solver in later code snippets. `NumPy` is used to handle trigonometric operations. **(2)** Since the geometry will be tuned, the parameters are passed as a list and then extracted for clarity. **(3)** Create the geometrical lattice by setting the lengths of the basis vectors to 1 and defining their directions according to Figure 2.2. **(4)** Define a function to create a single triangle based on height H, displacement D, base length B, angle θ, which marks the rotation of the triangle around the center of its base, and angle α, which marks the direction of the triangle around the center of the cell. The triangle group is centered at coordinates C_x and C_y. The function first constructs the triangle's vertices in Cartesian coordinates N, M, and O, and then transforms them using the defined transformation function. Finally, the triangle is added to a geometry list using the `mp.Prism` method, where we specify the material and set the height to 1, as we are operating in two dimensions. **(5)** Create a geometry list to be passed to the solver and populate it using the `add_triangle` method with six triangles, defined by different values of the angle α.

Now that we have specified the lattice and the geometrical objects of the photonic

crystal that we use as an example, we can proceed to construct the MPB solver. To do this, we need to define the number of solutions (bands), the $\boldsymbol{k}$-points to be solved, the resolution of the unit cell, and the background material.

Taking into account the first point, we stress that, when considering the N bands in a given system, it is advisable to calculate the $N + 2$ bands instead of just N. The reason is that this ensures that the solution is not a mix of two different band types when there is a band crossing at the top of the spectrum. ugh rare, some systems exhibit one band crossing multiple bands, which is why we recommend calculating two extra bands [45]. Regarding the $\boldsymbol{k}$-points, which should be solved, we usually represent them by constructing a path starting at Γ, and specifying the corner points. MPB then allows to fill in additional $\boldsymbol{k}$ to achieve a desired resolution, so we do not need to specify it separately. Another relevant aspect is the number of spatial steps that discretize the photonic crystal unit cell. According to MPB gidelines [74], it is recommended to use a power of 2. In our calculations, we use 32 or 64 steps. Finally, to fully define the exemplary crystal, we simply set the relative permittivity of the background material to 0.

A code that realizes the simulation of the proposed example of photonic crystal is the following:

```
# Define vertices of the path in reciprocal space (1)
k_points = [
    mp.Vector3(0,0),          # Γ
    mp.Vector3(-1/3,1/3),     # K
    mp.Vector3(0,0.5),        # M
    mp.Vector3(0,0),          # Γ
    ]

# Insert additional points between the vertices (2)
points_to_insert = 8
k_points = mp.interpolate(points_to_insert, k_points)

# Initiate the MPB solver (3)
ms = mpb.ModeSolver(num_bands=7,
    k_points=k_points,
    geometry=geometry,
    geometry_lattice=geometry_lattice,
    resolution=32,
    default_material=mp.Medium(epsilon=0),
    force_mu=False
    )
```

The code contains the following instructions: **(1)** Definition of the path in reciprocal space using the reciprocal basis vectors (see Figure 2.3). **(2)** Increase the path resolution by adding eight additional points between each pair of high-symmetry points. **(3)** Initialization of the mode solver object. The `force_mu` flag is set to `False` for an anisotropic medium.

Before proceeding with the calculation and presenting the results, it is good practice to check whether the geometry has been defined correctly. To do this, we can plot the permittivity:

```
# Initiate modesolver parameters and obtain epsilon (1)
ms.init_params(True, True)
eps = ms.get_epsilon()
```

```
# Edit visualization (2)
md = mpb.MPBData(rectify=rectify,
    periods=2,
    resolution=32)
converted_eps = md.convert(eps)

# Yor favorite way of ploting bittmap (3)
...
```

We discuss the following points of this code: **(1)** Since we are not using a run command, we need to initialize the mode solver parameters manually. These flags represent parity and reset fields options, which are irrelevant for the `get_epsilon` function call. The permittivity comes out angled as we are dealing with a hexagonal lattice. We rectify it for plotting purposes in **(2)**, where we also increase the number of periods to be plotted to 2 to show the lattice. Finally, in **(3)** we can plot the `converted_eps` any way we like. In this case, we increased the resolution to 128 to get nicer images, as shown in Figure 2.4.

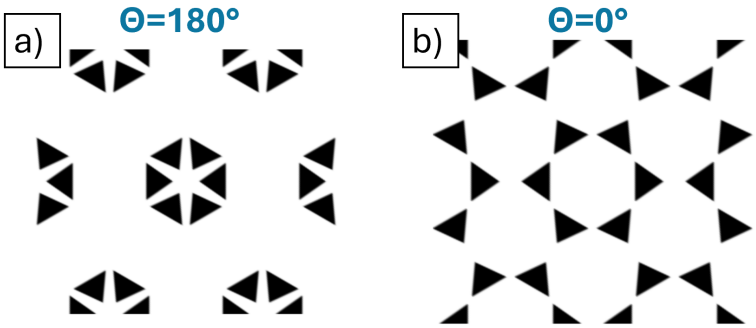


Figure 2.4 Plot of permittivity of the geometry defined in the code above. Black color represents material. Parameters used were same as in [53]. ($H = 0.2a; D = 0.3a; B = 0.28a; \varepsilon_r = 12$). Resolution of the solver was increased to 128 for better plot quality.

With the correct geometry, we can proceed to run the calculation and extract the results.

2.1.1 MPB bandstructure

In this section, we demonstrate how to run the simulation to obtain the eigenfrequencies, extract information about the gap, and use these objects for visualization using the Python matplotlib library.

```
# Run the calculation for TM modes and get eigenfrequencies (1)
ms.run_tm(mpb.fix_hfield_phase)
tm_modes = ms.all_freqs

# Get a list of gaps (2)
tm_gaps = ms.gap_list

# Produce plots (3)
resol = points_to_insert+1
y_max = max(tm_modes[:,num_bands-1])+0.1
k_float_label = 3*points_to_insert*np.linspace(0,1,resol*3+1)
```

```
fig, ax = plt.subplots()
ax.plot(k_float_label, tm_modes, color='blue', lw=2)

for gap in tm_gaps:
    if gap[0] > 1:
        ax.fill_between(x, gap[1], gap[2],
                        color='blue', alpha=0.2)

ax.set_xticks(k_float_label[[0,resol,2*resol,3*resol]])
ax.set_xticklabels(["Γ","K(K')","M","Γ"])
plt.ylabel('ωa/(2πc)', fontsize=16)
ax.set_xlim(k_float_label[0],k_float_label[3*resol])
ax.set_ylim([0, y_max])

ax.vlines(k_float_label[resol],
    ymin=0,
    ymax=2*y_max,
    colors='k',
    linestyles="solid",
    lw=1)
ax.vlines(k_float_label[2*resol],
    ymin=0,
    ymax=2*y_max,
    colors='k',
    linestyles="solid",
    lw=1)

plt.show()
```

(1) The simulation is run with the `fix_efield_phase` option to ensure that the phase is not random, but instead maximizes the energy in the real part of the field. This does not affect the band structure calculations, but it is essential when dealing with eigenfunctions. **(2)** MPB offers a convenient method to extract information about band gaps, which we can use to look for band gap overlaps. **(3)** The code produces a plot of the band structure, including highlighted band gaps, marked high-symmetry points, and a scale-less y-axis.

Using the code above with fixed values of $H, D, B = [0.2a, 0.3a, 0.28a]$ and for three different values of $\Theta = [0°, 122°, 180°]$ produces the band structures shown in Figure 2.5, demonstrating agreement with the results shown in [53] calculated using COMSOL. Therefore, these results validate the approach taken in this Thesis, which relies on the use of MPB and FDTD to compute the photonic band structures and their properties.

On the other hand, the band structures displayed in Figure 2.5 reveal another aspect that is central in this Thesis. More specifically, the computed structures show that the change from $\Theta = 0°$ to $\Theta = 180°$ is not an adiabatic transformation, since along the way, at $\Theta = 122°$, the band gap closes, forming a double Dirac cone. This indicates the possibility of a symmetry band inversion. To determine whether an inversion occurred and the system became topological, we need to investigate the eigenmodes in those bands, which is discused in the following section.

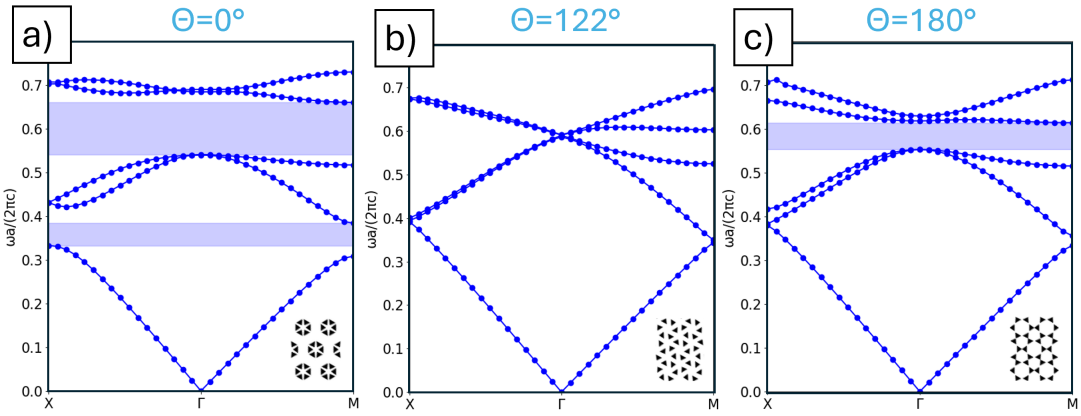


Figure 2.5 Bandstructures of PC unit cells designed by Huang in [53]. Fixed parameters are: $H = 0.2a; D = 0.3a; B = 0.28a; \varepsilon_r = 12$, the PC geometry is depicted in the bottom right corner. (a) $\Theta = 0°$, the PC is in topologically trivial state (b) $\Theta = 122°$, the band-gap closes, the PC is in a process of topological tzransition (c) $\Theta = 180°$, the PC is in topologicaly non-trivial state

2.1.2 MPB eigenmodes

Using the mode solver object defined in Section 2.1, the eigenmodes at Γ can be obtained as follows:

```
# Function to extract fields (1)
def get_fields(ms, band):
    fields.append(ms.get_efield(band, bloch_phase=False))

# Run the calculation (2)
fields=[]
ms.run_tm(mpb.output_at_kpoint(mp.Vector3(0,0),
    mpb.fix_efield_phase,
    get_fields))

# Prepere fields for plot (3)
rectified_fields=[]
for f in fields:
    f=f[...,0,2]
    rectified_fields.append(md.convert(f))
eigvec = np.array(converted).real

# Produce the plot (4)
for i, field in enumerate(eigvec):
    plt.subplot(331 + i)
    plt.contour(converted_eps.T, cmap='binary')
    plt.imshow(field.T,
        interpolation='spline36',
        cmap='RdBu',
        alpha=0.9)
    plt.axis('off')

plt.show()
```

(1) Definition of a function for extracting the eigenmodes from the solver. **(2)** Running the simulation with the extraction function as a solver parameter. We

run only the TM modes, as these are the modes that produce the photonic band gap. The field we are extracting is the z-component of the electric field. **(3)** As in the permittivity plot, the fields are angled due to the triangular lattice calculations and need to be rectified. We also separate the real part for plotting purposes. The field generally has a random phase, which is fixed by the `fix_efield_phase` option in (2), maximizing the energy in the real part. To recognize the symmetry of the eigenmode, it is sufficient to use only the real part. **(4)** Plotting procedure of the eigenfunctions. Using the contour method provided by the matplotlib library, we can visualize the edges of the material to gain a better understanding of the modes.

The eigenmodes are shown in Figure 2.6. Mode 1 is trivial for both configurations. For $\Theta = 0°$, modes 2 and 3 have p symmetry and modes 4 and 5 have d symmetry. For $\Theta = 180°$, the order is reversed: modes 2 and 3 have d symmetry and modes 4 and 5 have p symmetry. This creates a clear band-symmetry inversion between the two geometries.

From Figure 2.5, we see that in both configurations modes 1, 2, and 3 lie at lower frequency (below the band gap near $a/\lambda = 0.6$), while modes 4 and 5 lie at higher frequency (above this gap). In other words, both geometries share the same band gap, but the symmetries of the bands directly below (modes 2 and 3) and directly above (modes 4 and 5) this gap are exchanged when Θ changes from 0° to 180°. This inversion of the band symmetries across the common gap indicates that interface modes can appear inside this gap.

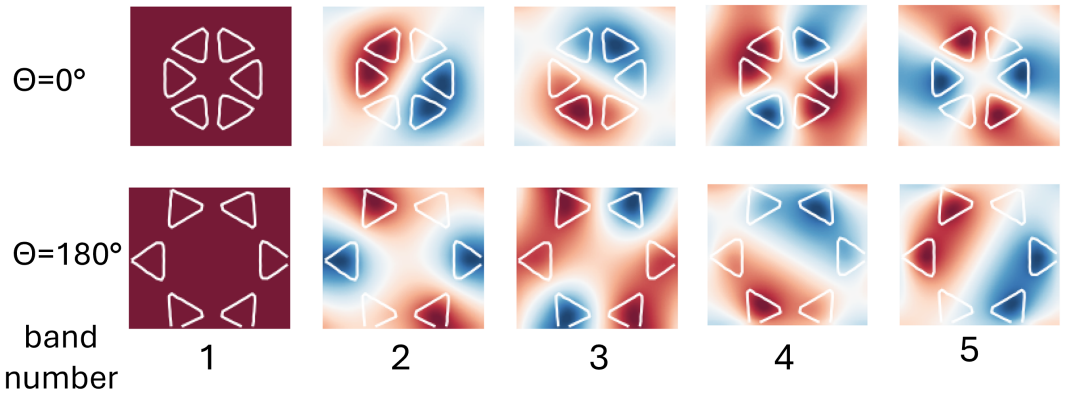


Figure 2.6 Eigenmodes of the PC designed by Huang [53] at Γ. Countours of the underlying structure are shown. The images depicts the real part of E_z field with a fixed phase.

Since the topological modes are a property of the bulk and appear at the interface, in the next section we show how to combine individual unit cells to form a topological interface using MPB.

2.1.3 MPB interface

In the previous section, we showed how to calculate a band structure of an individual PC unit cell. To observe the topological modes, we need two semi-infinite planes of topologically trivial and topologically non-trivial PCs. Neither MPB nor FDTD supports these types of simulations. To deal with this problem,

we use a supercell containing several periods of PC_1 unit cells and several periods of PC_2 unit cells. Such a supercell is depicted in Figure 2.7a. This pattern is then periodically repeated by MPB, forming the structure shown in Figure 2.7b.

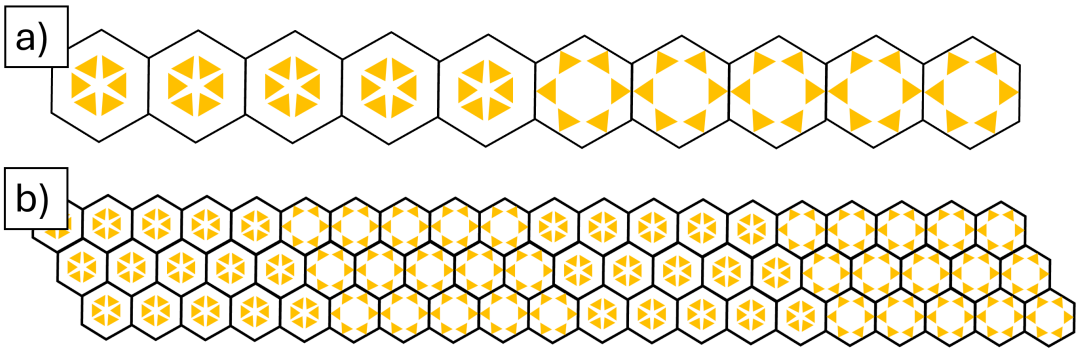


Figure 2.7 Example of a unit-cell for interface MPB calculations. **a)** single unit-cell defined in MPB geometry list. **b)** Pattern prodiced by periodical repetition of the Unit-cell, mimicing the topological interface.

The interface calculations are similar to those of a single unit cell, with just a few differences:

```
...
# Increase the size of lattice (1)
geometry_lattice = mp.Lattice(size=mp.Vector3(2*Npers,1),
    basis1=mp.Vector3(math.sqrt(3)/2, 0.5),
    basis2=mp.Vector3(math.sqrt(3)/2, -0.5)
    )
...

# Add the number of periods to the unit cell (2)
def add_structure(cx,cy,theta):
    for i in range(6):
        alpha=2*np.pi/6.*i
        add_triangle(H,L,B,theta,alpha,cx,cy)

for i in range(Npers):
    cy = 0
    cx = i+0.5
    theta=0
    add_structure(cx,cy,theta)
    cx=i+0.5-Npers
    theta=np.pi
    add_structure(cx,cy,theta)
...
```

(1) The size of the unit cell has to be adjusted to accommodate $2N$ elementary unit cells (N for each type of PC). **(2)** The building blocks of the unit cell have to be replicated with different `x_offset` values.

A band structure with eight periods of each PC type is shown in Figure 2.8. Since we now have sixteen PC unit cells in the supercell, the number of calculated bands has to be increased. For single-cell calculations, we needed to calculate 5 bands, but here we need eighty. In this case, the topological modes partially breach the band gap, one from below and one from above.

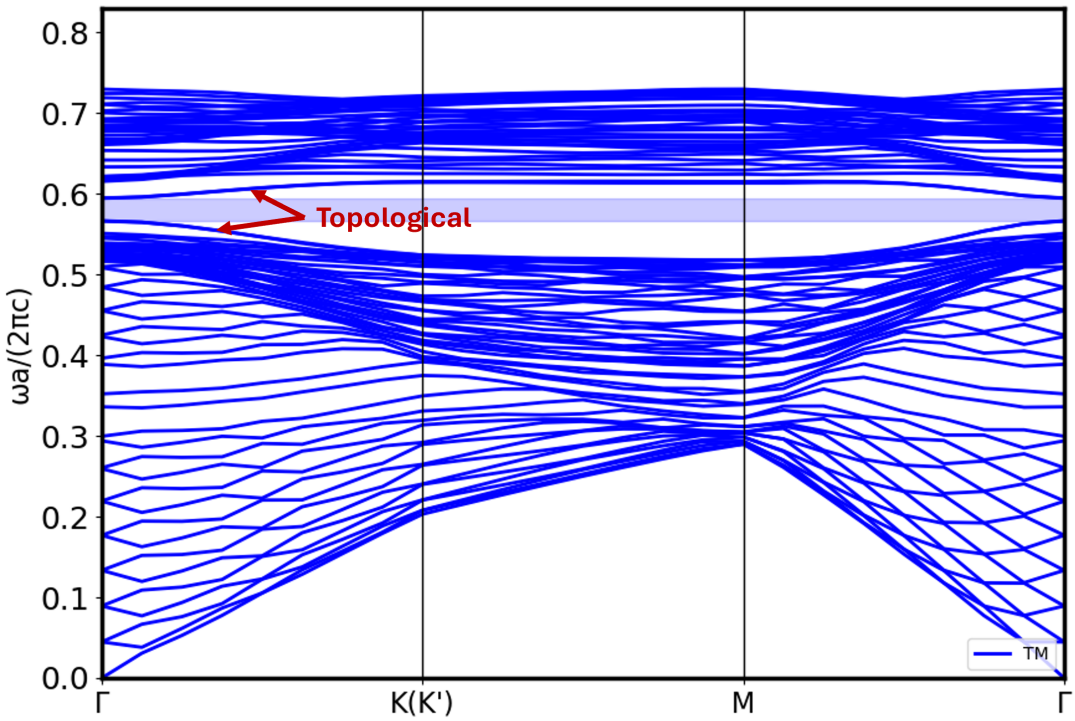


Figure 2.8 Reproduction of the topological interface band structure calculation done by Huang [53]. 8 topologically trivial PC unit cells and 8 topologically non-trivial PC unit cells was used in a supercell.

This concludes the introduction to MPB and its use in topological calculations throughout this thesis. We have demonstrated that it can replicate results obtained by COMSOL by reproducing the calculations done by Huang [53]. The next step, aimed at the analysis of the transmission characteristics of the crystals and the impact of defects, requires the use of a different tool, which in our case is the FDTD algorithm. We discuss this aspect in the following.

2.2 FDTD method

The Finite-Difference Time-Domain method is a technique for directly solving Maxwell's equations. It discretizes the spatial coordinates into a Yee grid [75] and introduces a finite time step. The numerical stability of the method is controlled by the relation between the time step and the spatial step. Typically, the time step is chosen so that it takes the electromagnetic wave ten to twenty time steps to propagate through the unit cell with the highest refractive index in the simulation region to ensure the simulation stability.

Discretizing the spatial and time steps allows reformulating Maxwell's equations into evolution equations, where the field variables are calculated based on previous time steps. The evolution equation for TM modes in two dimensions can look as follows:

$$
\begin{aligned}
\tilde{E}_z^{n+1}(i,\,j) &= C_{ezez}(i,\,j)\tilde{E}_z^{n}(i,\,j) \\
&\quad + C_{ezhy}(i,\,j)\Big[H_y^{n+\frac{1}{2}}(i,\,j) - H_y^{n+\frac{1}{2}}(i-1,\,j)\Big] \\
&\quad - C_{ezhx}(i,\,j)\Big[H_x^{n+\frac{1}{2}}(i,\,j) - H_x^{n+\frac{1}{2}}(i,\,j-1)\Big] \\
&\quad - C_{ezjiz}(i,\,j)j_{iz}^{n+\frac{1}{2}}(i,\,j) \\
H_x^{n+\frac{1}{2}}(i,\,j) &= C_{hxhx}(i,\,j)H_x^{n-\frac{1}{2}}(i,\,j) \\
&\quad - C_{hxez}(i,\,j)\Big[\tilde{E}_z^{n}(i,\,j+1) - \tilde{E}_z^{n}(i,\,j)\Big] \\
&\quad - C_{hxmix}(i,\,j)M_{ix}^{n}(i,\,j) \\
H_y^{n+\frac{1}{2}}(i,\,j) &= C_{hyhy}(i,\,j)H_y^{n-\frac{1}{2}}(i,\,j) \\
&\quad + C_{hyez}(i,\,j)\Big[\tilde{E}_z^{n}(i+1,\,j) - \tilde{E}_z^{n}(i,\,j)\Big] \\
&\quad - C_{hymiy}(i,\,j)M_{iy}^{n}(i,\,j)
\end{aligned}
\tag{2.4}
$$

Here, the upper index of the field variables n indicates the time step, while i, j mark the position on the grid, and the C_{****} terms include permittivity, permeability, conductivity, and stability factors. The half step at the n variable is a feature of the Yee grid (see Figure 2.9), which separates the electric and magnetic fields into two distinct subgrids with a half-step offset. This enables a central difference approximation of the derivatives without increasing the grid resolution.

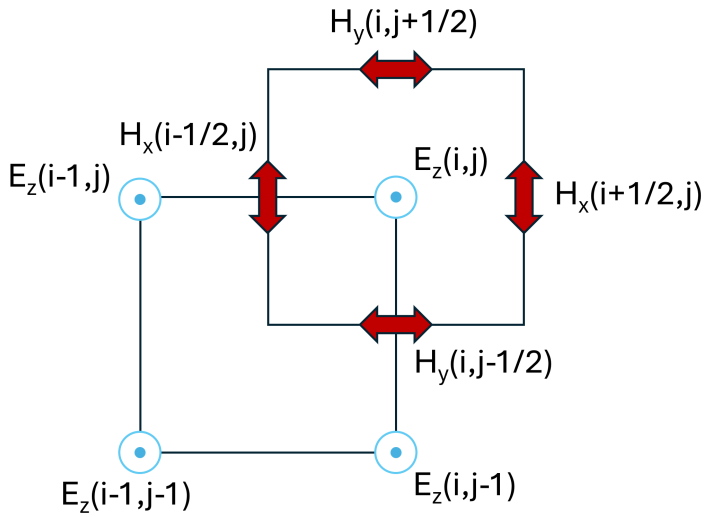


Figure 2.9 Schematic representation of a single grid cell in the 2D Yee grid before reindexing the sub-grids. The diagram illustrates the field components of the transverse magnetic (TM) mode, including the electric field E_z at the grid points and the magnetic field components H_x and H_y at staggered half-grid positions.

Notice that to calculate a field component at (i, j), it is necessary to know the field at $(i+s, j+s)$, where $s \in \{-1, 0, 1\}$. This becomes an issue at the boundary of the simulation region, where some components are missing. Supplementing the missing values with zeros would lead to artificial reflections at the boundary.

The solution to this problem is to introduce artificial layers called PML (perfectly matched layers), with gradually increasing material loss, which are perfectly matched in conductivity with the simulation objects. As the field propagates through these layers, it is gradually absorbed, and in the new simulation region, the reflections caused by missing simulation cells are suppressed. Simulating the photonic crystal unit cells avoids this issue, since periodic boundary conditions (or Bloch boundary conditions for specific $\boldsymbol{k}$-vector simulations) can be used instead. However, for topological interface transmission simulations, PML must be used.

FDTD operates in the time domain, which allows recording raw field data in a specific simulation region. This data can later be processed to obtain the spectral behavior or other properties, meaning that all specified frequencies are obtained from a single simulation. This places a small constraint on the material data, as we need an analytical description of the material properties in the selected frequency range to model dispersive behavior. This constraint is not an issue in this work, as we focus on dielectric materials, namely Indium Phosphide (InP), available in the Lumerical material database [76, 77], in a spectral region with little to no dispersion. The targeted wavelength for the potential application is 1550 nm. The InP model for FDTD is shown in Figure 2.10. The imaginary part of the relative permittivity is on the order of 10^{-9} in this region.

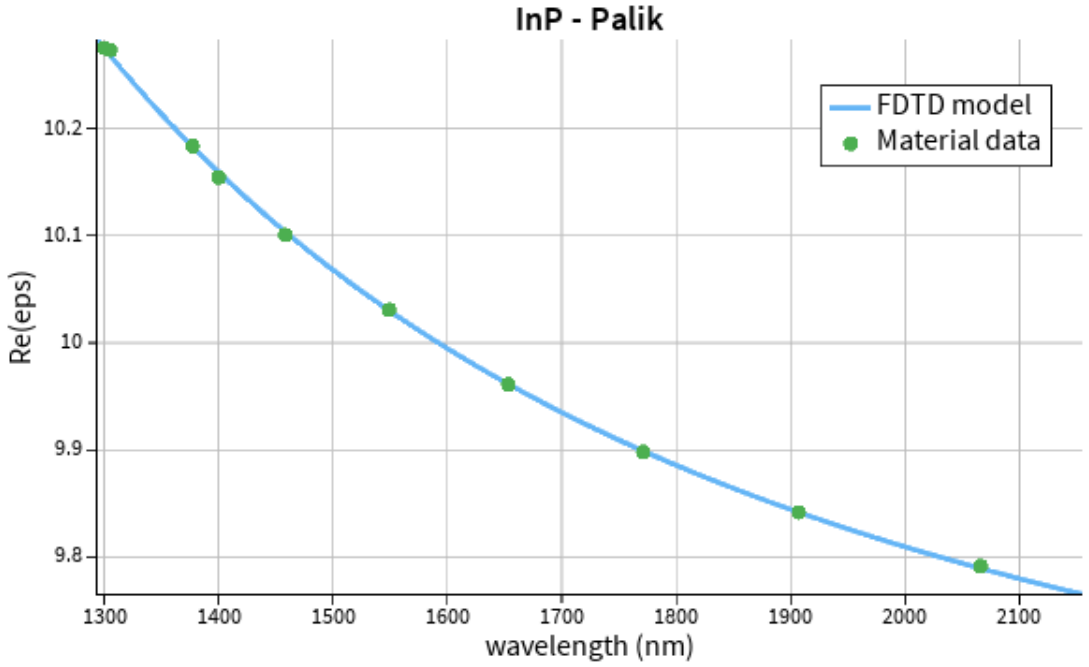


Figure 2.10 Relative permittivity of InP used in the FDTD simulation. The figure demonstrates a strong agreement between the data published by Pelik and the model implemented in the FDTD simulation.

2.2.1 FDTD in topological simulations

We use FDTD in two situations: **a)** To characterize the transmission of the topological interface **b)** To demonstrate the presence of topological bands in the photonic band gap by a method other than MPB

The FDTD method is a universal solver that could be used for all the calculations in this work. However, for solving eigenproblems, the frequencies are captured via Fourier transform, which does not guarantee capturing all eigenfrequencies, especially in the case of degeneracies. Furthermore, if we wanted to obtain the eigenfunctions, we would need to run the simulation for each eigenfunction individually. This why in this Thesis we rely on MPB to solve the eigenproblems, where we rely on FDTD to carry out the transmission calculations and to validate the existence of topological modes through a method other than MPB.

The FDTD simulation in Ansys / Lumerical consists of the following objects: **a)** The geometrical objects we want to simulate **b)** The FDTD simulation region, which sets up the mesh and boundary conditions **c)** The electromagnetic field source **d)** The monitors that record the fields, which might be used later in post-processing The specifics of these objects differ based on the type of simulation we are performing.

2.2.2 FDTD transmission simulation

The schema of the simulation objects for the topological interface simulation is shown in Figure 2.11. The green and orange squares represent different PC unit cells, with each type of PC consisting of $N \times M$ unit cells. These squares should not be confused with the Yee grid—each of them is built on a much more detailed FDTD grid. The simulation region is surrounded by PML layers to suppress reflections. This means we need to use a sufficient number of PC unit cells to invoke periodic behavior. We use $N = 20$, and later we will demonstrate that this number of cells is sufficient.

The source we use is a line source (for 2D simulation) with a custom profile. Since we are interested in the transmission properties of the interface for the topological mode, we do not investigate how the source is created. Other authors, such as Kagami [65], have already designed couplers from regular waveguides to topological waveguides. We obtain the topological source from another simulation that is built similarly to the one described in Figure 2.11, but in this case, the source is a combination of two dipole sources with a 90° phase offset and orientation to invoke all the modes in the desired spectral region. We set the spectral region to the photonic band gap, where only the topological modes exist, and so only the topological modes can couple to the interface and be recorded by the monitor T_2. We then export the recorded field from the monitor T_2 and use it as the input for the source in the transmission simulation. We use a combination of two line frequency-domain profile monitors, T_1 and T_2, separated by K PC unit cells to measure the transmission of the interface, which in this case is defined as the fraction of power propagated from T_1 to T_2.

A technical note on building the simulation geometry: it is recommended to control the simulation objects in Lumerical using the Lumerical scripting language (.lsf file), even though a graphical user interface (GUI) is available. The Lumerical scripting commands are available in Python via the Interconnect Ansys module. Since we are working with geometry optimization, we opted to use Python to handle all simulation settings. However, building simulation objects from Python using Lumerical script commands inflates the setup time, since each

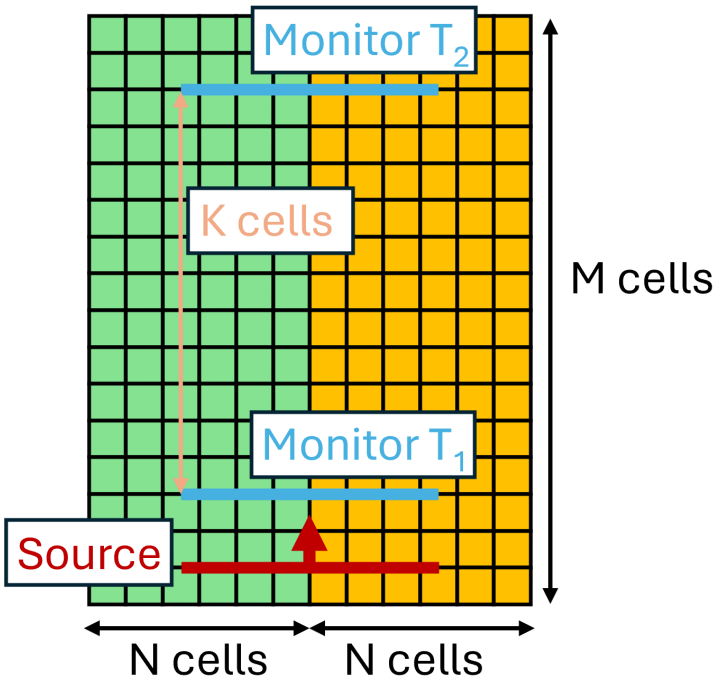


Figure 2.11 Schematic representation of the FDTD interface transmission simulation setup. Green squares indicate trivial photonic crystal unit cells, while orange squares denote topological photonic crystal unit cells. The interface consists of two photonic crystal regions, each containing $N \times M$ unit cells. The red line represents the electromagnetic field source within the simulation domain. Blue lines indicate monitors T_1 and T_2, positioned K unit cells apart, for recording field data.

Python command has to pass through the Interconnect to the Lumerical FDTD solver. Setting up sources, monitors, boundaries, and the mesh is acceptable, as it involves only a few commands, but the geometrical objects, especially in interface simulations, cause problems, as we have to set up thousands of individual objects in the simulation. Each PC unit cell contains several geometrical objects. We solved this problem by creating an .lsf script that accepts a bitmap created by Python, which describes the geometrical objects. This way, the geometrical objects are created from inside the FDTD solver, while still being controlled by Python, which is a much faster option.

Another note for the transmission simulation is that, since the method operates in the time domain, it uses a Fourier transform to obtain spectral data. However, the simulation must run only for a limited time, which effectively truncates the Fourier transform. This creates a problem where the recorded data is polluted by convolution with a sinc function. Suppose we have a source $H(\omega)$ that produces a time-dependent field $h(t)$. The simulation runs only for a certain time, defined by the support function $s(t)$. Then, for the recorded spectrum $R(\omega)$, we can write:

$$R(\omega) = \mathcal{F}\{h(t) \cdot s(t)\} = \mathcal{F}\{h(t)\} * \mathcal{F}\{s(t)\} = H(\omega) * S(\omega) \tag{2.5}$$

Lumerical is efficient with the deconvolution of the results, but in our case, we are dealing with a situation where a topological mode exhibits very high transmission within a photonic band gap that otherwise has zero transmission. This sharp change, effectively a step function, poses a problem for the finite-window

Fourier transform as well as the deconvolution. The recorded spectrum exhibits oscillating behavior. This issue is amplified in the transmission calculation, where we take the ratio of two oscillating functions, especially in regions within the band gap. The small values in the denominator effectively inflate the values in the numerator, which can lead to sharp spikes in the transmission inside the photonic band gap. This is a form of noise amplification and can also result in transmission overshooting 100%, which is non-physical. For this reason, the transmission results should be viewed as qualitative rather than quantitative.

Results of such calculations are shown in Figure 2.12, which presents an FDTD reproduction of the Huang topological interface [53]. Here, we present raw data to demonstrate the oscillation effect in its most severe form. In the scale-less frequency range between 0.51 and 0.52, we can see that the transmission values oscillate around 100%, which corresponds to the topological mode below the photonic band gap. Then, there is a sharp drop in transmission between 0.52 and 0.54, corresponding to the band gap. Afterward, the transmission rises again but with heavy noise, making the second topological mode unrecognizable.

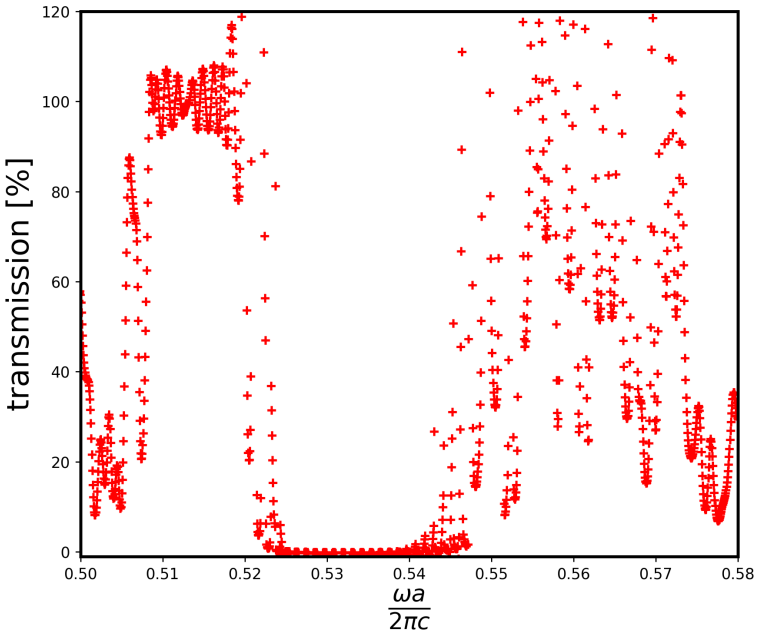


Figure 2.12 Transmission of the topological interface designed by Huag [53] calculated by FDTD method. The oscillations are cause by the finite time windon of the simulation as described in sec. 2.2.2

2.2.3 FDTD bandstructure simulations

There are two types of band structure calculations in this work. The first type involves calculating the band structure of individual photonic crystals to determine the position of the band gap and the ordering of band symmetries to identify band symmetry inversion. The second type involves calculating the band structure of the topological interface, where we are interested in the position, localization, and dispersion of the topological modes. We use FDTD for the latter as a means to cross-verify the results.

Obtaining the band structure through the FDTD method requires running a simulation for each $\boldsymbol{k}$ vector individually. There is also no direct method to obtain the eigenvalues. The simulation process begins by enclosing the PC unit cell in Bloch boundary conditions, which are similar to periodic boundary conditions but support a phase offset. This allows specifying the $\boldsymbol{k}$ point in the reciprocal space that we want to calculate. The source of the field is a swarm of randomly placed broadband dipoles with random polarization, orientation, and phase. The goal is to excite all possible modes in the specified spectral region. A separate swarm of randomly placed time monitors records the field at specific points and observes its decay. The field decays quickly at non-resonant frequencies, while it persists at resonant frequencies (eigenvalues). The eigenfrequencies are then captured from the time monitors by averaging and Fourier transforming. Multiple time monitors are required to avoid cases where the field is recorded at a node of a mode, causing the monitor to miss the resonance. The geometry of the simulation is shown in Figure 2.13.

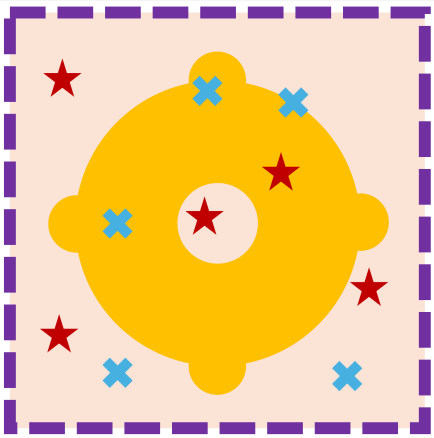


Figure 2.13 Schematic representation of a FDTD band-structure simulation setup. The orange shape represents the photonic crystal unit cell structure, while the pink region denotes the FDTD simulation domain. The purple dashed line indicates the Bloch boundary condition, which determines the position in $\boldsymbol{k}$-space. Red stars mark the randomly selected positions of dipole sources, ensuring excitation of all modes. Blue crosses represent time monitors, which measure the field decay rate to capture the resonant eigenfrequencies.

Furthermore, the unit cell design for the FDTD interface band structure differs from the one used in MPB calculations. Using a single strip of trivial and non-trivial PC cells would result in an unbalanced simulation region, where randomly placed objects (dipole sources and time monitors) would not be able to excite and measure the field. For better convergence, it is beneficial to use a rectified version (see Figure 2.14), even if it requires more unit cells in the simulation. We aim for a side ratio of 4:1. This increase in unit cells within the simulation region would produce significantly more modes folding over each other in MPB. However, since FDTD captures only the Fourier transform of the resonant field, many degenerate resonances are captured as one. This is not an issue here, as we are interested only in the topological modes in the band gap, which appear in pairs and are isolated from the folded bulk modes.

We again demonstrate the use of FDTD in the case of the Huang interface

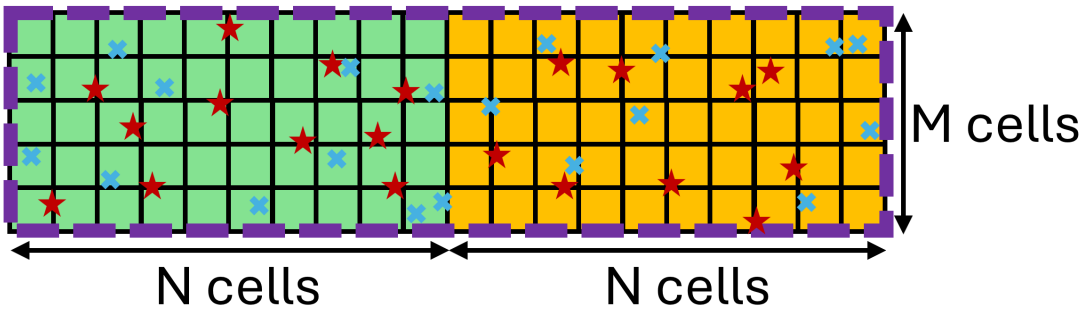


Figure 2.14 Schematic representation of the FDTD interface band-structure simulation setup. Orange squares represent topologically non-trivial photonic crystal unit cells, while green squares denote trivial photonic crystal unit cells. The simulation domain consists of $2N \times M$ such cells. In this study, we set $N = 10$ and $M = 5$ to maintain an aspect ratio of approximately 4:1. Twenty dipole sources (red stars) are randomly positioned to excite all modes, and twenty time monitors (blue crosses) are randomly placed to measure the field decay rate. Bloch boundary conditions (purple dashed lines) are applied.

[53] in Figure 2.15. Here, we can see that some resonances are falsely captured and some are missing.

As opposed to the MPB band structure simulations, the FDTD band structure simulation scheme does not produce eigenmode field distributions. A simulation for each individual eigenmode (not just $\boldsymbol{k}$ vector) would have to be run with spectrally narrow sources and the appropriate Bloch boundary conditions. Although possible, this approach is not recommended, as MPB performs much better in this regard and no new information is gained.

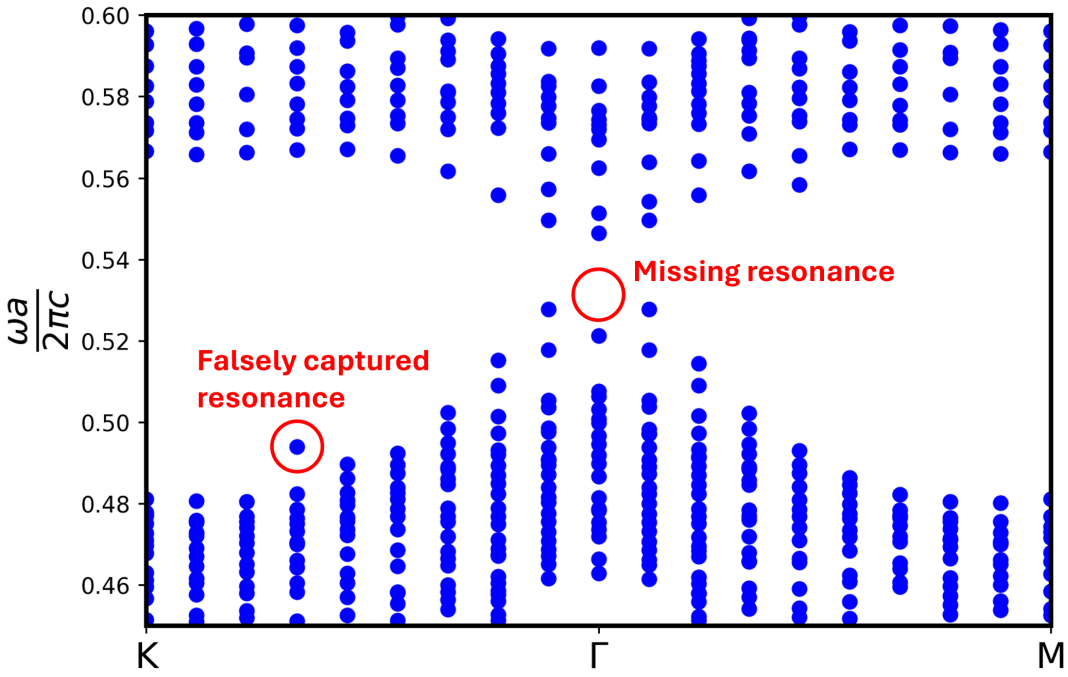


Figure 2.15 Band structure obtained by FDTD method of the photonic interface designed by Huang [53].

Part II

Research findings

3 Exploration of Chern Topologies for IR Photonics

The aim of this research is to develop and characterise topologically protected edge states suitable for photonic integration. At the beginning of the project, we chose to explore Chern-type topological states, since they offer a high degree of control over photonic modes. By tuning the difference between Chern numbers around a given photonic band gap, one can select the exact number of topologically protected edge modes that appear within the gap. This tunability makes Chern-type systems attractive for device applications. In addition, Chern topology does not require any special interface material, because air or vacuum is already topologically trivial, which simplifies fabrication and broadens the range of usable material platforms.

However, a fundamental limitation of Chern topology is that it requires breaking TRS. In photonics this is usually achieved with magnetic materials, which operate effectively only at much lower frequencies than the IR range targeted in integrated photonic platforms. This means that, although Chern systems seem promising from a theoretical point of view, the operating wavelength required for TRS breaking makes them unsuitable for practical IR devices. Metamaterials can generate artificial magnetism without magnetic materials, which at first seems to relax this requirement, but this would lead to designing a metamaterial out of a metamaterial and does not provide a fabrication-friendly or scalable solution. We also explored how far the material parameters can be tuned while keeping the topological phase intact, but the allowed parameter range does not permit a sufficient shift of the operating wavelength. As we will show, both natural and artificial magnetic approaches fail to produce practical Chern-type topological modes in the IR.

When we started the research, several design concepts for topologically non-trivial photonic crystals were already available. Our goal was to identify an optimal design, which could be a modification of an existing concept or a new structure. The motivation was to provide a flexible design framework, where a device engineer could specify the desired operating wavelength and the available materials, and our method would return a suitable topological crystal. During this exploration it became clear that Chern-type systems cannot meet the target wavelength constraints in integrated IR photonics, which leads to the need for an alternative approach.

Achieving such optimisation requires automation of the topological design process. A key challenge is the automated calculation of Chern numbers in photonic crystals. If a photonic band of interest crosses other bands, the Chern number cannot be assigned to a single isolated band and must instead be computed for the full group of bands involved in the crossing. As the geometry is tuned to explore design variations, the band structure evolves and new band crossings can appear. This makes it necessary to automatically detect such crossings, group the affected bands, and compute the correct total Chern number of the band group.

In this chapter we describe our exploration of Chern topologies and the extent to which the required conditions can be relaxed. We conclude that Chern-type

materials are not suitable for IR integrated photonics and motivate the need for an alternative approach based on OAL crystals, introduced in Chapter 4 and 5.

3.1 Band connection procedure

As discussed in the introduction, the symmetry of eigenmodes obtained from Eq. 1.8 plays a crucial role in two key aspects. First, it allows for the correct connection of eigenvalues to construct the photonic band structure, enabling the identification of band crossings, which are fundamental to understanding Chern topology.

To remind and summarize previous chapters, in this study we focus on transverse magnetic modes, as they are known to induce a photonic band gap [78, 79]. Specifically, we consider only the periodic component of the Bloch wave solution, denoted as $u_{\boldsymbol{k}}(\boldsymbol{r})$ (see Eq. 1.12), which is a two-dimensional complex field dependent on the spatial coordinate $\boldsymbol{r}$.

To compute the eigenmodes, we employ the MIT Photonic Bands Python library, available for macOS and Linux. Alternative approaches, such as COMSOL Multiphysics [80] or finite-difference time-domain (FDTD) solvers, can also be used. However, due to its high computational cost, FDTD is preferable only when accounting for materials with significant losses or dispersion.

In MPB, we utilize the built-in option to fix the phase of the eigenmode such that the real part of the field maximizes energy. This approach allows us to transform the complex function $u_{\boldsymbol{k}}(\boldsymbol{r})$ into a scalar two-dimensional array. Figure 3.1 illustrates examples of eigenfunctions obtained using this method, corresponding to the first twelve eigenvalues at the Γ point of a triangular photonic crystal composed of dielectric rings.

3.1.1 The need for the automated band connection

As mentioned in the earlier chapters, the correct identification of band crossings is essential for topological photonics, since it plays a crucial role in the calculation of the Chern number and the Wilson loop, which are used to classify the topological nature of our systems. The issue arises because the photonic band structure is obtained as a set of eigenvalues of the eigenproblem defined in equation 1.8. This eigenproblem is typically solved using MPB or COMSOL. However, in the case of MPB, the resulting bands are connected based on the eigenvalue index without considering the underlying symmetry. We illustrate this problem using an example known to exhibit a photonic band crossing, studied in [81]. The band structure computed with MPB is shown in figure 3.2. Panels a)–c) demonstrate that MPB incorrectly assumes an anti-crossing between the red and green bands along the $X - M$ path. An inspection of the corresponding eigenmodes along the $X - 0.5XM$ path in panel c) reveals a switch in eigenmode type, indicating that the bands are connected incorrectly. The result of our algorithm is shown in panel d), where the symmetry of the eigenmodes is taken into account, and the crossing is correctly identified.

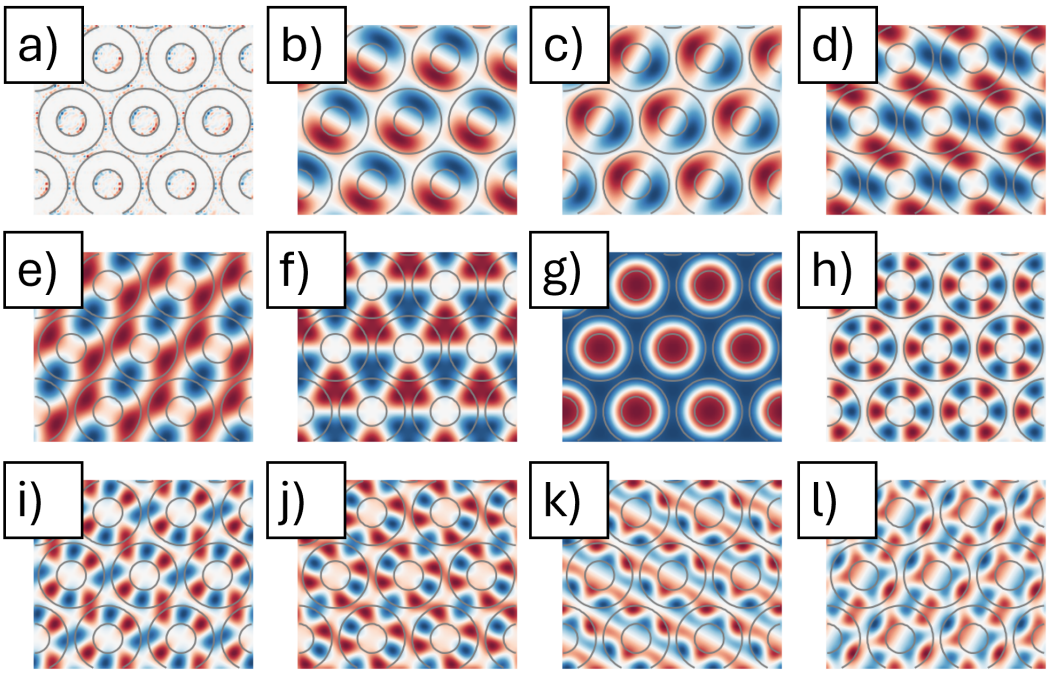


Figure 3.1 Visualization of periodic functions from the Bloch form in a photonic crystal composed of dielectric rings arranged in a triangular lattice. Each subfigure (**a**–**l**) represents a different standing wave mode, calculated at the Γ point. The red and blue color gradients indicate phase variations, while the black outlines highlight the structural elements.

3.1.2 Algorithm for automated band connection

To connect the bands, we employ the following strategy: we define a similarity distance between two eigenvalues at consecutive $\boldsymbol{k}$ points along the ζ path, where the ζ path connects high-symmetry points in the Brillouin zone (see Fig. 3.3). We split the path into segments between the points of high symmetry, for example path $\Gamma - X - M$ is split into segments $([\Gamma - X], [X - M], [M - \Gamma])$ and we operate on each segment individually. We then sequentially append eigenvalues to form a band [82]. Once this process is complete, we compute the average eigenfunction of the constructed band. This average eigenfunction is subsequently used in the next iteration of band formation. After each iteration, we check whether the average eigenfunction has changed. If it remains unchanged, the algorithm has converged. We then connect the bands on segments since they share the same edge points. The algorithm is illustrated in Fig. 3.4.

This algorithm is inspired by machine-learning clustering algorithms, where, instead of identifying a converged average eigenfunction, the goal is to find a stable center of mass for each cluster [83, 84].

We define the initial distance $d_{m,n,k}$ between the m-th eigenvalue at k and the n-th eigenvalue at $k+1$ as follows:

$$d_{m,n,k} \equiv \frac{|\hat{a}_{m,k} - \hat{a}_{n,k+1}|}{\langle u_{m,k}(\mathbf{r}) | u_{n,k+1}(\mathbf{r}) \rangle}, \tag{3.1}$$

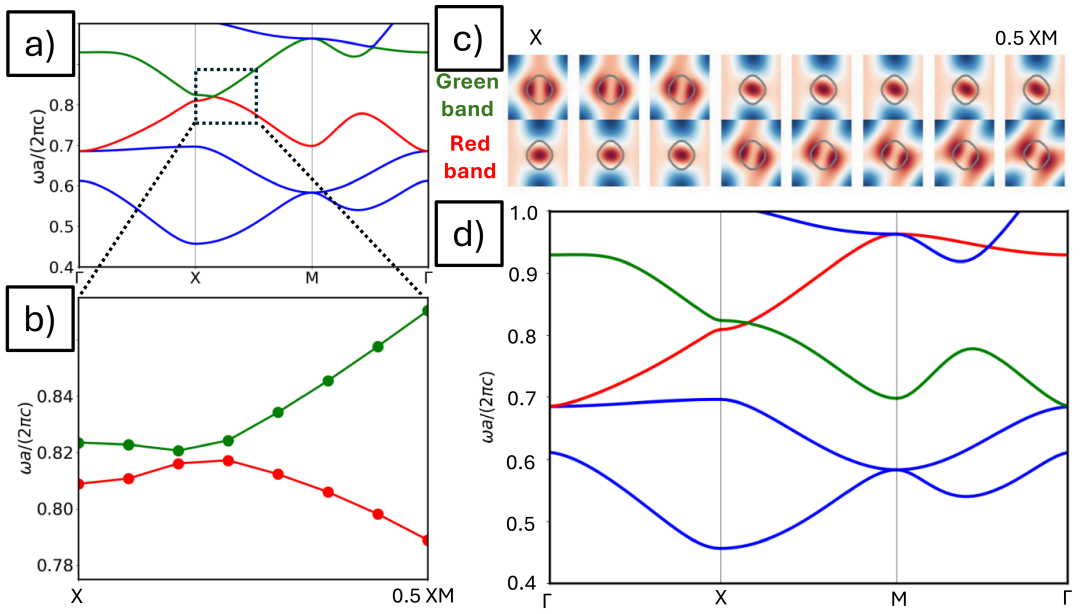


Figure 3.2 Illustration of the role of proper band connection, using a simple photonic crystal system that exhibits a band crossing [81]. The structure is a two-dimensional square lattice of dielectric rods with permittivity $\varepsilon = 7.2$ and radius $r = 0.2a$ in air. **a)** Band structure calculated with MPB, where bands are ordered only by eigenvalue index. An apparent anti-crossing can be seen between the red and green bands along the X–M line. **b)** Magnified view of the possible crossing region. The discrete eigenvalues at each k-point are shown as dots, with the corresponding eigenmodes presented in the (c) panel. **c)** Normalized field patterns of the eigenmodes from b). A symmetry change occurs after the third mode, revealing an incorrect band labeling caused by eigenvalue-only tracking. **d)** Corrected band structure produced by our automated method, which considers both eigenvalue closeness and mode similarity [82].

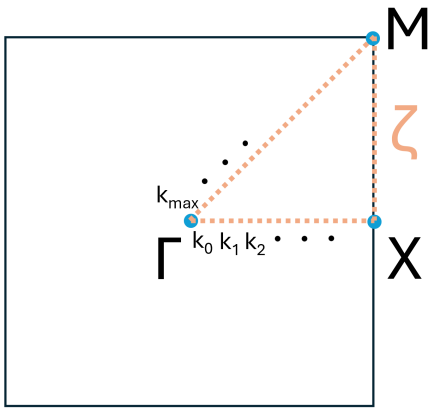


Figure 3.3 Illustration of the ζ path in the Brillouin zone, connecting high-symmetry points Γ, X, and M. The discretized $\boldsymbol{k}$ points along the path are labeled as $k_0, k_1, k_2, \ldots, k_{\max}$.

where $\hat{a}_{m,k}$ is the m-th eigenvalue obtained from Eq. 1.8 solved for k. Notice that k is no longer a vector, but rather the index of $\boldsymbol{k}$ along the ζ path segment. The term $\langle u_{m,k}(\mathbf{r})|u_{n,k+1}(\mathbf{r})\rangle$ denotes the scalar product of the two eigenfunctions, which in our case is a two-dimensional sum:

$$\langle u_{m,k}(\mathbf{r})|u_{n,k+1}(\mathbf{r})\rangle = \sum_{i,j=0}^{M-1} u_{m,k}\left[r_i, r_j\right] \cdot u_{n,k+1}\left[r_i, r_j\right] \tag{3.2}$$

Here, M is the spatial resolution of the eigenfunction defined in the MPB calculation, and $u_{m,k}\left[r_i, r_j\right]$ is the scalar value of the $u_{m,k}$ field at the (r_i, r_j) coordinate.

It is preferable to avoid initiating the appending process at a high symmetry point, as it is a common location for degeneracies. Instead, we select a starting point, k_{start}, along the ζ path based on the highest separation value. The separation value is defined as:

$$S_k \equiv \prod_{m=0}^{m_{max}-1} (\hat{a}_{m+1,k} - \hat{a}_{m,k}) \tag{3.3}$$

The separation value is defined to minimize the likelihood of two eigenvalues being close in energy.

Starting from the lowest eigenvalue, $\hat{a}_m = 0$, $k = k_{\text{start}}$, we construct the first band by minimizing the distance between eigenvalues, as defined in Eq. 3.1. We then proceed upwards in the eigenvalue index, removing already assigned eigenvalues from the available pool for subsequent appending. Once the initial band formation is complete, we compute the average eigenvector for each band segment:

$$u_i(\mathbf{r}) = \frac{1}{k_{max}+1} \sum_{k=0}^{k_{max}} u_{i,k}(\mathbf{r}) \tag{3.4}$$

Here, we introduce a new indexing variable, i, for the already sorted bands. Note that the indexing starts from 0 to ensure compatibility with later equations used in scripts.

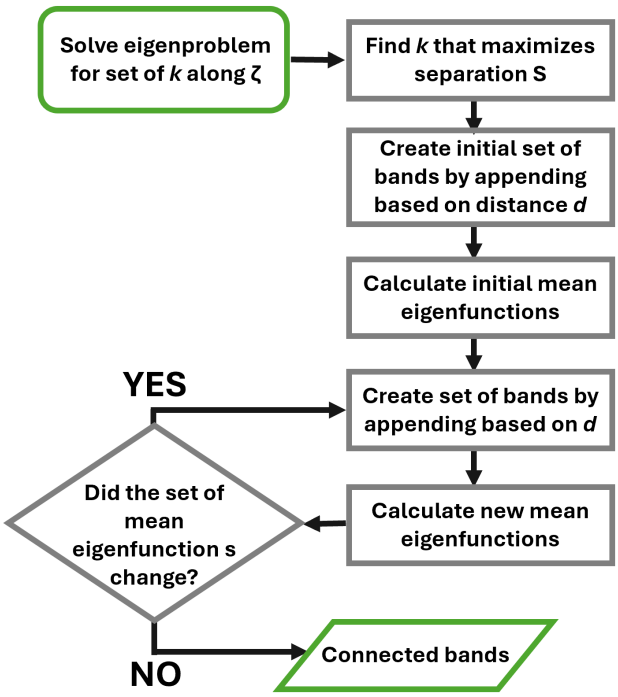


Figure 3.4 Flowchart of the band connection algorithm for individual $\boldsymbol{k}$-space segments. The process begins by solving the eigenproblem along the ζ path, selecting the $\boldsymbol{k}$ point with the highest separation S, and constructing an initial set of bands based on the distance d. The mean eigenfunctions are computed iteratively, and bands are updated based on $\bar{d}$. The algorithm repeats until the mean eigenfunctions remain unchanged, indicating convergence. Segments are finally stitched together at shared edge points to reconstruct full bands.

With this newly computed average eigenfunction, we can define the distance for the iterative process as:

$$\bar{d}_{i,n,k} = \frac{|\hat{a}_{i,k} - \hat{a}_{n,k+1}|}{\langle u_i(\mathbf{r}) | u_{n,k+1}(\mathbf{r}) \rangle}, \tag{3.5}$$

We now construct the bands based on $\bar{d}$, following the same procedure as with d, and compute a new set of average eigenvectors. If this new set matches the previous one, the iteration process terminates, indicating that the band segments have been correctly connected. If the sets differ, we continue iterating until convergence is achieved.

Once the band segments are stabilized, we can reconstruct the full bands by connecting them through endpoint matching. Since each high-symmetry point and its corresponding eigenfunction appear in two segments, we can use this redundancy for consistent connection. For example, Γ is included in both $[M - \Gamma]$ and $[\Gamma - X]$.

Connecting the bands enables the identification of potential band crossings by examining whether there exists a combination of two or more $\boldsymbol{k}$ points where the eigenvalue order reverses. Specifically, a band crossing is detected if, at one $\boldsymbol{k}$ point, $\hat{a}_{i,k_1} > \hat{a}_{j,k_1}$, while at another, $\hat{a}_{i,k_2} < \hat{a}_{j,k_2}$:

$$\operatorname{sign}(\gamma_{i,k} - \gamma_{j,k}) \neq \operatorname{sign}(\gamma_{i,k+1} - \gamma_{j,k+1})\,. \tag{3.6}$$

Using this criterion, we can select the set of intersecting bands for the overlap matrix (Eq. 1.20) to compute the Berry curvature.

With the automation of the topological invariant calculation, we can now proceed to investigate variations in material and geometrical parameters to identify topological phase transitions, material requirements, and the optimal geometry.

3.2 Problem of scale

The first problem we aimed to address is the material requirement for the Chern topological invariant to arise at frequencies and length scales suitable for integration. As mentioned in the introduction, non-trivial Chern numbers require an external magnetic field that produces off-diagonal elements in the permeability tensor and breaks time-reversal symmetry [85]. In two dimensions, the relative permeability tensor has the form

$$\mu_{\mathbf{r}} = \begin{bmatrix} \mu_{r,d} & \mu_{r,od} & 0 \\ \mu_{r,od} & \mu_{r,d} & 0 \\ 0 & 0 & 1 \end{bmatrix}, \tag{3.7}$$

where the indices d and od mark the diagonal and off-diagonal elements, which describe the gyromagnetic properties [86]. In [20], Blanco uses values of $\mu_{r,d} = 14$ and $\mu_{r,od} = 12.4i$, corresponding to yttrium iron garnet (YIG) [87], which is commonly used in magneto-optics and Chern-type photonic crystals.

YIG exhibits dominant permeability values (both diagonal and off-diagonal) between 10 and 100 MHz. Around 1.5 GHz, the off-diagonal component reaches approximately 1, and above 2 GHz it becomes effectively zero [88]. Since photonic crystals operate at wavelengths on the same scale as the lattice size [89], a frequency of 2 GHz corresponds to a wavelength of roughly 15 cm [90]. This already indicates a mismatch between the natural operation range of Chern photonic crystals based on YIG and the micron-scale wavelengths required for integrated photonics.

In this section, we systematically explore whether the material constraints of Chern systems can be relaxed so that the same topological phase survives with smaller permeability values and, ideally, at higher frequencies. We consider two related strategies:

(i) reducing the required magnitude of the gyrotropic permeability while keeping the same topological phase, and

(ii) modifying the unit-cell geometry to increase the overlap between the electromagnetic field and the gyromagnetic material, which should make the topological phase more robust and potentially reduce the required permeability values.

3.2.1 Material parameter scan around a reference Chern crystal

As a reference system, we use the design of Blanco [20], shown in Fig. 3.5. It is a simple square lattice with a single geometrical parameter, the radius r of a central cylinder, which makes it convenient for a systematic study.

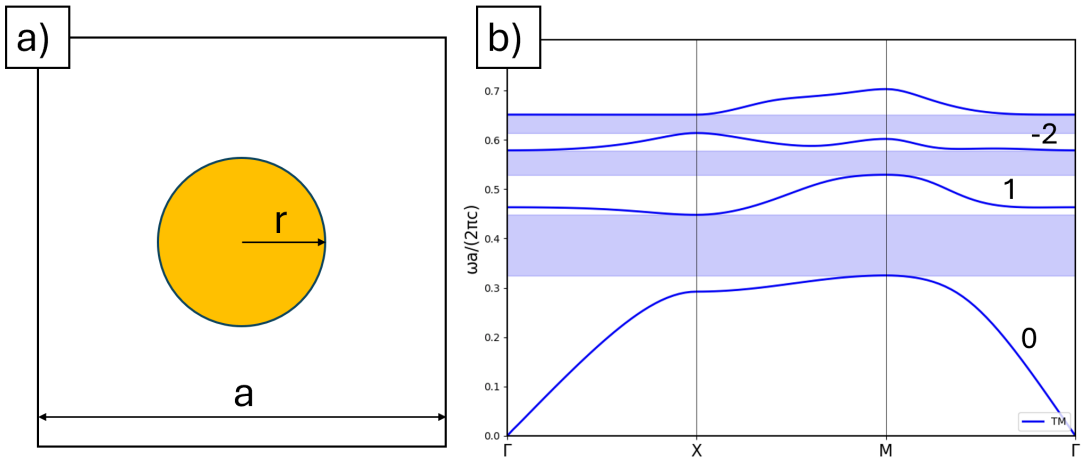


Figure 3.5 Chern photonic crystal acting as a topological insulator, designed by Blanco [20]. **a)** Geometrical definition of the square unit cell with lattice parameter a, containing a central cylinder with radius r. The material parameters are $\mu_{r,d} = 14$, $\mu_{r,od} = 12.4i$, and $\varepsilon_r = 15$. **b)** Band structure of the photonic crystal with the Chern numbers of the individual bands indicated.

For these parameters, the structure produces three separated bands with Chern numbers $(0, 1, -2)$ (see Fig. 3.5b). We use this configuration as a starting point and ask for which material parameters the same topological phase persists. Here, *topological phase* means that:

- the Chern numbers of the first three bands remain $(0, 1, -2)$, and
- the number of photonic band gaps between these bands remains unchanged.

The configuration space consists of the diagonal and off-diagonal permeability and the diagonal permittivity,

$$(\mu_{r,d}, \mu_{r,od}, \varepsilon_r) \in [0, 20]\,,$$

with the constraint $\mu_{r,od} \leq \mu_{r,d}$.

To investigate strategy (ii), we vary the radius of the central cylinder. Increasing r increases the overlap between the electromagnetic field and the gyromagnetic material, which intuitively should stabilize the topological phase. In other words, a larger portion of the field energy is stored inside the gyromagnetic region, so one might expect that smaller permeability values could still give rise to the same Chern phase.

3.2.2 Effect of field–material overlap

The boundaries of the topological phase for $r = 0.1a$ are shown in Fig. 3.6, and for $r = 0.15a$ in Fig. 3.7. Each point in these diagrams corresponds to a

material parameter set for which the band structure was calculated and the Chern numbers were evaluated. The size of the dots represents the size of the second photonic band gap.

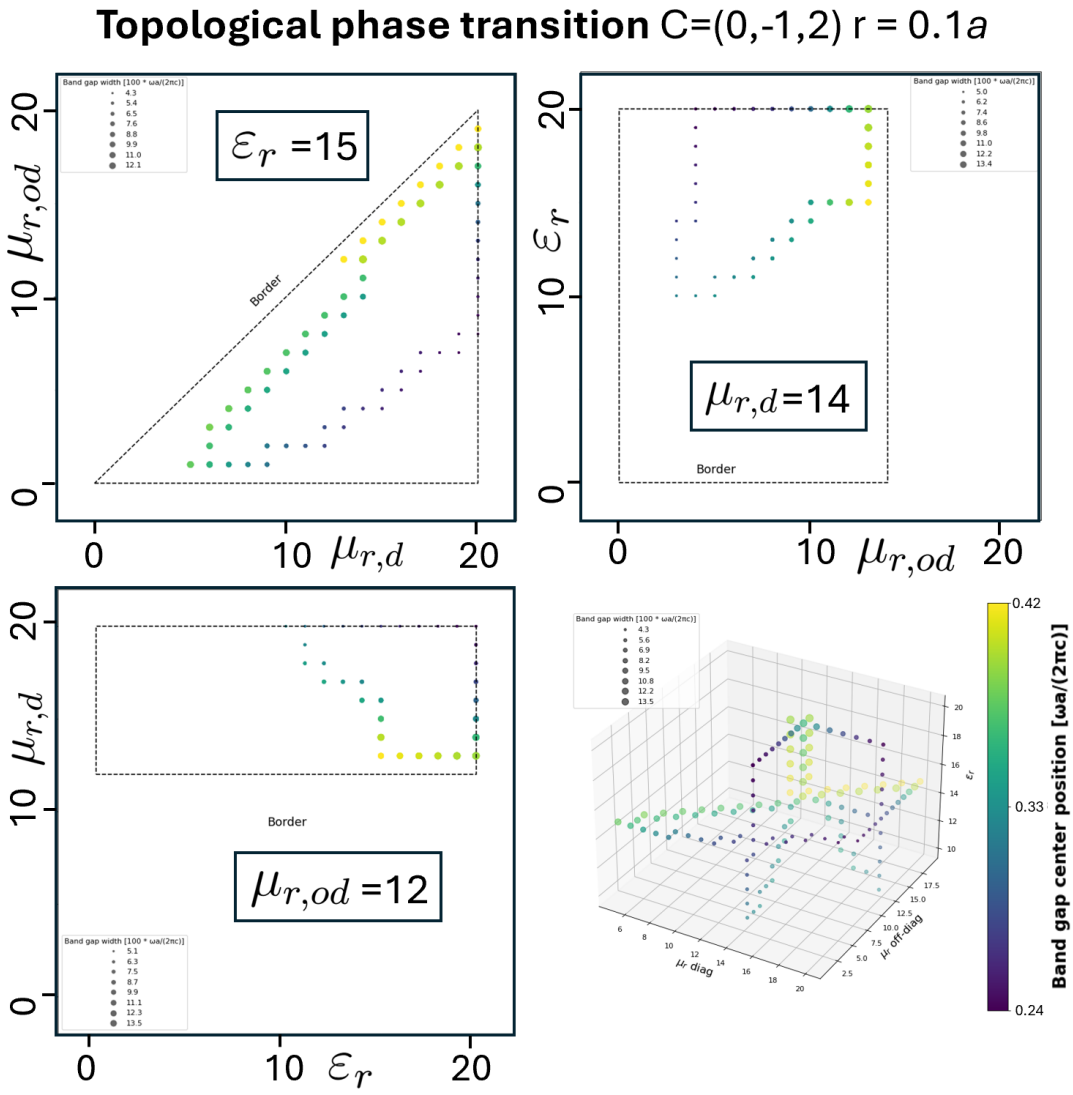


Figure 3.6 Boundaries of the topological phase $C = (0, 1, -2)$ in the material configuration space of a square lattice photonic crystal with a central cylinder of radius $r = 0.1a$. The size of the dots represents the size of the second photonic band gap (see Fig. 3.5b). The phase does not extend to small values of $\mu_{r,d}$ and $\mu_{r,od}$.

Comparing Figs. 3.6 and 3.7 shows that increasing the field–material overlap by enlarging the radius indeed enlarges the region in parameter space where the Chern phase $C = (0, 1, -2)$ exists. The topological phase becomes more robust against variations of $\mu_{r,d}$, $\mu_{r,od}$, and ε_r.

However, this effect has a clear limitation. Even for the larger radius and a finer sampling of the parameter space, the allowed region does not extend to small values of $\mu_{r,d}$ and $\mu_{r,od}$. In other words, although changing the geometry can make the phase more tolerant to parameter changes, it cannot reduce the required permeability values to be close to one. The Chern phase remains tied to strongly gyrotropic materials that are only available at microwave frequencies, and therefore to large wavelengths and lattice constants.

This analysis shows that strategy (ii), increasing the field–material overlap, helps to stabilise the Chern phase but does not solve the underlying scale problem. The topological phase cannot be shifted into a regime where the required permeability values are compatible with micron-scale operation.

3.2.3 Metamaterials as an alternative route

A natural alternative is to ask whether metamaterials could provide the required gyrotropic permeability at much higher frequencies. In [91], Singh reports sufficient values of permeability in the low THz region, pushing the wavelength down to about $600, \mu$m, which would correspond to a unit cell size of approximately $300, \mu$m.

In principle, such a material could be designed and optimised using the Lumerical FDTD solver. This tool allows the calculation of complex reflection and transmission coefficients (S-parameters) and the extraction of effective metamaterial parameters such as refractive index, impedance, permittivity, and permeability [92, 93]. One could then try to tailor the metamaterial response so that the effective permeability tensor matches the values required for a given Chern phase, but at higher frequencies.

However, this approach effectively amounts to building a Chern photonic crystal out of a material that is itself a complex metamaterial. The resulting structure would be a "metamaterial out of metamaterials", with several serious drawbacks:

- The fabrication would be extremely demanding, since one would need to pattern subwavelength resonant elements and then arrange them into a larger-scale photonic crystal.
- The extraction and control of the effective parameters would become highly non-trivial, especially when trying to preserve a specific topological phase across a wide parameter range.

For these reasons, although metamaterials offer a conceptual way to shift permeability to higher frequencies, they do not provide a practical route to simple and robust Chern photonic crystals operating at infrared or visible wavelengths.

3.2.4 Shift of focus to dielectric topological platforms

From the above investigation, we can draw a clear conclusion. Achieving Chern-type topological phases at higher frequencies (for example in the infrared or visible regimes) requires materials or metamaterials with large gyrotropic permeability. Such values are naturally available only in the microwave regime. Increasing the field–material overlap by geometric changes can expand the topological phase in the material configuration space, but it does not reduce the required permeability values enough to shift the operation frequency toward the optical range. Designing an additional metamaterial to artificially increase permeability at high frequencies would introduce a second level of structural complexity, making fabrication and parameter control prohibitively difficult.

Therefore, using the Chern formalism as the main design principle for topological edge-mode devices that should operate at micron-scale wavelengths and be

integrated on a chip is not feasible in practice. This motivates a shift to topological photonic platforms that do not rely on time-reversal symmetry breaking and do not require large gyrotropic permeability. In the remainder of this thesis, we therefore focus on such alternative platforms, in particular on obstructed atomic limit crystals, which can support edge modes in standard dielectric materials and at frequencies and length scales compatible with integrated photonics.

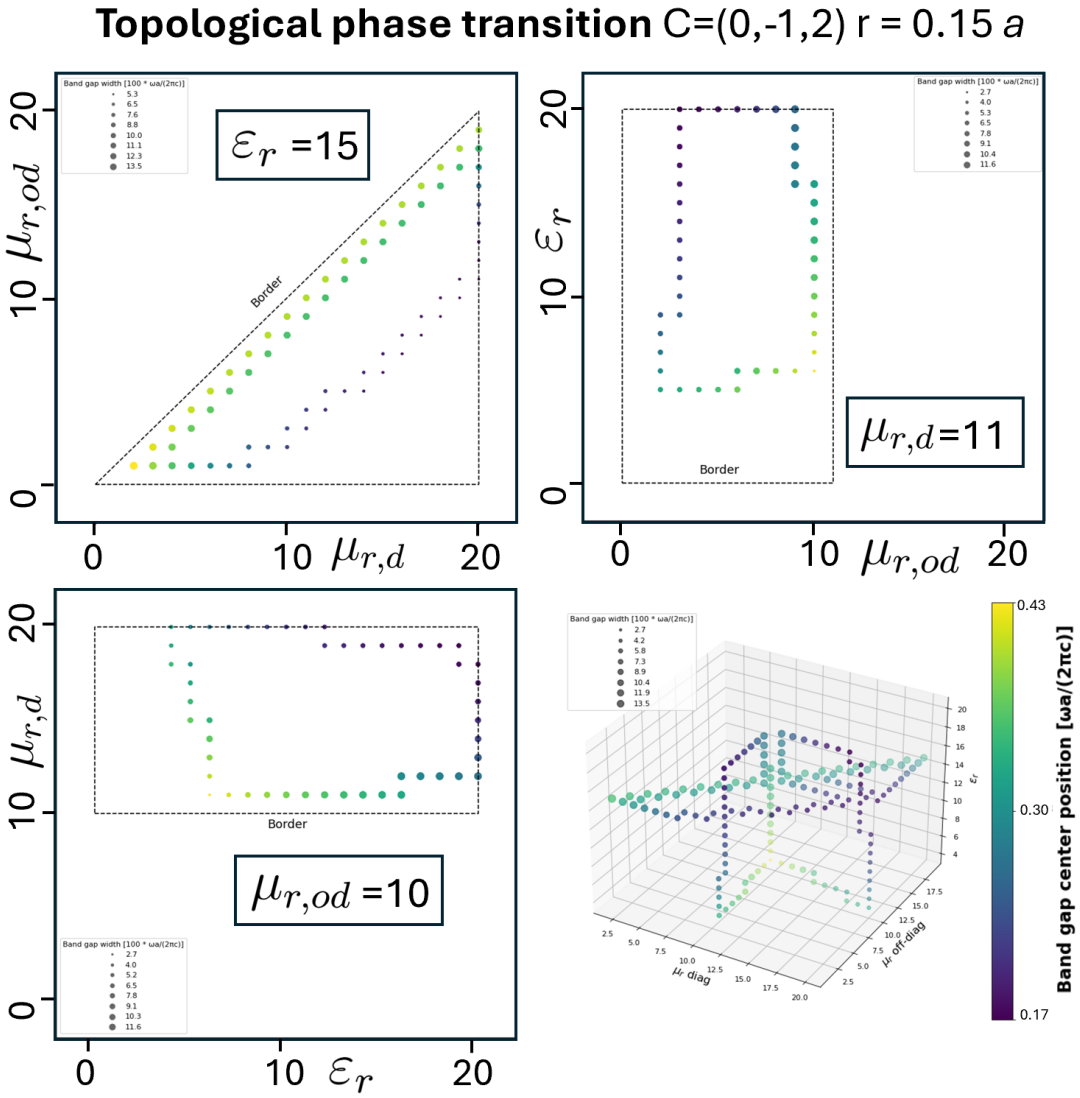


Figure 3.7 Boundaries of the topological phase $C = (0, 1, -2)$ in the material configuration space of a square lattice photonic crystal with a central cylinder of radius $r = 0.15a$. The size of the dots represents the size of the second photonic band gap (see Fig. 3.5b). Compared to $r = 0.1a$, the topological phase has expanded, but it still does not reach small values of $\mu_{r,d}$ and $\mu_{r,od}$.

4 Automated Detection of Band-Symmetry Inversions

The aim of this thesis is to move towards an application-ready, fabrication-friendly, and integrable design of a topologically protected interface. In the previous chapter, we established that Chern topology, the photonic equivalent of the quantum Hall effect, does not lead to integrable designs, since the material properties required to break time-reversal symmetry are not available in the optical or near-infrared spectral region.

This motivates the search for a different topological platform. We choose to investigate the obstructed atomic limit driven by eigenfunction-type inversion on an Indium Phosphide platform, targeting a wavelength of 1550 nm in a square lattice. While topological photonics commonly uses triangular lattices, this work aims to explore the properties of such modes in a square lattice. The C_4 lattice is particularly attractive for realizing such behavior due to its compatibility with orthogonal logic architectures [57, 94, 95]. Indium Phosphide was chosen because it is already widely used in photonic platforms [96, 97, 98].

To simplify the search for a suitable design, we need to automate the recognition of eigenmode order inversion. We will explore various parametrized geometric configurations of the photonic crystal unit cell, which can evolve through different lattice types during the optimization. Furthermore, we need to find a pair of photonic crystal unit cells that share a common photonic band gap to host the topological modes and have the same eigenmode types but in a different order around the band gap. These requirements complicate the standard approach based on field projections into symmetry operations, since the lattice symmetry group might not be known in advance. Moving away from symmetry-based classification and focusing on data-driven recognition enables us to investigate generative geometries that can give rise to various lattice types.

The goal is to create a procedure to analyze the dataset of eigenfunctions produced during the geometrical exploration of a given design and to identify whether a combination of geometrical parameters leads to eigenfunction order inversion with a matching pair around a specific band gap.

4.1 Band-symmetry recognition procedure

The central challenge in this problem is to identify corresponding eigenmodes across different geometries. Here, "different geometries" refers to different realizations of the same photonic crystal unit cell obtained by tuning the parameters that define its shape. For each fixed set of parameters the eigenmodes are orthogonal and their classification is straightforward. However, when the unit cell is modified, the resulting eigenmodes come from a different geometry and orthogonality between modes from the two cases is no longer guaranteed. To address this, we construct a set of *comparators*, which serve as reference functions. By evaluating scalar products between eigenmodes and these comparators, we can classify the modes into symmetry types and track the evolution of each mode across the parameter space.

4.1.1 Amplitude invariance via the sign function

A technical complication arises due to variations in eigenmode amplitude profiles introduced by the eigenvalue solver (in our case, MPB). Even for the same symmetry type, the relative amplitudes of lobes in an eigenfunction can vary with geometry, as shown in Fig. 4.1. Such inconsistencies make direct comparison unreliable. To resolve this, we define a transformed eigenfunction that retains only the sign of the field distribution:

$$v_i(\mathbf{r}) = \text{sign}\left(u_i(\mathbf{r})\right), \tag{4.1}$$

where $u_i(\mathbf{r})$ is the eigenfunction indexed by i and $v_i(\mathbf{r})$ is its sign representation. This transformation eliminates amplitude variations while preserving the essential spatial symmetry. All subsequent classification is carried out using $v_i(\mathbf{r})$ rather than the raw eigenfunctions.

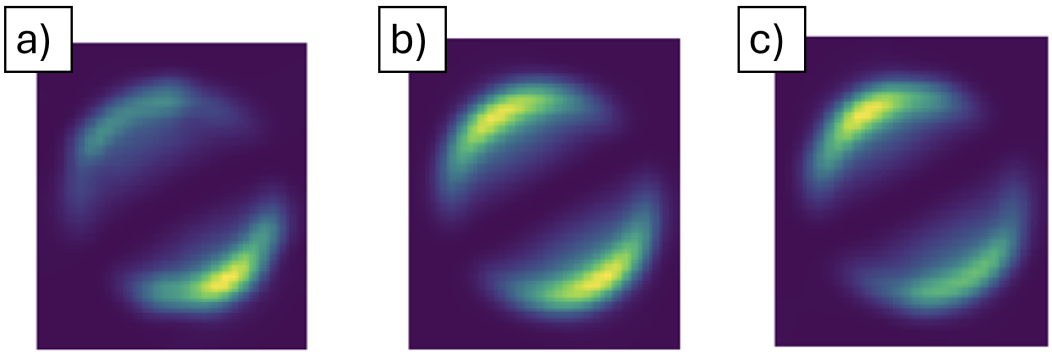


Figure 4.1 Demonstration of eigenfunction amplitude inconsistency in the same mode of a photonic crystal under geometrical variation, obtained using MPB. **a)** The bottom lobe exhibits a higher amplitude. **b)** Both lobes have equal amplitude. **c)** The top lobe exhibits a higher amplitude. In all cases, the underlying symmetry is identical, motivating the use of the sign function.

Since eigenmode symmetry is preserved along the band, it is sufficient to evaluate eigenmodes only at the Γ point, which simplifies the calculation.

4.1.2 Comparator-based mode recognition

Suppose we have a set of comparators $\{C_m(\mathbf{r})\}$, where each comparator represents a symmetry class from a specific point group symmetry, in our case C_4. To classify a given eigenmode $v_n(\mathbf{r})$, we compute scalar products with each comparator:

$$s_{m,n} = \sum_{i,j} C_m[i,j] \cdot v_n[i,j], \tag{4.2}$$

where the summation runs over the discretized spatial grid. If the maximum scalar product $s_{m,n}$ exceeds a predefined threshold, chosen as two-thirds of the total number of pixels r_e^2, then eigenmode v_n is assigned to comparator C_m:

$$\exists\, m \;\text{ such that }\; s_{m,n} > \tfrac{2}{3} r_e^2 \quad \Rightarrow \quad v_n \in \text{class}(C_m). \tag{4.3}$$

Otherwise, v_n remains unlabeled.

4.1.3 Predefined comparators from group theory

In the simplest case, the comparator functions can be defined using irreducible representations of the underlying point group symmetry. For example, in a C_4 lattice, the following comparators distinguish between s-, p-, and d-like modes:

$$C_{px}(\mathbf{r}) = \text{sign}(x), \quad C_{py}(\mathbf{r}) = \text{sign}(y),$$
$$C_{d_{xy}}(\mathbf{r}) = \text{sign}(xy), \quad C_{d_{x^2-y^2}}(\mathbf{r}) = \text{sign}(x^2 - y^2).$$

Here, C_{px} and C_{py} capture dipolar (p-like) symmetries along the x and y axes transforming as E irreducible representation (irrep), while $C_{d_{x^2-y^2}}$ and $C_{d_{xy}}$ capture quadrupolar (d-like) symmetries, transforming as B_1, B_2 irreps respectively. These classes correspond to irreducible representations of the C_4 group [99].

4.1.4 Comparator generation from the dataset

In many situations, the unit cell symmetry may not be known in advance. For example, when the geometry results from a generative design algorithm or when parameter tuning produces multiple symmetry types. In such cases, comparators must be generated directly from the dataset.

The procedure works as follows:

1. Initialize the comparator set $\mathbb{C} = \emptyset$.
2. For each eigenmode $u_n(\mathbf{r})$, compute its sign representation $v_n(\mathbf{r})$.
3. Compare v_n with all existing comparators $C_m \in \mathbb{C}$ using the scalar product.
4. If no comparator satisfies $s_{m,n} > \frac{2}{3}r_e^2$, then v_n is considered a new eigenmode type and is added to $\mathbb{C}$.

This ensures that $\mathbb{C}$ is incrementally constructed to capture the full symmetry diversity of the dataset.

To avoid contamination from atypical modes at the parameter space boundaries, it is advantageous to initialize comparators using eigenmodes from the central (average) geometry, which are most representative. Once this core set of comparators is established, edge-case eigenmodes can be classified reliably.

4.1.5 Identifying band-symmetry inversion

Once all eigenfunctions are consistently labeled, identifying band-symmetry inversion reduces to examining the eigenmode labels of the bands adjacent to a photonic band gap. If the order of these labels is inverted between two unit cell geometries that share a common band gap, the conditions for realizing an obstructed atomic limit are satisfied.

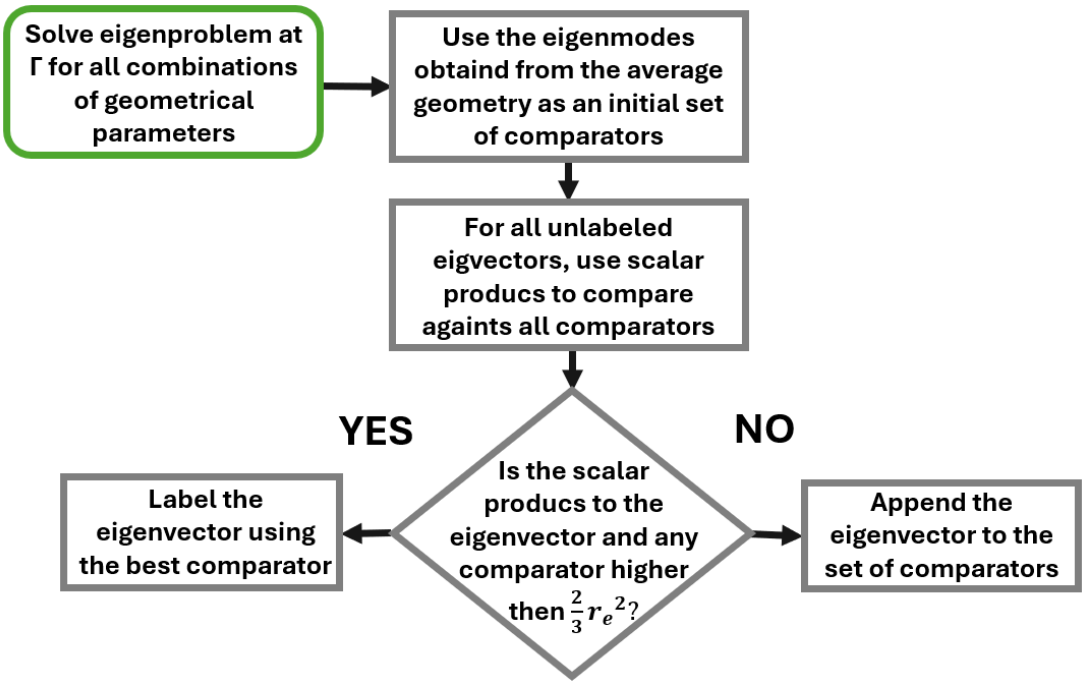


Figure 4.2 Flowchart of eigenmode labeling and comparator generation. The eigenproblem is solved at the Γ point for all geometries. Eigenmodes from the mean geometry initialize the comparator set. Each unlabeled eigenmode is compared to the comparators. If the scalar product with a comparator exceeds $\frac{2}{3}r_e^2$, the eigenmode is labeled accordingly. Otherwise, it becomes a new comparator.

5 Search for Eigenmode Inversions in C_4 Lattices

The objective of this chapter is to design a square-lattice photonic crystal that exhibits a full eigenmode order inversion in C_4 lattices. We begin with a qualitative analysis of the formation of topological phases, motivated by reports in the literature suggesting that band degeneracies, and consequently the closure of photonic band gaps, is accidental [51, 100, 101, 102]. Next, we show that band degeneracy and the associated band-gap closure can be deliberately induced.

The foundation of this chapter is based on the work of Xu et al. [51], who present topological phase diagrams for their designs. The photonic crystal considered here is a triangular lattice of dielectric cylinders, as illustrated in Figure 5.1. The authors present a band-symmetry inversion phase diagram that quantifies the energy difference between the p and d modes. However, we found it more insightful to examine the band gaps themselves and how they evolve with changing geometric parameters.

In Figure 2.5, we show that transitioning from a topologically trivial to a non-trivial state by varying geometric parameters requires the system to undergo a topological phase transition. This transition is characterized by the closure of the photonic band gap, as the band ordering around the gap must invert. This inversion occurs gradually as the geometry is varied. Raising the p modes above the d modes leads to a point where the p and d modes become degenerate and the photonic band gap closes. (In the referenced example, the gap closes at $\Theta = 122°$.)

By examining the band gap above specific bands across a range of geometric configurations of the photonic crystal unit cell, we can identify potential candidates for topological phase transitions by observing where the gap closes and immediately reopens. Such plots for the structure defined in Figure 5.1 are shown in Figure 5.2. We adopted this technique as a simplified approach for identifying potential topologically non-trivial candidates. By doing so, we can compute the band structure for various geometries within the configuration space and focus on the eigenfunctions only in the vicinity of band-gap closure regions.

Four of our designs are illustrated in Figure 5.3. The motivation behind the designs shown in Figures 5.3a and 5.3b lies in the idea that tuning the geometric parameters influences the effective lattice structure. For example, in the design shown in Figure 5.3b, if the cylinder radius r is fixed at an arbitrary value, small values of displacement d yield a regular C_4 lattice with lattice constant a. At $d = \frac{a}{2}$, the resulting lattice is still square, but it is rotated by $\frac{\pi}{4}$ radians and has a lattice constant of $\frac{\sqrt{a}}{2}$. Another perspective is to consider the coupling strength between the original unit cell and its neighbors: for small d, the intra-cell coupling dominates, whereas for larger d, the inter-cell coupling becomes stronger. This mechanism is similar to that employed in one of the foundational works in topological photonics by Wu and Hu on the honeycomb lattice [103, 50].

To describe this situation in more detail, which we do not pursue in this thesis, one could employ the tight-binding model (TBM) [104, 105]. The TBM offers a simplified yet effective framework to describe how energy, such as light in photonic

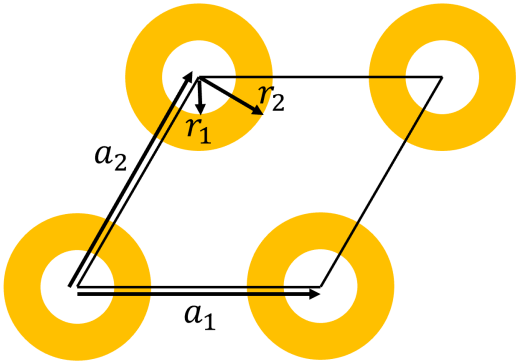


Figure 5.1 Schematic of a photonic crystal composed of rings arranged in a triangular lattice. The design follows the work of Xu [51], which employs a dielectric material with relative permittivity $\varepsilon_r = 9$. The configuration space is defined by the inner radius r_1 and the outer radius r_2 of the rings.

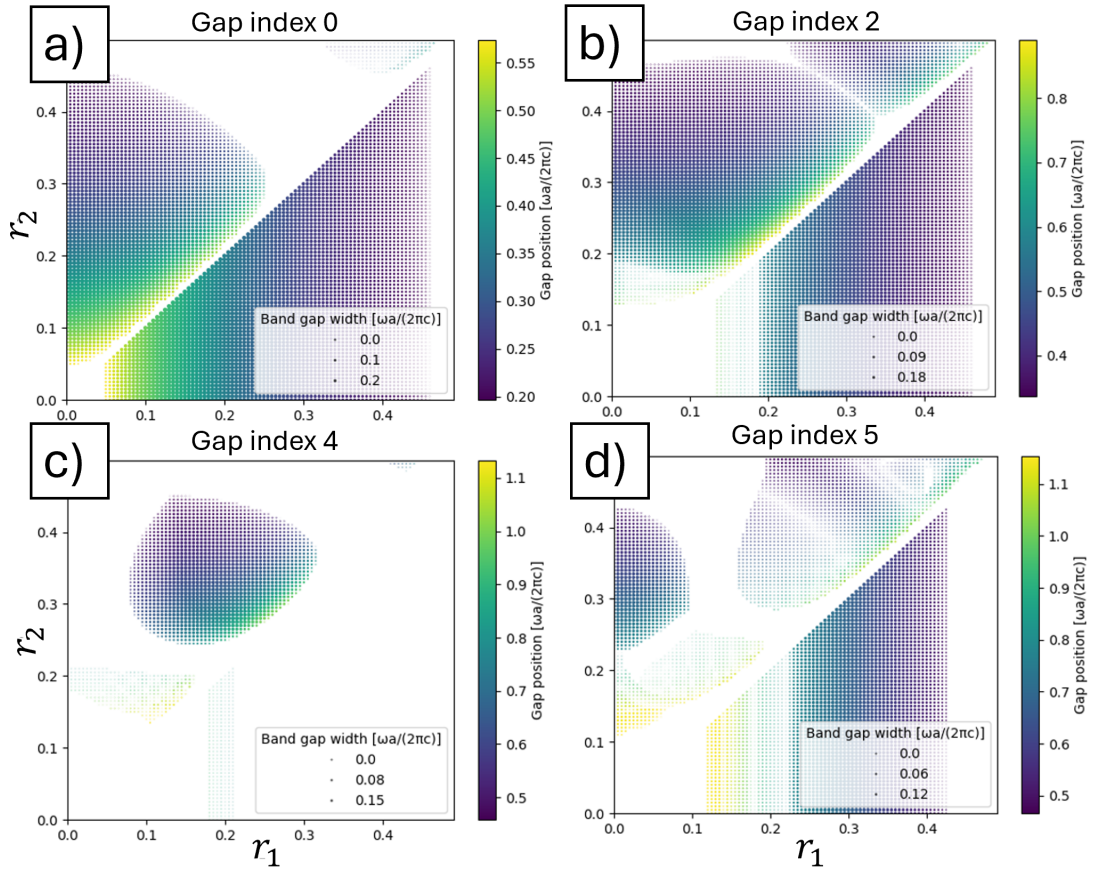


Figure 5.2 Photonic band gap characteristics of the structure proposed by Xu et al. [51], plotted as a function of the geometric parameters r_1 and r_2. The units of the variables used are given as fractions of the lattice parameter a. Each subplot corresponds to a distinct band gap, indexed by the lower photonic band (a: index 0; b: index 2; c: index 4; d: index 5). The color scale shows the central frequency (gap position) of the band gap in normalized units $\omega a/(2\pi c)$, while the dot size indicates the gap width in the same units. Only non-zero gaps are shown. The diagonal white region corresponds to the geometrical limit where $r_1 = r_2$, representing a vacuum with no structure. Below this limit, the material is inverted, meaning air rings embedded in a dielectric.

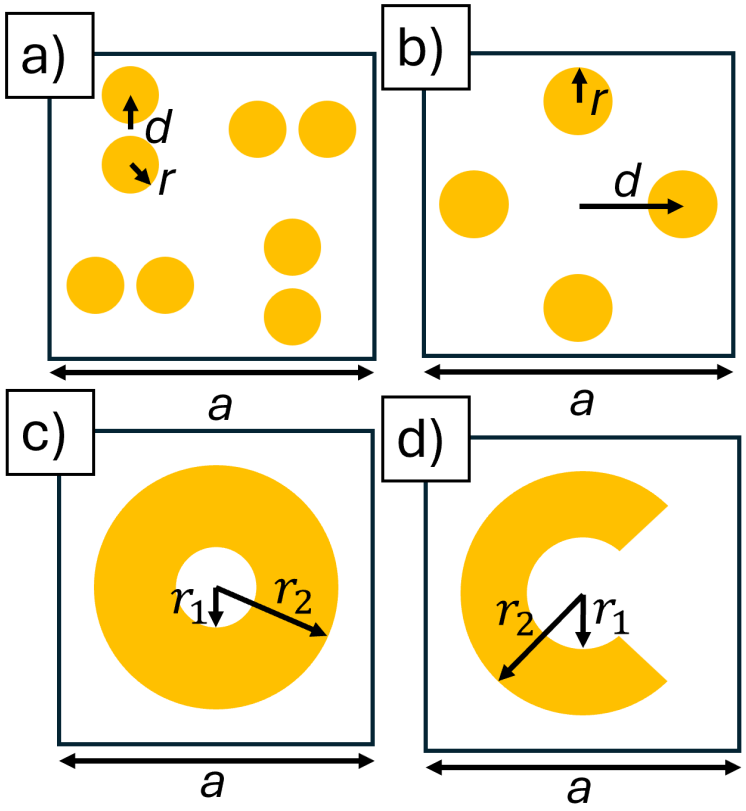


Figure 5.3 Schemes of various 2D photonic crystal square unit cell designs with lattice constant a. **a)** Array of cylinders displaced from a square grid by a distance d, with radius r. **b)** Cylinders positioned on a square grid with varying displacement d, and radius r. **c)** Concentric ring inclusion with inner radius r_1 and outer radius r_2. **d)** Circular sector inclusion with inner radius r_1, outer radius r_2, and an angular span of $\frac{3}{2}\pi$.

systems, propagates through a periodic structure by considering only localized modes at each site and their coupling to neighboring sites. The relative strength of these couplings, between sites within the same unit cell and those in adjacent cells, directly affects the band structure and can lead to topological features such as edge or corner states. By varying geometrical parameters that influence these coupling strengths, one can model transitions between different topological phases without solving the full electromagnetic problem for each configuration.

In Figure 5.3c, we examine how the behavior changes when the unit cell structure from Figure 5.1 is retained but the lattice type is altered. Figure 5.3d explores the consequences of reducing the symmetry of the design.

The design a from Figure 5.3 did not exhibit any indications of a potential phase transition, as there are no regions with band-gap closure followed by reopening, as shown in Figure 5.4. However, it is worth noting that the structure is capable of producing unusually large band gaps. In particular, Figure 5.4c shows a gap of 0.4 $\frac{\omega a}{2\pi c}$, spanning the energy range from 0.8 to 1.2 a/λ. In this Figure, only the gaps above bands with indices 3, 5, 7, and 8 are displayed, as not all bands can support a band gap directly above them.

To avoid including an excessive number of unnecessary figures, we note that

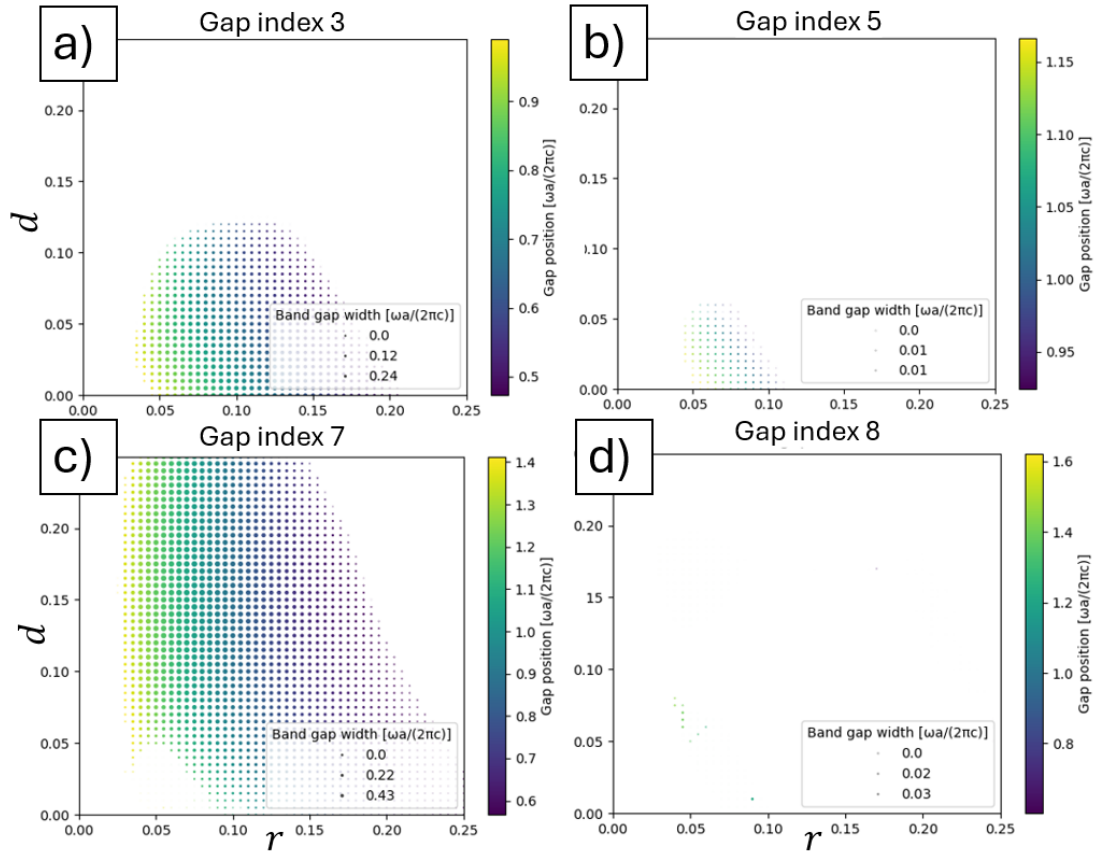


Figure 5.4 Photonic band gap characteristics of the structure defined in Figure 5.3a, shown as a function of the geometric parameters r (cylinder radius) and d (cylinder displacement). The units of the variables used are given as fractions of the lattice parameter a. The plots display the first four band gaps with indices 3, 5, 7, and 8 (band indices start from zero). The color scale represents the central frequency (gap position) in normalized units $\omega a/(2\pi c)$, and the dot size indicates the gap width in the same units.

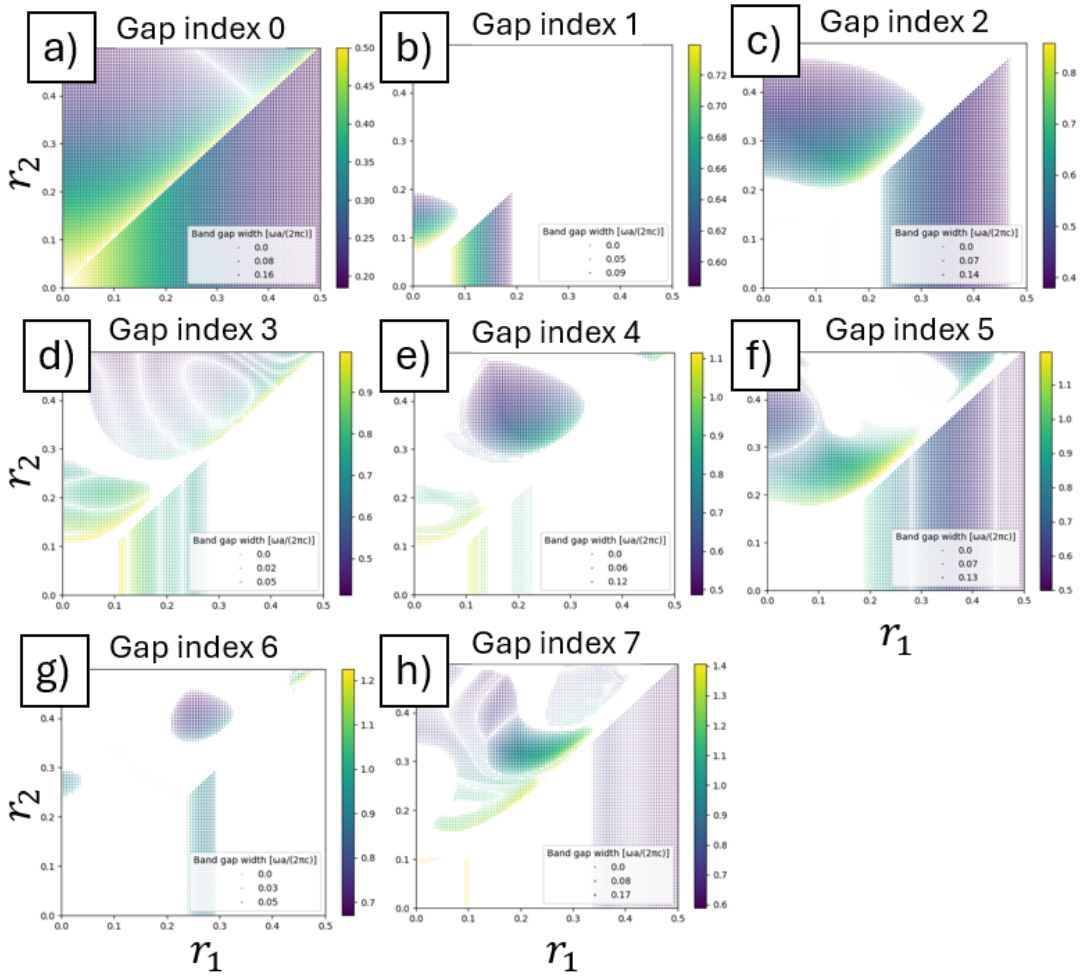


Figure 5.5 Photonic band gap characteristics of the structure defined in Figure 5.3c, shown as a function of the geometric parameters r_1 (inner radius) and r_2 (outer radius). Both radii are expressed in normalized units as fractions of the lattice parameter a. The plots display the first four band gaps with indices 3, 5, 7, and 8. The color scale in each panel indicates the central frequency (gap position) in the same normalized units used throughout the work, $\omega a/(2\pi c)$, and the dot size represents the corresponding gap width in these units. The region where $r_1 > r_2$ again corresponds to the material-inverted design described in Figure 5.2.

the study of design b from Figure 5.3 revealed some indications of gap closures and reopenings. However, the results were inconclusive.

The design c from Figure 5.3 exhibits a rich band-gap structure, as shown in Figure 5.5. Not only do all the bands form a band gap above them, but numerous line-like localized band-gap closures are also present. The most prominent example appears in Figure 5.5a. However, since this gap lies above the first band—which corresponds to a trivial field configuration—no band-symmetry inversion can occur there.

In Figure 5.5d, we observe several regions of line-like closures that suggest potential band-symmetry inversion. Nevertheless, the band gap in this case is very narrow, making it impractical for applications. For a topological band gap to be useful, it must reside within a sufficiently wide photonic band gap, as the spectral dispersion determines the operational bandwidth. The most promising

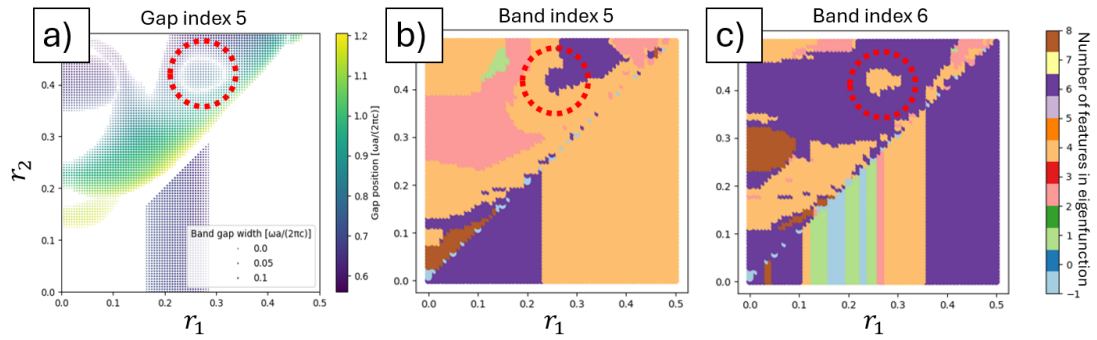


Figure 5.6 Analysis of band gap index five for the design defined in Figure 5.3d. **a)** Gap distribution over the parameter space defined by r_1 (inner radius) and r_2 (outer radius). The units of the variables used are given as fractions of the lattice parameter a. **b)** Number of field lobes in the eigenmodes corresponding to the band below the investigated band gap. **c)** Number of field lobes in the eigenmodes corresponding to the band above the investigated band gap.

candidate for band-symmetry inversion is shown in Figure 5.5h, where the band gap is sufficiently large and features gap closures with clear contrast.

Breaking the design symmetry in design d from Figure 5.3 yields qualitatively similar results to design c. We chose to highlight the behavior of band 5 in Figure 5.6, where an isolated region emerges around a band-gap closure. Using a method developed during the early stages of this research, we measured the number of field lobes present in the eigenfunction, which we will discuss further in Section 5.1.

In Figure 5.6a, a band-gap region—highlighted by a red circle—is separated from the surrounding configuration space by a line of band-gap closure. Analyzing the eigenmodes of the bands below (Figure 5.6b) and above the gap (Figure 5.6c) reveals that the number of field lobes in the eigenfunctions is reversed within this region, indicating a band-symmetry inversion. To realize topologically protected edge modes, we still need a couple of conditions: (i) establishing a boundary between the band-inverted crystal with a topologically nontrivial crystal having a regular ordering of eigenmodes; and (ii) the nontrivial crystal should have its band-gap overlaping with that of the crystal with band-symmetry inversion.

While this approach presents a possible pathway to discovering non-trivial photonic crystals, we have developed a more effective method, which will be introduced in Section 5.2.

5.1 Early versions of the mode clasification

In this section, we briefly describe our early attempts to classify eigenfunctions in order to identify band-symmetry inversion. As mentioned in Figure 5.6, one of our initial methods involved counting the number of field lobes in the eigenfunctions. This was done using the *measure* module from the *skimage* Python library, specifically employing the *find_contour* method, as illustrated in Figure 5.7.

We later improved this approach by introducing a machine learning-based clustering algorithm. The process begins by interpreting the eigenfunction (Figure 5.8a)

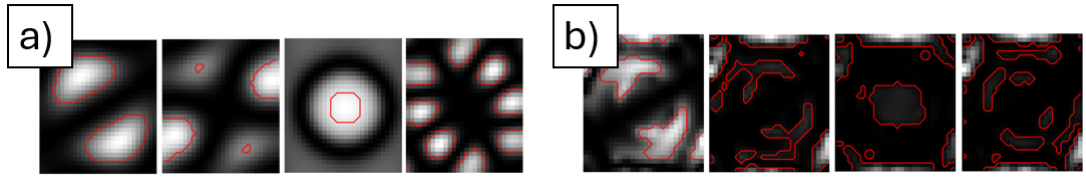


Figure 5.7 Demonstration of the use of the *skimage.measure.find_contour* function to identify the number of field lobes in eigenfunctions. **a)** Example where the method successfully detects distinct lobes. **b)** Example where the method fails due to noise or fragmentation of the eigenfunctions.

as a probability distribution and populating the domain with 1000 randomly sampled points based on this distribution (Figure 5.8b). These randomly distributed points retain the structural features of the eigenfunction and serve as input for the clustering algorithm. The algorithm then identifies clusters, classifies the points accordingly, and computes the cluster centers and standard deviations (Figure 5.8c).

Since the number of clusters—corresponding to the number of field lobes in the eigenfunction—must be specified in advance, we addressed this by calculating the total distance from each point to the nearest cluster center while incrementally increasing the number of clusters. The results are plotted in Figure 5.8d. Using the elbow method [106, 107], we can identify the point at which adding more clusters yields diminishing returns, allowing us to estimate the optimal number of clusters.

This method helped mitigate issues with scattered eigenfunctions, but its reliance on the elbow method makes it insufficiently reliable for our purposes. A typical result for a single geometry, where multiple eigenmodes are classified, is shown in Figure 5.9. In cases **e**, **f**, **i**, **j**, and **l**, the centroids were incorrectly placed, splitting individual lobes into multiple segments.

Even after introducing constraints on the possible number of field lobes in a square lattice, N_c, such that only an even number of lobes or a single lobe is permitted, the method remained prone to misclassification.

$$\{N_c \in \mathbb{Z} \mid N_c = 2k \text{ or } N_c = 1,\ k \in \mathbb{Z}\} \tag{5.1}$$

Searching for local maxima did not resolve the issue either, as some lobes give rise to multiple local maxima. This is particularly evident in Figures 5.10f and 5.10l.

The idea behind counting the number of field lobes in an eigenfunction was to identify similarities between eigenfunctions, which could then be used to group them into the same function type. The most developed version of this approach was the clustering method incorporating orientation deviation, as shown in Figure 5.11. This method was later replaced by a scalar-product-based approach, but the core concept of generating a set of comparators was retained.

5.2 Unit cell design

By analyzing the heuristically selected designs shown in Figure 5.3 and the corresponding eigenmode distributions from the classification procedure, we ob-

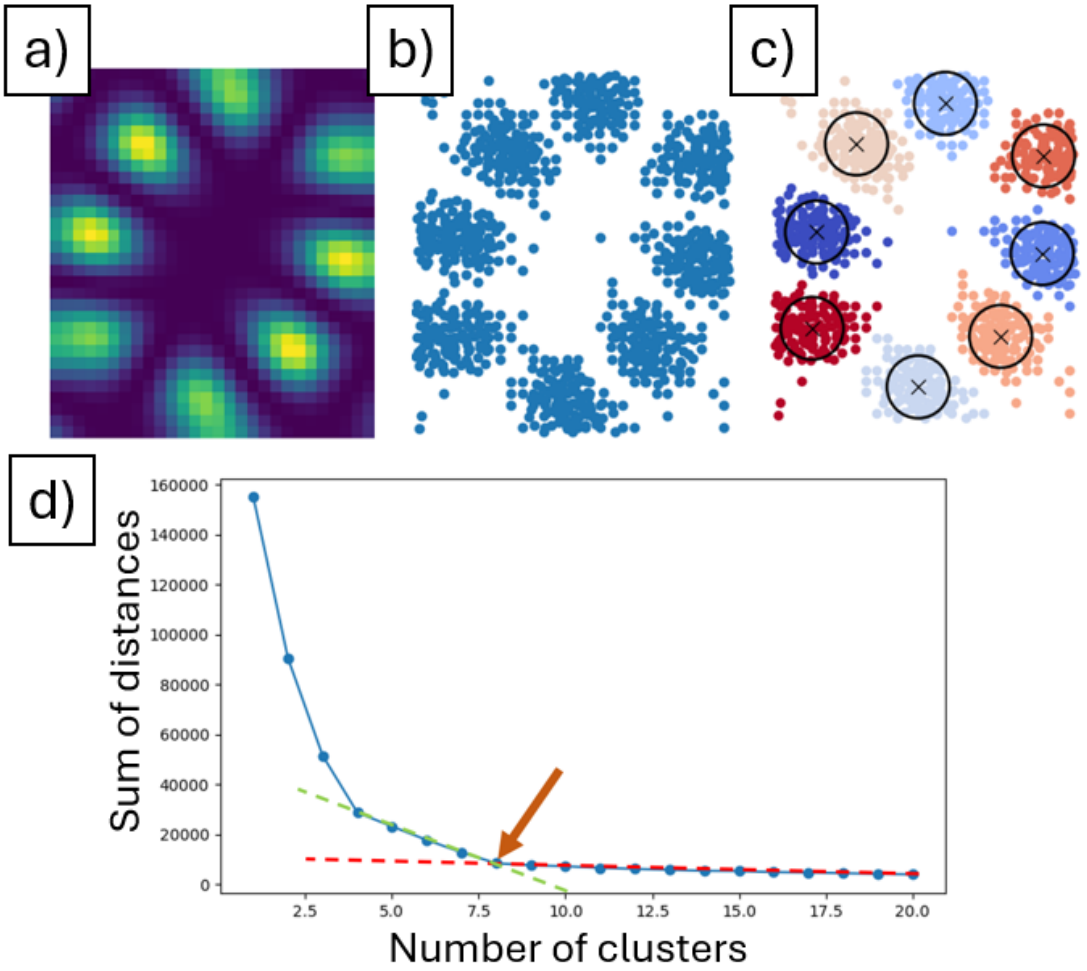


Figure 5.8 Use of a clustering algorithm to determine the number of field lobes in an eigenfunction. **a)** Photonic eigenfunction visualized as a 2D probability map, where brighter areas indicate higher probability density. **b)** 1000 points randomly sampled according to the probability distribution from a). **c)** Clustering applied to the sampled points, showing cluster centers (crosses) and standard deviations (circles). **d)** Elbow plot of within-cluster distances versus the number of clusters, indicating 8 as the optimal choice.

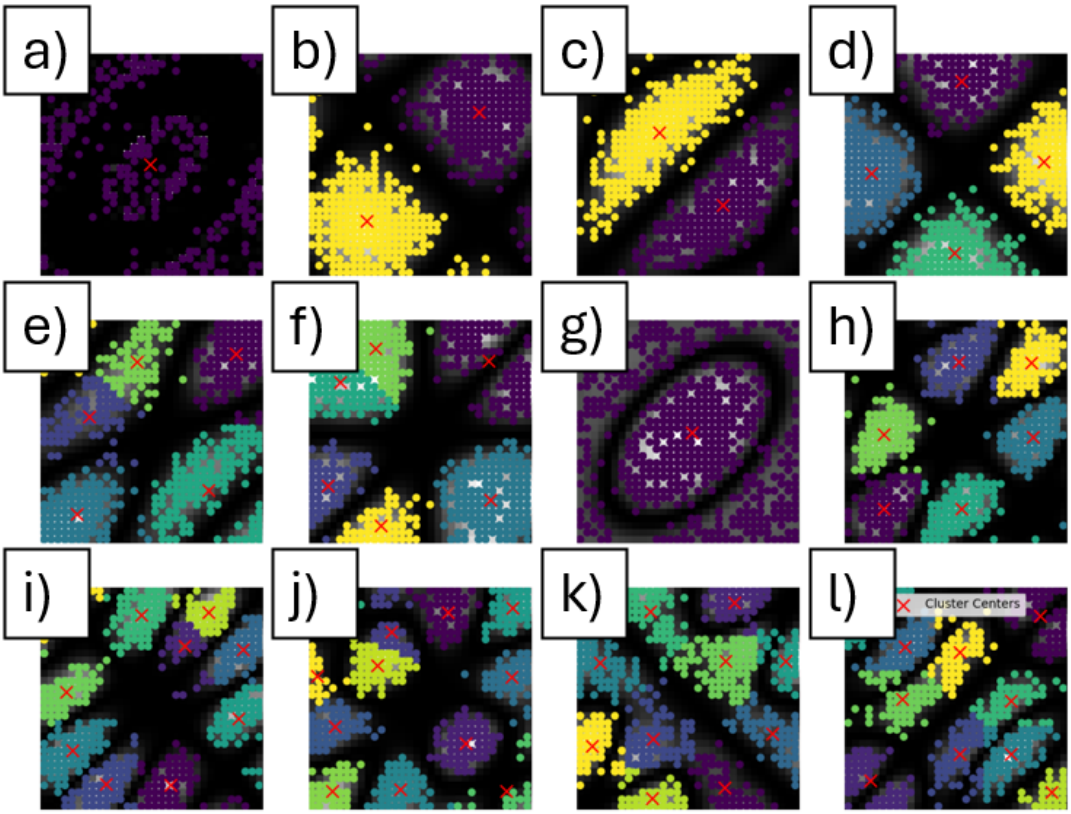


Figure 5.9 Demonstration of the clustering algorithm used for eigenmode classification. Cases **a**, **b**, **c**, **d**, **g**, **h**, and **k** were correctly classified, while the algorithm failed to correctly place the centroids in cases **e**, **f**, **i**, **j**, and **l**.

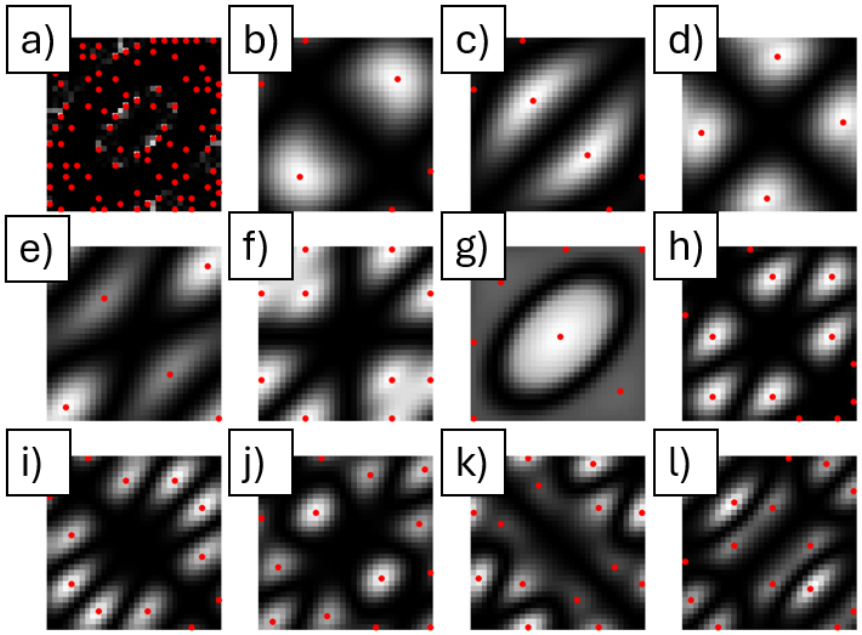


Figure 5.10 Use of a local maxima search algorithm for eigenfunction classification. Among all the presented cases, only case **d)** correctly identifies the field lobes.

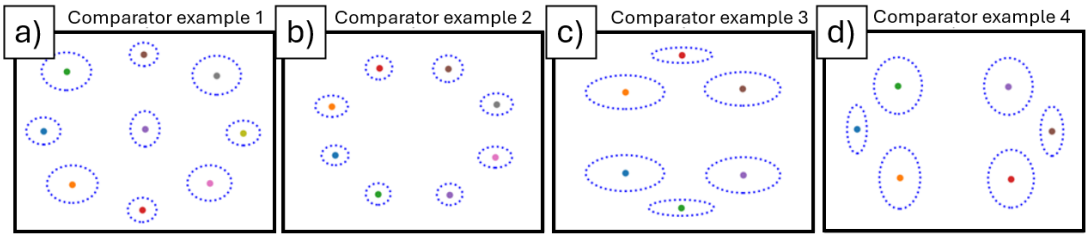


Figure 5.11 Examples of eigenfunction classification comparators based on a clustering algorithm, incorporating constraints on the number of field lobes per cluster and accounting for oriented deviation.

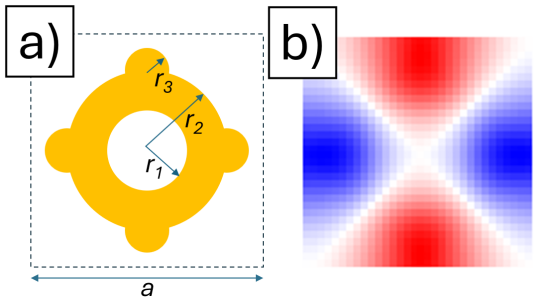


Figure 5.12 **a)** Photonic crystal unit cell design aimed at lowering the energy of the $d_{x^2-y^2}$ mode below that of the two p modes. **b)** The targeted d mode.

served that to lower the energy of a mode that would normally lie higher, it is necessary to increase the overlap between the eigenmode (field) and the material.

We tested this hypothesis in a design that combines features of Figures 5.3c and 5.3d. Specifically, we targeted the d-mode with the symmetry of an $x^2 - y^2$ function by adding material cylinders at the outer edge of the ring, positioned at points closest to the sides of neighboring unit cells. This configuration enhances the overlap between the material and the desired mode. The geometry used to implement this strategy is illustrated in Figure 5.12 [108].

The original ring serves as a base, ensuring that the eigenfunctions generated by the modified structure remain similar to those of the original (unaltered) ring. The four additional cylinders in the modified ring, which we refer to as "bridges," are introduced to enhance the overlap between the field lobes of the targeted eigenmode and the material in the unit cell. This increased overlap facilitates the formation of the mode, lowering its energy and thus shifting it downward in the band structure.

This effect is demonstrated in Figure 5.13, where we start with the design defined in Figure 5.12 and gradually increase the bridge radius from $r_3 = 0 \cdot a$ (representing the unmodified structure) to $r_3 = 0.2 \cdot a$. Figure 5.13a shows how the ordering of eigenmodes evolves with increasing r_3, revealing that even a modest increase to $r_3 = 0.1 \cdot a$ is sufficient to invert the mode ordering and push the $d_{x^2-y^2}$ mode below the p_x and p_y modes. The lines in the eigenmodes illustrate the underlying geometry of the unit cell. Figure 5.13b further shows how the band corresponding to the $d_{x^2-y^2}$ mode (highlighted in red) shifts to lower energy as a response to this geometric modification.

This approach enables the identification of potential designs that support band-symmetry inversion. However, to realize topologically protected edge modes, an

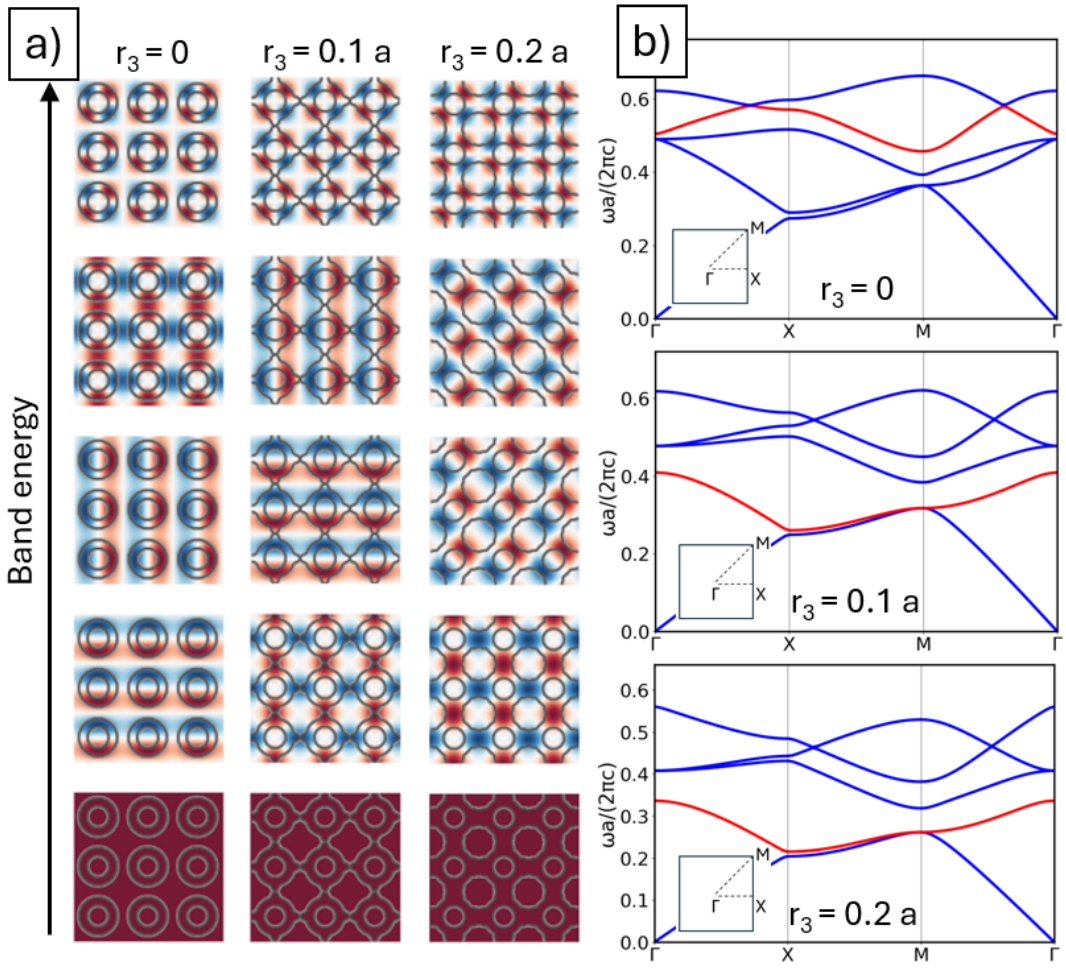


Figure 5.13 Demonstration of the material–field lobe overlap effect based on the design of dielectric rings with four bridging cylinders, as defined in Figure 5.12. **a)** Eigenmode ordering for different values of r_3, with the corresponding unit cell structures shown below each mode. **b)** Band structures of the geometries for varying values of r_3, with the band corresponding to the $d_{x^2-y^2}$ mode highlighted in red.

additional requirement is the existence of a complementary structure that produces the same type of modes in regular ordering. Moreover, both structures must exhibit photonic band gaps that share an overlapping region, and the inversion must occur within this gap. Meeting all these conditions presents a significant challenge due to the number of constraints involved.

To address this, our strategy begins with identifying a suitable design, such as the one shown in Figure 5.12, that can potentially lower the $d_{x^2-y^2}$ mode below the p modes and thereby enable a band-symmetry inversion. We then parametrize this design and explore the configuration space defined by the introduced parameters. Within this space, we quantify the degree of inversion using the algorithm described in Section 4.1.4. This allows us to identify regions where inversion is possible and where the relevant modes are located.

Once an inverted design is identified, we search our dataset for a complementary design that exhibits the same mode types in regular ordering and shares a band-gap overlap with the selected inverted design. In some cases, no suitable complementary design exists, while in others, multiple candidates may fulfill the criteria. When several candidates are available, we typically choose the one that maximizes the band-gap overlap, as this increases the likelihood that the resulting topological modes will lie within the common band gap. Placing the topological modes outside of the band gap would undermine the purpose of the design, since the mode could then scatter into other available modes at the same energy.

Finally, once both the inverted and complementary designs are identified and validated, we proceed with supercell characterization, as demonstrated in Section 2.1.3, to reveal the topological edge modes, their spectral position, and dispersion.

We explored the configuration space for the design shown in Figure 5.12, as illustrated in Figure 5.14. Since the structure is parametrized using three variables: r_1 (inner ring radius), r_2 (outer ring radius), and r_3 (radius of the side cylinders), we present only selected slices of the full configuration space. The color of each dot represents the energy separation between one of the p modes and the $d_{x^2-y^2}$ mode at the Γ point. White dots indicate configurations where these modes become degenerate at Γ.

At the Γ point, the p_x and p_y modes are automatically degenerate due to the C_4 rotational symmetry of the structure, which ensures equivalence between the x and y directions. The missing data points, particularly evident in the upper-right corner of Figure 5.14c, correspond to geometries for which the algorithm introduced in Section 4.1.4 failed to identify the relevant modes or the modes did not match the types required for comparison.

It is important to note that the inversion, as defined here, is evaluated only at Γ and does not guarantee a complete TM band gap. It measures mode separation at a single k-point. To assess whether a band-gap overlap exists, each geometry must be evaluated across multiple k-points to determine the true size and spectral position of the band gap.

As an example, we consider a scenario in which we select the geometry exhibiting the strongest inversion and pair it with its best band-gap overlap counterpart. The individual band structures for both designs are shown in Figure 5.15. The parameters for the regular structure are $[r_1 = 0.025 \cdot a,\ r_2 = 0.325 \cdot a,\ r_3 = 0.06 \cdot a]$, resulting in a geometry that is nearly a solid cylinder, with only a small central hole and minor protrusions at the edges. The inverted

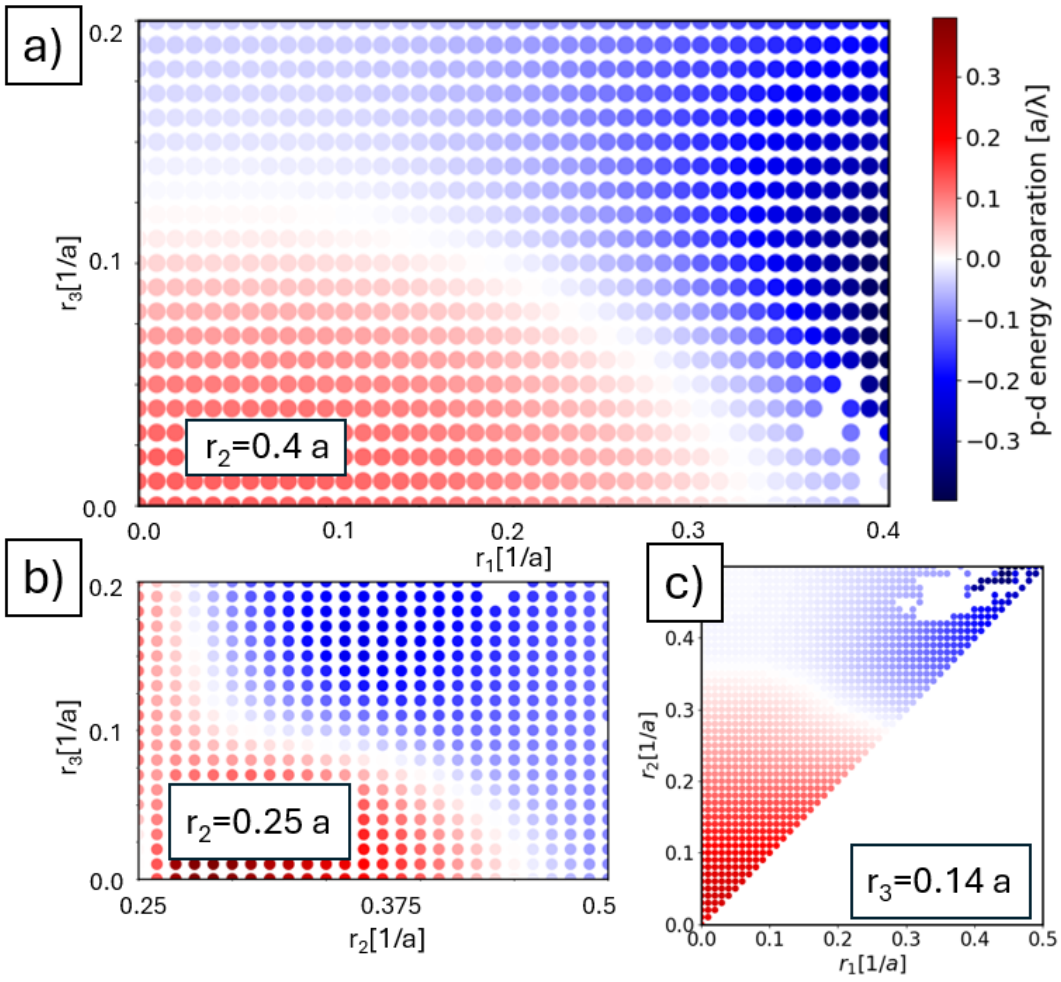


Figure 5.14 Band-symmetry inversion phase diagram for the ring with cylindrical bridges photonic crystal design defined in Figure 5.12. The color bar indicates the energy separation between the p_x mode and the $d_{x^2-y^2}$ mode at the Γ point. Three slices through the configuration space are shown. Missing values correspond to geometrical configurations where the algorithm described in Section 4.1.4 failed to identify the mode types or the required modes were not present.

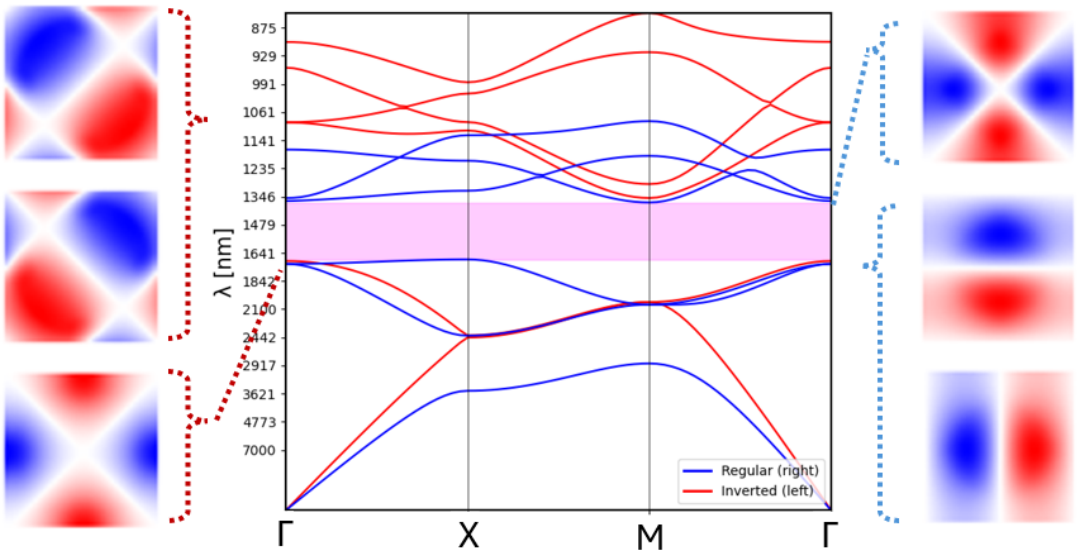


Figure 5.15 Band structure of the design exhibiting the highest degree of band-symmetry inversion and its complementary design, which yields the largest band gap overlap. Both designs are based on the structure defined in Figure 5.12. Regular structure parameters: $[r_1 = 0.025 \cdot a,\ r_2 = 0.325 \cdot a,\ r_3 = 0.06 \cdot a]$; inverted structure parameters: $[r_1 = 0.425 \cdot a,\ r_2 = 0.45 \cdot a,\ r_3 = 0.12 \cdot a]$. The material used is $\mathrm{InP}_{\lambda=1550\ \mathrm{nm}}$, with lattice constant $a = 700$ nm.

structure has parameters $[r_1 = 0.425 \cdot a,\ r_2 = 0.45 \cdot a,\ r_3 = 0.12 \cdot a]$, meaning that the ring is only $0.025 \cdot a$ thick and thus does not play a significant role. For future designs, this ring component may be omitted to simplify fabrication.

The material used is indium phosphide (InP), selected for operation at $\lambda = 1550$ nm, where the topological modes are expected to occur in a structure with lattice parameter $a = 700$ nm.

Interestingly, in this example, each side exhibits a different types of p modes. The regular design supports p_x and p_y modes, while the inverted design supports p_{xy} and p_{-xy} modes. Both sets of modes possess $\mathbb{C}_2$ symmetry but are rotated by $\frac{\pi}{4}$ with respect to each other. This can happen when the Wannier centers of the unit cell shift away from the geometric center.

Creating a supercell composed of 20 unit cells of each type of crystal results in a boundary between topoligically trivial and nontrivial geometries with the band structure shown in Figure 5.16. In this figure, the pair of red bands appearing within the previously shared band gap represents the new topologically protected modes generated by the band-symmetry inversion. Notably, unlike the topological modes shown in Figure 2.8, where the modes partially overlapped with the bulk bands and slightly breached the band gap, the modes here are centered within the band gap. This creates a fully isolated spectral region in which propagation is possible only via the topological modes, while both edges of this region remain gapped. Additionally, the topological bands produced by this geometric configuration appear to be relatively flat. This feature will be discussed in more detail in the following chapters.

Since we have not yet presented a transmission simulation of the modes that we claim to be topological, one might reasonably question whether these modes are, in fact, merely interface defect modes. To do this, we present a case in which

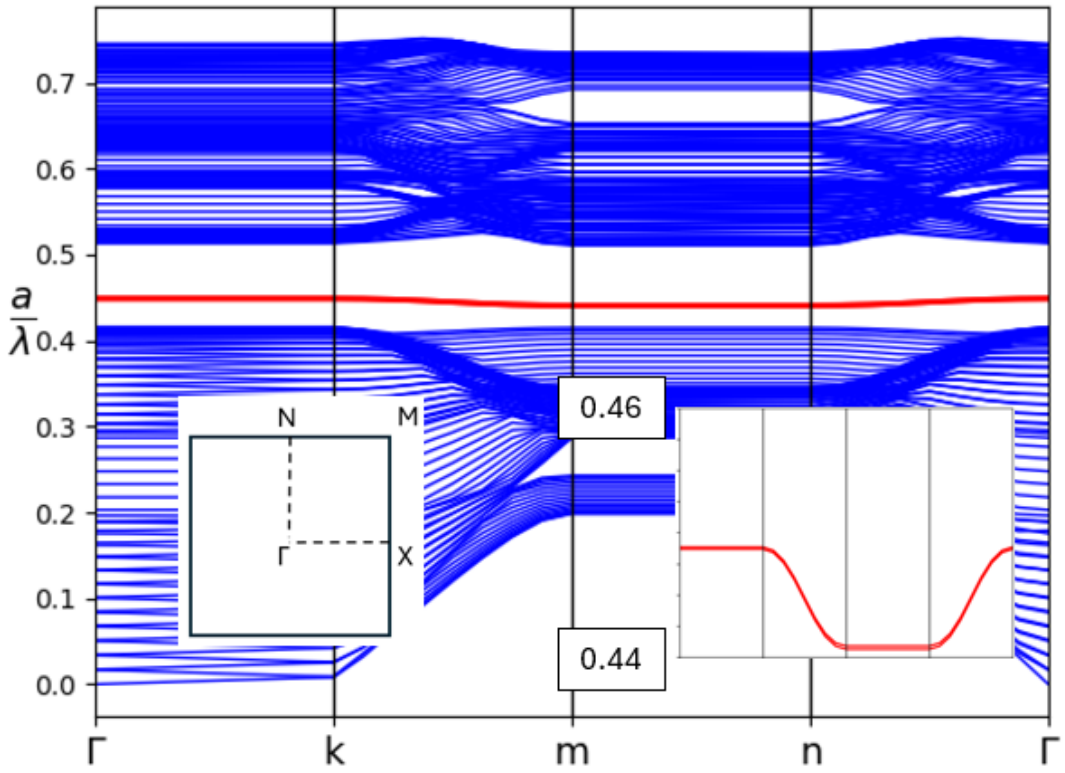


Figure 5.16 Band structure of a topological interface composed of 20 unit cells of each type defined in Figure 5.15. The two nearly degenerate topological modes are highlighted in red.

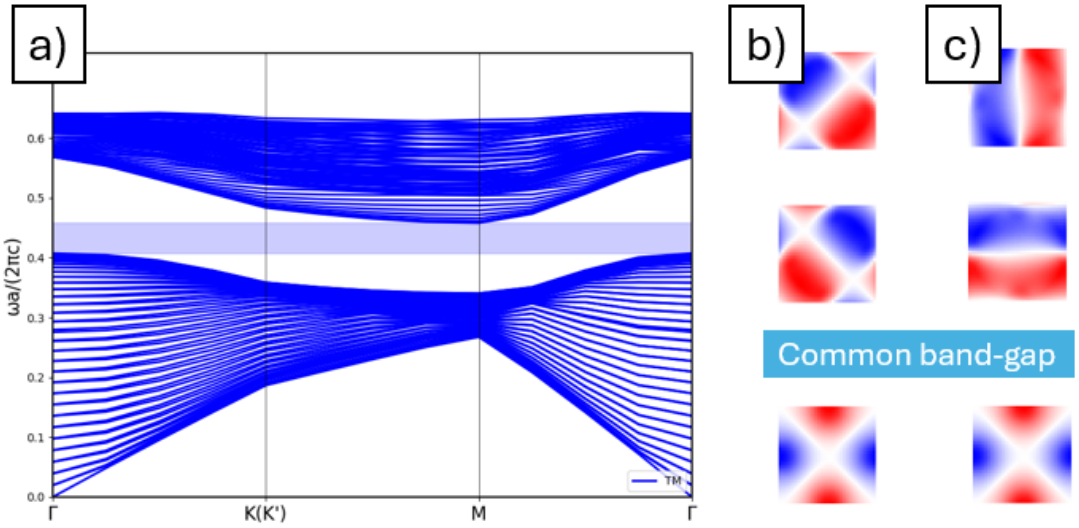


Figure 5.17 Band structure and eigenmode ordering of an interface formed by two geometries resulting in a band-symmetry inverted configuration. Left structure parameters: $[r_1 = 0.4 \cdot a,\ r_2 = 0.45 \cdot a,\ r_3 = 0.12 \cdot a]$; right structure parameters: $[r_1 = 0.425 \cdot a,\ r_2 = 0.45 \cdot a,\ r_3 = 0.06 \cdot a]$. The design parameters are defined in Figure 5.12. The material used is $\mathrm{InP}_{1550\ \mathrm{nm}}$, and the supercell forming the interface consists of 15 unit cells of each geometry type. A boundary between crystals belonging to the same topology class does not host in-gap modes. Therefore, the observed in-gap modes are not defect-related but topological.

an interface is created between two designs that share a photonic band gap. In this example, both designs produce sets of p modes that are rotated by $\frac{\pi}{4}$ relative to each other, as previously observed. Note, however, that in this case both designs are in a topologically non-trivial phase, meaning that both exhibit band-symmetry inversion and, therefore, no compensating edge modes are required. This scenario is shown in Figure 5.17a, while the corresponding eigenmodes are illustrated in Figures 5.17b and 5.17c. The images are arranged to match the energy ordering of the bands. Taken together, these results show that when two crystals belong to the same topological phase, no edge modes appear inside the band gap. This confirms that the modes observed in the previous section are not defect modes but arise from the topological mismatch between distinct phases.

5.3 Lattice-parameter matching using fractional ratios in photonic crystals

After exploring the parameter space to identify topologically inverted cases and their complementary designs, one of the main challenges we encountered was achieving a match between the band gaps of the inverted and regular structures. This issue has also been reported in the literature. Xu et al. [51] addressed the problem by designing the complementary structure using a different material, thereby shifting the band gap to align with that of the inverted case. Similar strategies were employed by Lai [109] and Sharma [110]. However, such approaches complicate the fabrication process and limit the practical applicability of these structures.

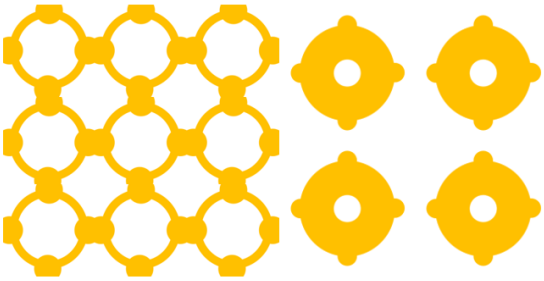


Figure 5.18 Demonstration of a photonic crystal with a lattice parameter ratio of 3:2 between the two structures.

Instead, we opted for a different solution. Rather than tuning the band gap by adjusting the material's refractive index, we leveraged the scalability of photonic crystals and varied the lattice parameter of one of the designs. Up to this point, we have described the photonic band structure in terms of the normalized frequency $\frac{\omega a}{2\pi c}$ or equivalently $\frac{a}{\lambda}$, which implies that the operating wavelength depends on the choice of lattice parameter. By allowing the lattice constants of the two designs to differ, we can shift a band gap that would otherwise have little or no overlap into a favorable position, enabling a usable overlap. An example of a 3:2 fractional lattice matching is shown in Figure 5.18.

The resulting interface band structure is shown in Figure 5.19. The number of bands that partially reach into the original photonic band gap appears to be equal to $n+m$ for a lattice parameter ratio of $n:m$. Notably, the number of unit cells around the interface does not affect the number of such bands.

Simulations involving fractional lattice parameter ratios require significantly more computational resources, due to the increased number of unit cells in the supercell. Even in the relatively simple 3:2 case, the unit cell count is three times higher than for a 1:1 configuration. For finer tuning of the band-gap alignment, such as with a 7:6 ratio, the computational load increases further, requiring seven times more unit cells. For this reason, we chose not to pursue further simulations of this type and instead focused on improving our configuration space search methods to identify designs that yield photonic band-gap overlap using a simple 1:1 ratio.

Although the observed modes originate from interfacing two photonic crystals in different topological phases, a valid question arises: could these modes instead be the result of local symmetry breaking due to lattice mismatch? While we did not perform transmission simulations for these modes, due to computational constraints and our prioritization of 1:1 lattice scaling, we present a case that addresses this question. Specifically, we constructed an interface between two topologically non-trivial geometries using a 2:3 lattice parameter ratio and observed no modes separating from the bulk bands.

The corresponding interface band structure is shown in Figure 5.20a, while the eigenmodes of the two designs are displayed in Figures 5.20b and 5.20c. Although the photonic band gap is relatively small in this case, this is due to the limited overlap between the band gaps of the two designs. The geometries are again based on the structure shown in Figure 5.12, with the following parameters: for the left structure, $[r_1 = 0.375 \cdot a,\ r_2 = 0.4 \cdot a,\ r_3 = 0.12 \cdot a]$, and for the right structure, $[r_1 = 0.425 \cdot a,\ r_2 = 0.45 \cdot a,\ r_3 = 0.12 \cdot a]$. The selected material is $\mathrm{InP}_{1550\ \mathrm{nm}}$,

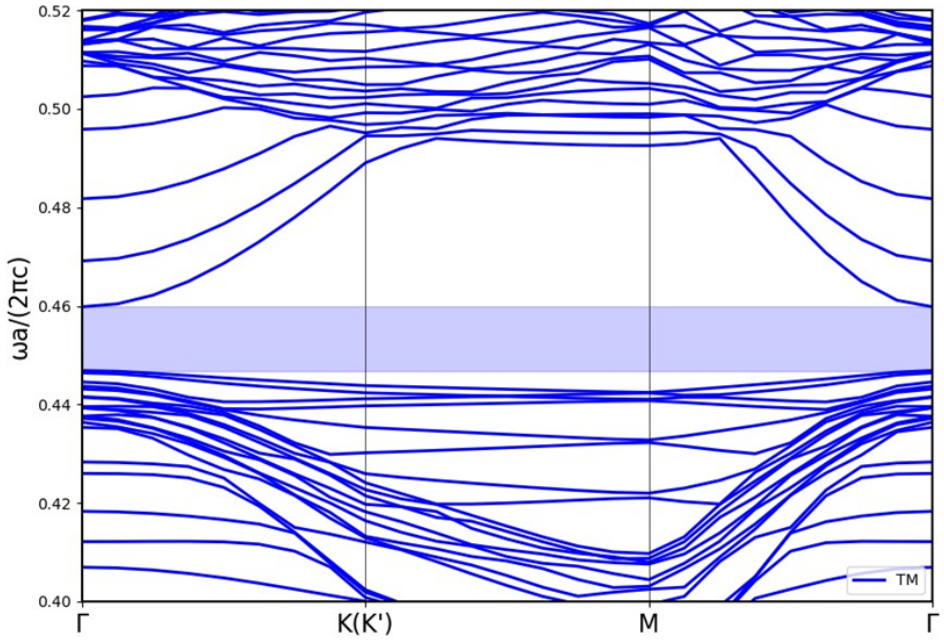


Figure 5.19 Band structure of a photonic crystal with a lattice parameter ratio of 3:2. The regular structure parameters are $[r_1 = 0.175 \cdot a,\ r_2 = 0.25 \cdot a,\ r_3 = 0.04 \cdot a]$, while the inverted structure parameters are $[r_1 = 0.425 \cdot a,\ r_2 = 0.45 \cdot a,\ r_3 = 0.14 \cdot a]$. The interface consists of five unit cell columns of each type. For lattice constants $a_{\text{regular}} = 750$ nm and $a_{\text{inverted}} = 500$ nm, and using $\text{InP}_{1200\text{nm}}$ as the material, the resulting common band gap spans from 1000 nm to 1270 nm.

and the lattice constant is $a = 1000$ nm.

In conclusion, although we did not perform the necessary transmission simulations to confirm the robustness of the modes against defects, our results strongly indicate that fractional lattice-parameter matching is an effective strategy to achieve the desired photonic band-gap overlap.

One important consideration when using this technique is that it inherently produces more bands. If the intended application requires only a single mode to be present at a specific energy, then only a portion of the edge band can be utilized. For example, in Figure 5.19, we presented an interface band structure that includes five bands resulting from fractional lattice-parameter matching. Among these, only the lowest band can be spectrally isolated, meaning that only the 0.46–0.468 a/λ spectral region is suitable for a single-band application.

5.4 Generative geometry approach to unit-cell design

In this section, we briefly discuss the idea of automatically generating the geometry based on the desired band structure ordering. The aim was to construct photonic crystal unit cell geometries directly from the symmetry and spatial distribution of the eigenmodes, rather than specifying the geometry manually and

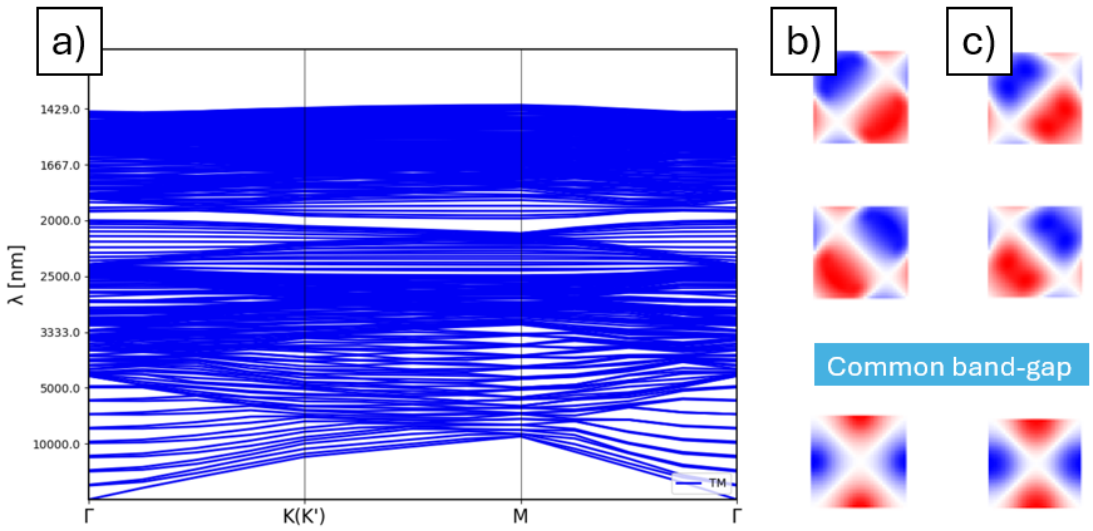


Figure 5.20 Band structure and eigenmode ordering of an interface formed by two geometries resulting in a band-symmetry inverted configuration. Left structure parameters: $[r_1 = 0.375 \cdot a,\ r_2 = 0.4 \cdot a,\ r_3 = 0.12 \cdot a]$; right structure parameters: $[r_1 = 0.425 \cdot a,\ r_2 = 0.45 \cdot a,\ r_3 = 0.12 \cdot a]$. The design parameters are defined in Figure 5.12. The material used is $\mathrm{InP}_{1550\ \mathrm{nm}}$.

then evaluating its optical properties. The motivation was to explore whether a generative method can be used to make the dielectric pattern emerge naturally from the desired field characteristics, emphasizing the overlap between the eigenfield profiles and the material distribution.

Although this approach was used in some exploratory designs, it did not lead to a geometry in which both d modes lie below the p modes. Despite this observation, this strategy represents an interesting concept which is worth further investigating beyond its initial exploration in this thesis.

The core idea of this approach is to define a "fitness" measure that rewards alignment between the field intensity $|\mathbf{E}|^2$ and the dielectric distribution $\varepsilon(\mathbf{r})$. Regions of high field intensity should coincide with high permittivity for the modes intended to shift to lower frequency, and with low permittivity for those intended to shift higher. This principle defines a generative process that iteratively modifies the geometry to maximize the field–material overlap associated with the desired mode ordering.

5.4.1 Mathematical formulation

Let $u_{\mathbf{k},i}(\mathbf{r})$ denote the i-th eigenmodes and $\varepsilon(\mathbf{r})$ the dielectric function to be determined. The eigenfrequencies ω_i relate to the eigenmodes through the operator $\hat{\boldsymbol{A}}(\boldsymbol{r})[\#]$ defined in chapter 1:

$$\hat{\boldsymbol{A}}(\boldsymbol{r})[\#] = \nabla \times \left[\frac{1}{\varepsilon_r(\boldsymbol{r})} \nabla \times \# \right], \tag{5.2}$$

which depends on $\varepsilon(\mathbf{r})$. The goal is to find $\varepsilon(\mathbf{r})$ such that the ordering of the low-lying eigenfrequencies produces the desired p–d inversion.

Instead of solving this as a full inverse problem, we used a simplified heuristic approach based on a score function S, which rewards configurations where regions

of high permittivity overlap with the desired (p-like) modes and avoid overlap with the undesired (d-like) ones:

$$S = \min!\left(\langle\varepsilon|u_p|\rangle\right) - \max!\left(\langle\varepsilon|u_d|\rangle\right), \tag{5.3}$$

where

$$\langle\varepsilon|u_i|\rangle = \int \varepsilon(\mathbf{r})|\psi_i(\mathbf{r})|\mathrm{d}\mathbf{r} \tag{5.4}$$

is the spatial overlap between the dielectric distribution and the field amplitude of mode i. The optimization aims to maximize S by modifying $\varepsilon(\mathbf{r})$ pixel by pixel.

An initial geometry estimate was defined from the four lowest modes at the Γ point (p_1, p_2, d_1, and d_2) as

$$G_0(\mathbf{r}) = \mathrm{sign}!\left(\alpha_1 d_1 + \alpha_2 d_2 - \alpha_3 p_1 - \alpha_4 p_2\right), \tag{5.5}$$

where α_n are adjustable weights that determine the relative influence of each mode. The binary pattern $(G_0 + 1)$ defines the initial dielectric layout used as the starting point for optimization.

5.4.2 Algorithmic implementation

The algorithm combines eigenmode initialization, geometry synthesis, and iterative refinement, which can be summarized as follows:

1. *Initialization of eigenmodes.* A simple circular geometry is used to generate an initial set of eigenmodes u_i using the MPB solver. The first few TM modes at the Γ point are extracted and processed to obtain their real-space field distributions. The p_1, p_2, d_1, and d_2 modes are used as the reference set for optimization.

2. *Initial geometry estimation.* The first geometry guess is constructed according to Eq. (5.5). The α_n weights can be tuned to modify the relative emphasis on p or d-like contributions.

3. *Iterative optimization.* The geometry is represented as a binary matrix corresponding to one quadrant of the unit cell. At each iteration, one pixel is flipped, and the geometry is symmetrized under C_4 rotational symmetry. The new configuration is scored using Eq. (5.3), and the pixel flip that provides the largest increase in S is accepted. The process continues until no further improvement occurs or a maximum iteration count is reached.

4. *Symmetry enforcement and export.* The optimized quadrant is symmetrically tiled to form the full C_4-symmetric unit cell. The final $\varepsilon(\mathbf{r})$ map is saved in HDF5 format and reimported into MPB for verification.

5. *Validation.* The generated geometry is validated by computing the band structure and checking whether the eigenmode ordering at the Γ point exhibits the desired p–d inversion.

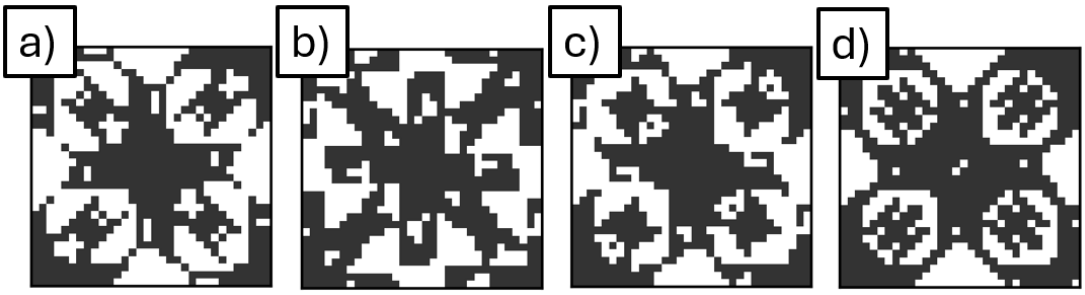


Figure 5.21 Four independent optimization runs of the same target configuration. Panels a)–d) show different but related dielectric patterns, illustrating that the algorithm is not fully stable and converges to distinct local optima. The white regions correspond to air, while the dark gray areas represent the high-permittivity material.

5.4.3 Results and limitations

Despite multiple optimization attempts and variations of the weighting parameters α_n, the algorithm did not yield a geometry where both d modes were below the p modes. Moreover, the search process proved to be unstable: repeated runs of the same scenario produced slightly different binary geometries. This instability suggests that the search often converges to different local optima, depending on early pixel choices during the optimization.

This generative approach represents a conceptually inverse design method where the geometry is derived from the modal properties rather than the other way around. While the algorithm did not achieve the targeted d-below-p ordering and shows limited stability between runs, it captures the essential physical idea that the dielectric distribution should reinforce the desired field structure.

We believe this concept is promising and could serve as a foundation for further research, where more advanced optimization strategies, such as gradient-based or machine learning methods, may be applied to improve stability and scalability. However, due to time constraints, this approach is not pursued further in this thesis.

6 Topological modes characterization

In the previous chapter, we discussed strategies for designing the photonic crystal unit cell to achieve photonic band-symmetry inversion. We introduced a design that utilizes the field-material overlap to lower the energy of a specific mode, and we applied this strategy to form our first topologically protected bands. In this chapter, we build on these ideas and further investigate the "bridged ring" design (see Fig. 5.12). The goal of this chapter is to analyze the properties of the topological modes that arise from our design and to demonstrate which properties to look for, how to characterize them, and how they affect potential applications.

We recall the geometry of the "bridged rings" design in figure 6.1a. The name originates from the original ring structure with cylinders near the sides that "bridge" to the neighboring cells, allowing the $d_{x^2-y^2}$ field lobes to sit on these bridges. This configuration reduces the energy required to sustain this mode, shifting it to a lower energy. In figure 6.1b, we show one possible combination of geometrical parameters that lead to the seed state [111, 112] of the topological modes.

The seed state in this case is defined as a combination of geometrical parameters that result in a structure with a closed photonic band-gap. By tuning these parameters, the band-gap can be reopened in either a topologically trivial or non-trivial way. Such states effectively represent the boundary between the trivial and inverted configurations discussed in the previous chapter and shown in figure 5.14.

In the previous chapter, figure 5.15 introduced the first combination of geometrical parameters leading to topologically protected edge modes, displayed in figure 5.16. The choice of these parameters was based on maximizing the degree of inversion in the phase diagram from figure 5.14 to select the inverted unit cell and then matching this inverted unit cell with a non-inverted one that produces the largest band-gap overlap. The resulting parameters were $[r_1 = 0.025 \cdot a,\ r_2 = 0.325 \cdot a,\ r_3 = 0.06 \cdot a]$ for the regular structure and $[r_1 = 0.425 \cdot a,\ r_2 = 0.45 \cdot a,\ r_3 = 0.12 \cdot a]$ for the inverted structure. In this case, the ring in the inverted structure is extremely thin, which raises the question of whether it is truly necessary, as omitting the ring and keeping only the side cylinders would simplify both the design and fabrication.

Introducing this additional requirement of having no ring in the search for a compatible design pair within our configuration space, we obtain the combination of geometries shown in figure 6.2. In this case, the geometrical parameters are $[r_1 = 0.1 \cdot a,\ r_2 = 0.275 \cdot a,\ r_3 = 0.06 \cdot a]$ for the regular structure and $[r_1 = 0.5 \cdot a,\ r_2 = 0.5 \cdot a,\ r_3 = 0.14 \cdot a]$ for the inverted structure. In the inverted structure, having $r_1 = r_2$ means that the thickness of the ring is zero and thus no ring is present. We still need to include these parameters, as r_2 determines the distance of the side cylinders from the center. In this case, $r_2 = 0.5 \cdot a$ means that the side cylinders are placed exactly at the center of the unit cell's sides, which also corresponds to the centers of the $d_{x^2-y^2}$ field lobes.

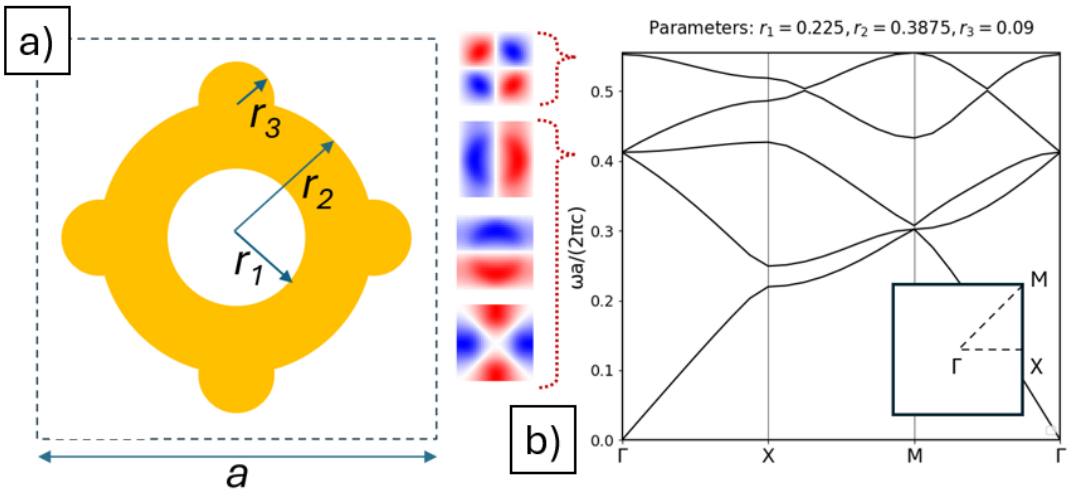


Figure 6.1 **a)** definition of geometrical parameters of the bridged ring design. **b)** Example of a seed state which can lead to a topologically trivial or non-trivial case, depending on the way of tuning the geometrical parameters.

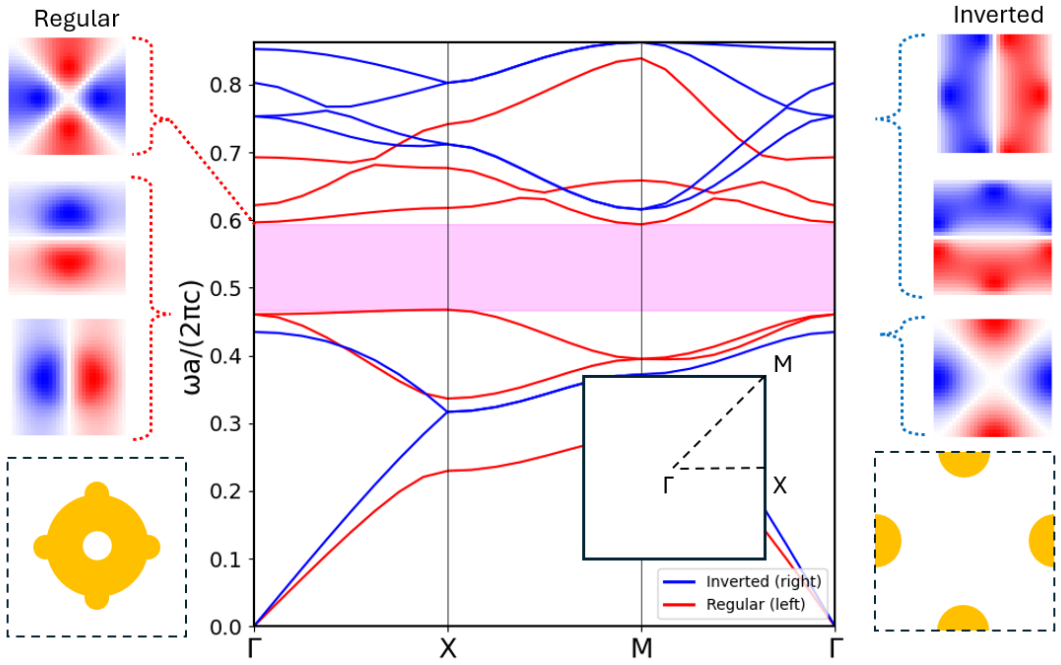


Figure 6.2 Band structure of the design exhibiting the highest degree of band-symmetry inversion and its complementary design, which yields the largest band gap overlap with restriction $r_1 = r_2$ for the inverted structure. The pattern corresponds to the bridged ring design defined in 6.1. Regular structure parameters: $[r_1 = 0.1 \cdot a,\ r_2 = 0.275 \cdot a,\ r_3 = 0.06 \cdot a]$; inverted structure parameters: $[r_1 = 0.5 \cdot a,\ r_2 = 0.5 \cdot a,\ r_3 = 0.14 \cdot a]$. The material used is $\mathrm{InP}_{1550\ \mathrm{nm}}$.

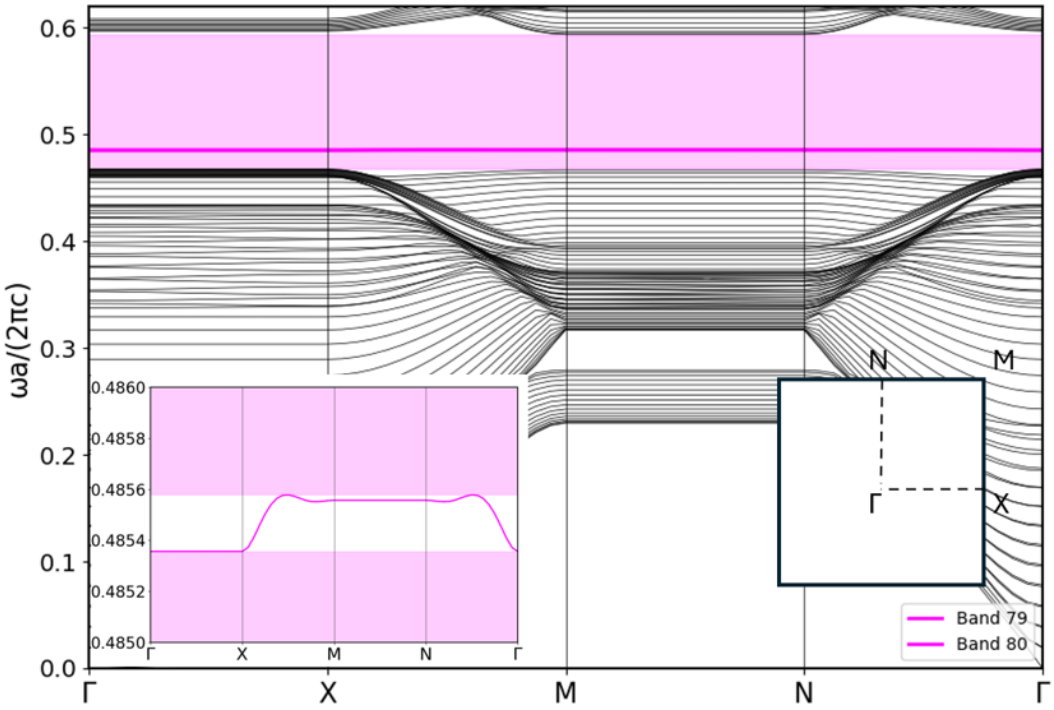


Figure 6.3 Band structure of a topological interface composed of 16 unit cells of each type defined in Figure 6.2 The two nearly degenerate topological modes are highlighted in magenta, while the original bad-gap is depicted in pink. The mode dispersion detail reveals abnormal dispersion slope.

The topological modes produced by this geometrical configuration are extremely flat. The detail of the topological mode dispersion in figure 6.3 reveals that the dispersion slope is anomalous, leading to a negative group velocity [113]. In this configuration, transmission simulations cannot be provided, as the topological bands act as light-trapping defects, making them unsuitable for the goals of this thesis.

However, these light-trapping, topologically protected modes offer interesting perspectives in several research areas. First, they enhance light-matter interaction, which can lead to improved sensing and field localization [114, 115]. They can also produce slow light and compact delay lines [116, 117], and there is potential for nonreciprocal and magnetic-free isolators [118, 119].

We suspect that the flatness of the bands is correlated with the degree of inversion or the width of the photonic band-gap. We will discuss this topic in more detail in section 6.4. For now, since we are interested in the transmission properties, we will select a different viable combination of geometrical parameters that lead to a topologically non-trivial interface with a smaller band-gap overlap. The parameters chosen for this case are $[r_1 = 0.105 \cdot a,\ r_2 = 0.35 \cdot a,\ r_3 = 0.072 \cdot a]$ for the regular structure and $[r_1 = 0.345 \cdot a,\ r_2 = 0.425 \cdot a,\ r_3 = 0.108 \cdot a]$ for the inverted structure. The band structures of the individual photonic crystals, as well as their common band gap, are shown in figure 6.4.

The topological modes produced by this geometry exhibit significantly larger dispersion (fig. 6.5a). In this case, the dispersion is normal, and in figure 6.5b we show the transmission calculated using the Lumerical FDTD solver discussed

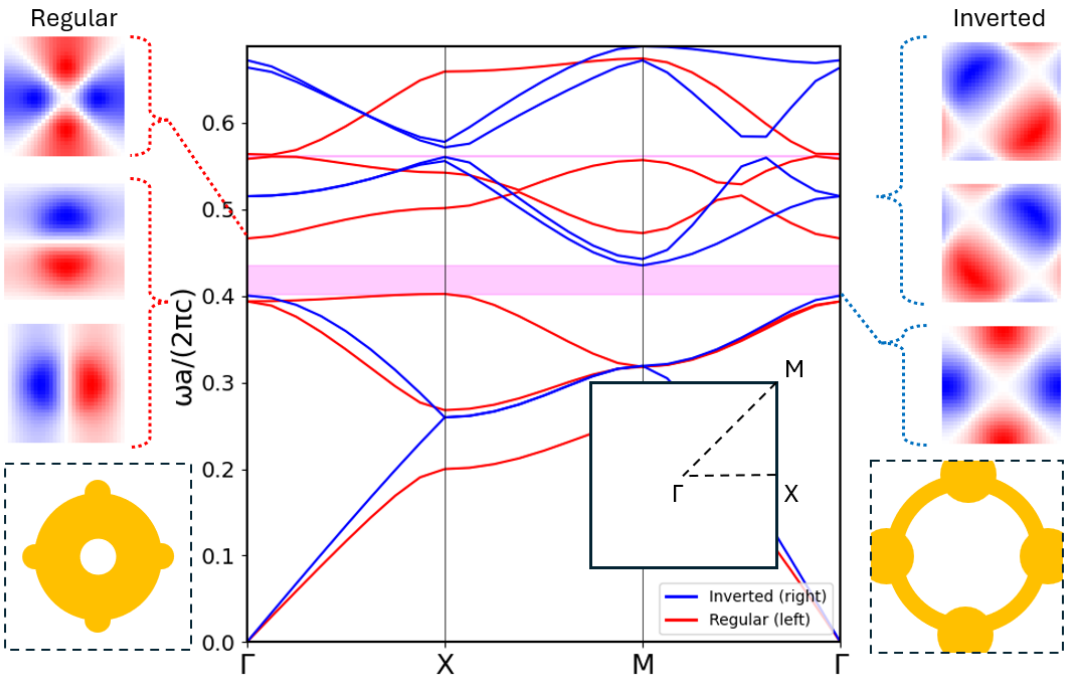


Figure 6.4 Band structure of the design that produces topologically non-trivial interface, but produces narrower band-gap then the design in figure 6.2. The pattern corresponds to the bridged ring design defined in 6.1. Regular structure parameters: $[r_1 = 0.105 \cdot a,\ r_2 = 0.35 \cdot a,\ r_3 = 0.072 \cdot a]$; inverted structure parameters: $[r_1 = 0.345 \cdot a,\ r_2 = 0.425 \cdot a,\ r_3 = 0.108 \cdot a]$. The material used is $\mathrm{InP}_{1550\ \mathrm{nm}}$.

in section 2.2.2. The transmission is plotted to share the y-axis with the band structure, which corresponds to wavelength. Notice that there is a slight shift in the position of the observed features along the y-axis. This is because MPB is solved using a dispersionless approximation of the material, while in FDTD simulations the material dispersion is included.

The mode transmission behaves exactly as expected: in the dispersive region, the transmission is nearly 100%, while in the gapped regions it sharply drops to zero, or in this case, to the level of numerical noise produced by the deconvolution discussed in section 2.2.2.

6.1 Classifying the type of topological modes

Before we proceed to characterize the topological mode properties, we need to classify the type of topology. To do this, we use the Wilson loops introduced in equation 1.21. The topological modes shown in figure 6.5, produced by the individual PCs from figure 6.4, are located in the photonic band gap and arise from eigenmode order inversion. To characterize the nature of their topological origin, we examine the Wilson spectra of the set of bands directly below the photonic band gap, where the $d_{x^2-y^2}$ mode was intentionally lowered in energy in the inverted case.

In both the topologically trivial and non-trivial cases, we need to consider two bands in the Wilson analysis. In the trivial case, we analyze bands 1 and 2 (indexing from zero), as they are degenerate between $M - \Gamma$. For the inverted

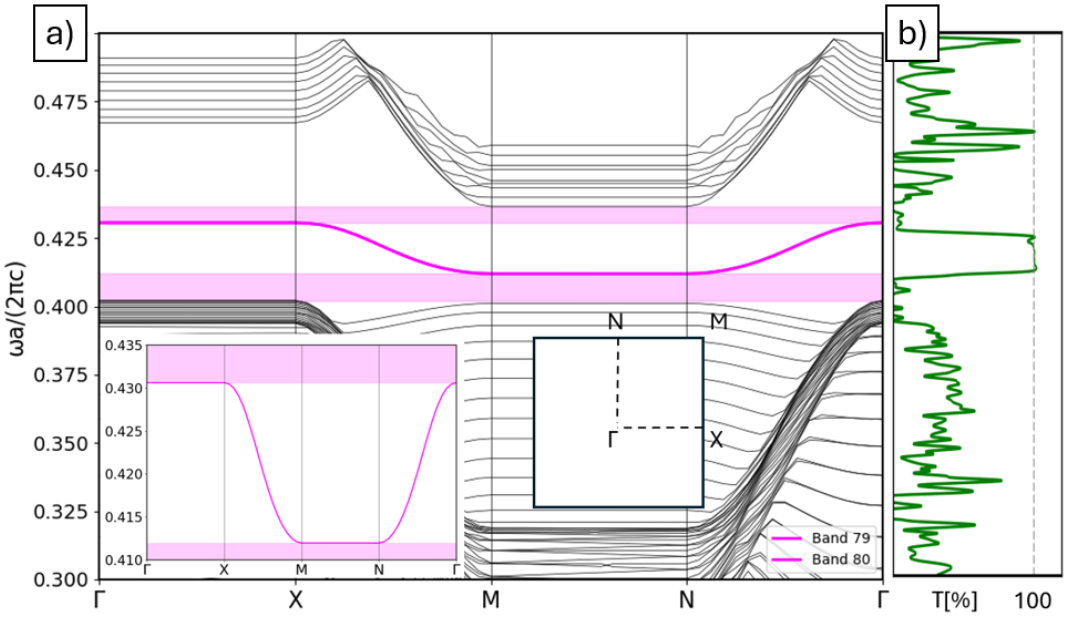


Figure 6.5 **a)** Band structure of a topological interface composed of 16 unit cells of each type defined in Figure 6.4 The two nearly degenerate topological modes are highlighted in magenta, while the original bad-gap is depicted in pink. The mode dispersion detail reveals regular dispersion slope. **b)** Transmission of the interface calculated by the FDTD method.

case, we consider bands 0 and 1, since they are degenerate between $X - M$. Thus, in this scenario, we use the matrix overlap formula (eq. 1.20).

The resulting Wilson spectra are shown in figure 6.6. These spectra reveal the positions of the Wannier centers in reciprocal space. We can see that there is no movement in either case, as the Wilson bands are flat in both the trivial (fig. 6.6a) and non-trivial (fig. 6.6b) cases. However, case (b) shows that the Wannier centers are displaced toward the edge of the Brillouin zone, creating a polarization mismatch between the two PC designs at the interface.

To demonstrate that this is indeed the origin of the topological modes in our study and not merely an effect of the interface itself, we present three different scenarios in figure 6.7. In column a), two photonic crystal designs belonging to the same topologically trivial phase (see fig. 5.14) are paired. In column b), a trivial design is paired with a topological one, and in column c), two unit-cell designs belonging to nontrivial topological designs are paired. The type of topology in each case corresponds to that shown in the Wilson loop analysis of the left and right photonic crystals, respectively.

The first row shows the resulting band structure of the whole system. We can see that only the combination of topological and trivial PC designs produces compensation modes. This confirms that the modes do not originate merely from the presence of an interface, since an interface exists in all three cases, but specifically from the junction between topologically trivial and non-trivial designs.

In summary, we have demonstrated that the "bridged ring" design provides a flexible platform for engineering topological photonic modes through precise tuning of geometrical parameters. By analyzing several representative configurations,

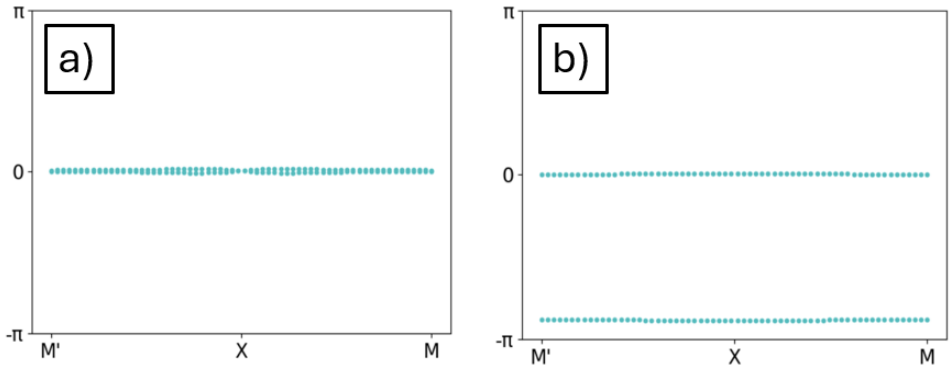


Figure 6.6 Wilson spectra of the set of bands below the photonic band gap of the PC design introduced in figure 6.4. The flat but displaced bands indicate the obstructed atomic limit topological effect.

we showed that the presence or absence of the ring, and the resulting degree of band-symmetry inversion, strongly influence the properties of the topological interface, ranging from flat, localized modes to highly transmissive dispersive states. We also confirmed that the origin of these topological modes lies in the obstructed atomic limit. These findings establish a foundation for the following sections, where we will further characterize the behavior of these modes in terms of spatial localization, directionality, and their relation to the underlying band-gap structure.

6.2 Edge modes vs boundary size

Another property we investigate is the behavior of the topological interface as the number of photonic crystal unit cells surrounding the topological boundary is varied. So far, we have worked in the limit where the number of unit cells on each side of the interface, N, is large, such that each crystal behaves as semi-infinite. To investigate the effect of boundary finite size effects, we have used in our simulations finite values for the number N of unit cells defining the boundary, with N varying between sixteen and twenty.

Since we are using MPB, it is important to recall that our approach cannot account for truly semi-infinite photonic crystals. Instead, we rely on supercells, as demonstrated in figure 2.7. This limitation provides a convenient way to study the effect of the number of cells around the interface, since N directly defines the size of the supercell.

The first property we focus on is the localization of modes around the interface as N increases. To study this, we calculate the eigenmode corresponding to one of the two topological bands produced by the transmission-capable interface discussed in figure 6.5. Unlike the eigenmodes used in the band-connection procedure or the band inversion search, these eigenvectors correspond to the entire supercell. Moreover, since we are interested in a propagating wave, we do not calculate the eigenmode at Γ but rather at a k-point located midway between Γ and N, corresponding to the highest propagation.

Finally, we modified the supercell arrangement to include both interfaces

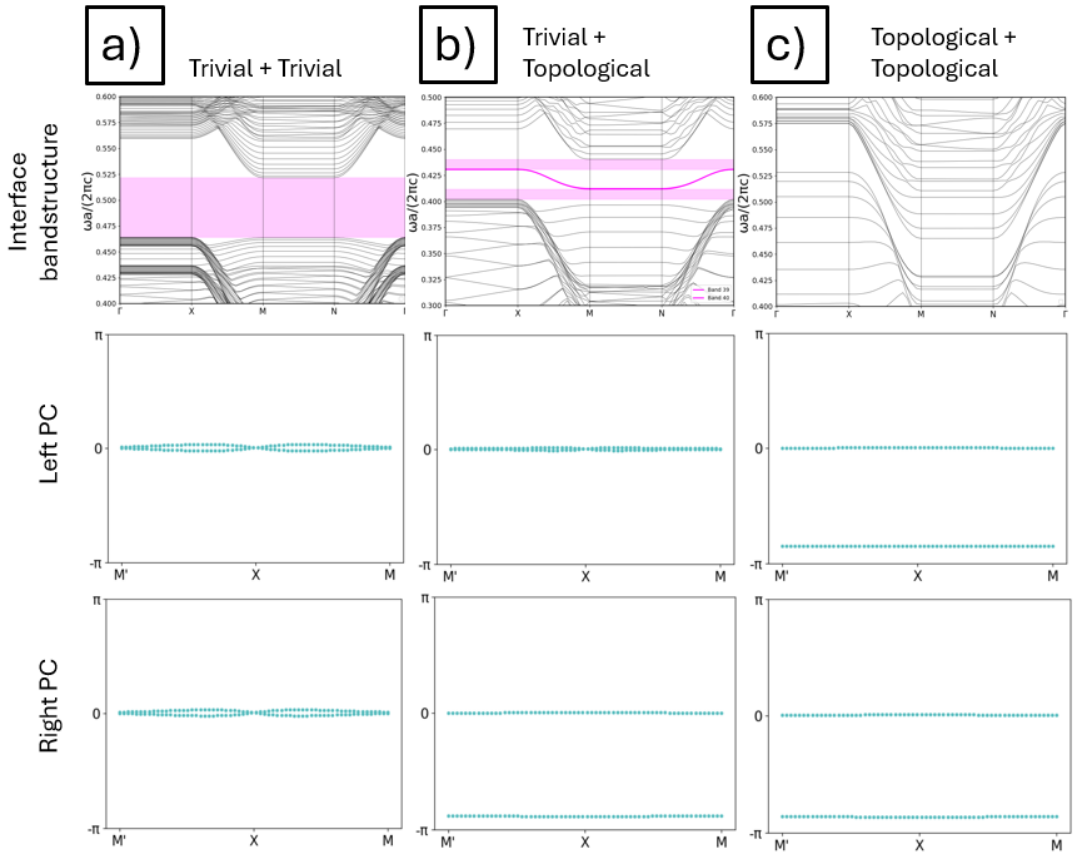


Figure 6.7 Interface modes and Wilson loop analysis for three photonic crystal combinations. Each column corresponds to an interface formed by joining two photonic crystals with distinct unit cell parameters, denoted as Left PC and Right PC. Top row: Interface band structures computed using a supercell geometry. Gap-localized modes are observed only in case b). Middle and bottom rows: Wilson loop spectra for the left and right photonic crystals forming each interface, respectively, calculated for the photonic bands below the band gap. Case a) shows an interface between two trivial configurations with matching Wilson loops and no interface modes. Case b) corresponds to a mismatch between a trivial and an obstructed atomic limit phase, indicated by a shift in the Wilson loop; this results in a pair of interface-localized modes within the band gap. Case c) involves two OAL phases with identical Wannier center positions and therefore no protected interface modes. This analysis demonstrates that the presence of localized interface states originates from a polarization mismatch between the adjoining bulk phases.

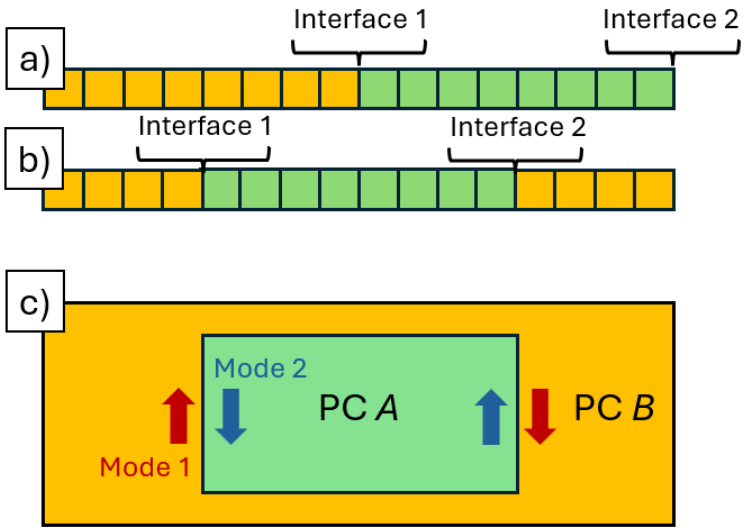


Figure 6.8 Schematic representation of supercell configurations used to simulate topological interfaces. **a)** An original supercell arrangement with one interface placed at the center and a second appearing at the boundary due to periodicity. **b)** Modified supercell with both interfaces symmetrically located within the cell, allowing for clearer analysis of interface-localized modes. **c)** Enclosed configuration where photonic crystal A is embedded in PC B, showing how the same topological mode (Mode 1) propagates in opposite directions depending on the orientation of the interface.

within its region, as shown in figure 6.8b, instead of the original configuration with one interface at the center and one at the edge (see figure 6.8a). Each supercell inherently produces two types of interfaces due to its periodic repetition, and the interface orientation determines the propagation direction. Suppose we create an enclosed PC A within PC B, as depicted in figure 6.8c. In this configuration, both interfaces are connected, and it becomes clear that one mode, in our case, the mode labeled "Mode 1", is responsible for upward propagation along the interface when PC B is on the left and PC A on the right. When the sides are reversed at interface 2, Mode 1 becomes responsible for downward propagation.

When calculating the field of the supercell from figure 6.8b, we select a k-vector and the corresponding band to display. In our case, the chosen k-vector corresponds to upward propagation. Modes 1 and 2 each belong to a different band, which means that to observe a topological mode, the field must be concentrated around one of the two interfaces. If field lobes were present near both interfaces, it would indicate that both interfaces allow propagation in the same direction within a single mode, which is not characteristic of topologically protected unidirectional modes.

We investigate this property by varying the number of PC unit cells N between two topological interfaces and observing where the corresponding topological mode localizes. The goal is to determine how many unit cells are required for the mode to become fully confined to a single interface. The results are summarized in figure 6.9, which presents data for two distinct topological modes.

Figure 6.9**a** shows the spatial distribution of the *first topological mode*, where each curve corresponds to a different value of N ranging from 1 to 10, color-coded accordingly. The vertical axis represents the mode magnitude summed over the

transverse (y) direction, while the horizontal axis indicates the position between the two interfaces. Although all profiles are plotted along the same horizontal axis, the actual physical distance between the interfaces increases with N. Thus, the x-axis does not represent an absolute length scale but rather a relative coordinate system aligned for visual comparison. The key purpose of this plot is not to assess the spatial width of the mode, but to illustrate how its localization center shifts as the separation between interfaces increases. We observe that for small N, the mode is distributed across both interfaces, but as N increases, it becomes progressively localized at one interface, indicating a transition to a unidirectional regime.

Figures 6.9**b** and **c** show the field distributions of the *second topological mode* for $N = 6$ and $N = 14$, respectively. For $N = 6$, the field amplitude remains significant at both interfaces, showing that the mode is delocalized and lacks a preferred propagation direction. In contrast, when $N = 14$, the mode becomes fully confined to Interface 2, demonstrating the emergence of directional transport consistent with topological protection. These examples, presented side by side, emphasize that different topological modes can localize on different interfaces, and that sufficiently large separation N allows the modes to "choose" their respective interfaces without overlap. This highlights the robustness and interface selectivity of topological states in photonic crystals.

The dependence on the number of cells in the supercell can be better understood by dividing the shifted supercell defined in figure 6.8b into two regions: the first half of the x-axis, centered around interface 1, and the second half, centered around interface 2. Summing the field intensity within these regions corresponds to the total energy propagating in each direction. This situation is illustrated in figure 6.10, where the blue dots, labeled as forward propagation, represent the percentage of the field located in the first region (containing interface 1) for the first topological mode. The red dots, labeled as backward propagation, represent the percentage of the field in the region around the second interface for the same mode. For the second topological mode, the situation is reversed.

The field distribution remains non-preferential up to $N = 3$, after which the separation between the two propagation directions becomes evident. Saturation occurs around $N = 10$. For this particular design (the one defined in figure 6.4), 98.5% of the energy propagates in one direction at $N = 9$, 99.7% at $N = 10$, and 99.99% at $N = 12$.

Another property we analyzed is the width of the topological modes. After separating the field into two regions around the interfaces, we calculated the standard deviation of the field in each region based on the data shown in figure 6.9a, and the results are presented in figure 6.11. A local minimum in the mode width is observed, after which the width increases, and around $N = 9$, the mode begins to narrow again. The value $N = 9$ also corresponds to the point where mode unidirectionality starts to saturate. The mode width appears to continue decreasing beyond the range of our dataset.

We did not calculate the exact value of N required to reach width saturation, as it appears to be large and, from an application perspective, smaller N values are preferable for higher integration density. Since $N = 10$–12 is sufficient to achieve unidirectionality, the mode width becomes less important. The only potential application where it might play a role is in field–matter interaction,

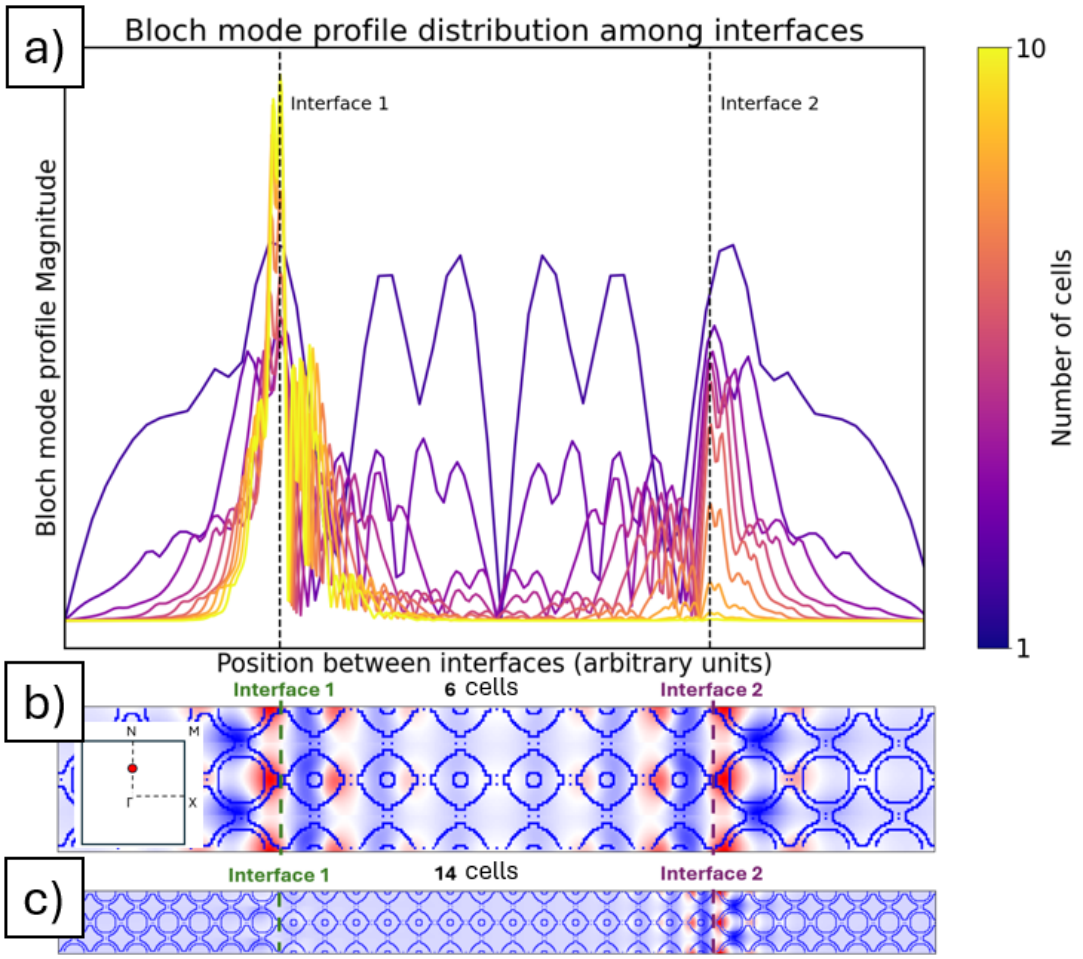


Figure 6.9 Dependence of mode localization on the number of photonic crystal unit cells between topological interfaces.
a) *First topological mode*: Bloch mode profile magnitude (summed over the transverse direction) plotted along the position between two interfaces for various numbers of unit cells N, color-coded from 1 to 10. As N increases, the mode transitions from being spread over both interfaces to being localized predominantly around one.
b,c) *Second topological mode*: Field distribution for **(b)** $N = 6$, showing the mode extends over both interfaces, indicating lack of unidirectionality, and **(c)** $N = 14$, where the mode is fully localized at Interface 2, demonstrating unidirectional propagation consistent with a topologically protected state.

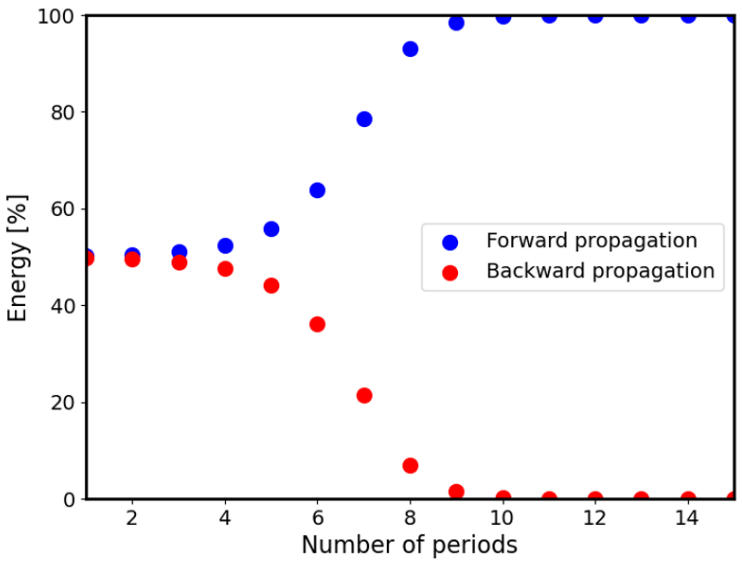


Figure 6.10 Directionality of the first topological mode as a function of the number of unit cells N between two interfaces. The supercell (defined in Fig.6.8b) is divided into two spatial regions: one containing Interface 1 (first half of the x-axis) and the other containing Interface 2 (second half of the x-axis). The blue points indicate the fraction of the total field energy located around Interface 1, corresponding to forward propagation, while the red points indicate the energy near Interface 2, corresponding to backward propagation. The design is based on the one shown in Fig.6.4.

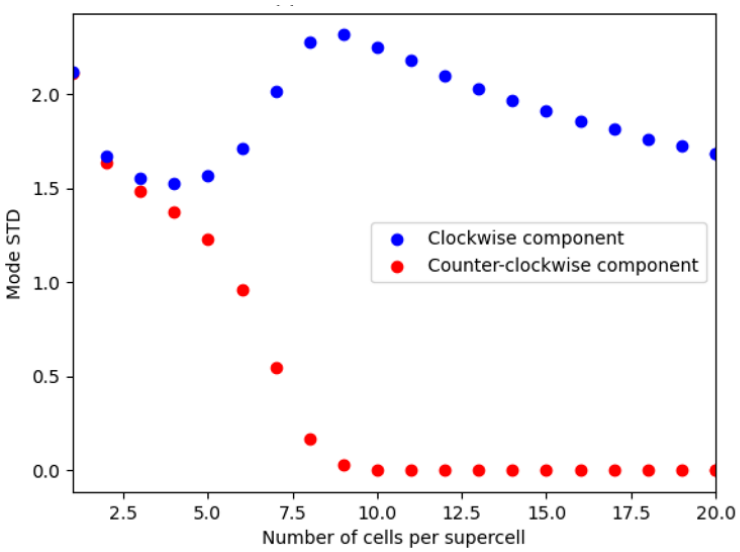


Figure 6.11 Standard deviation (STD) of the field distribution for the first topological mode in the upper band channel as a function of the number of unit cells N. Clockwise (blue) and counter-clockwise (red) components correspond to regions around Interfaces 1 and 2, respectively.

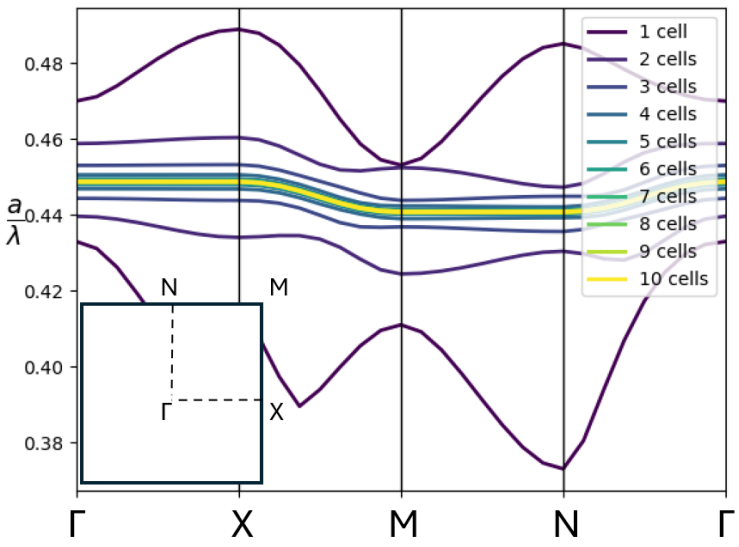


Figure 6.12 Band structure evolution for different numbers of unit cells N in the supercell, showing the convergence of the topological modes in the upper band channel. As N increases from 1 to 10, the initially split topological bands gradually merge and become nearly degenerate around $N = 6$, indicating stabilization of the mode frequency.

where tighter field confinement could enhance detection capabilities. However, we believe there are more effective approaches to achieve such improvement, including the slow-light interfaces mentioned earlier.

The final property we investigated is the position of the topological modes along the energy axis as the number of cells changes. Figure 6.12 shows that the topological modes tend to converge toward a specific energy level and become degenerate as N increases. Degeneracy is achieved at around $N = 6$, indicating that the value of N required to achieve unidirectionality is also sufficient to ensure a stable band position.

In this section, we investigated how the number of photonic crystal unit cells N surrounding a topological interface affects the behavior of topological modes. Our results show that for the studied design, the critical threshold for achieving unidirectionality occurs around $N = 9$–10, beyond which the mode localizes to a single interface with over 99% directionality. Importantly, this same range of N also ensures spectral stability, as the mode energies converge and become degenerate around $N = 6$. Although the spatial width of the mode continues to evolve and does not saturate within the tested range, this parameter is less critical for most topological photonic applications. Therefore, the main consideration for practical implementation is the number of unit cells required to guarantee unidirectional transport, which in this case also provides mode frequency stabilization. This balance makes moderate values of N an optimal choice for integration into compact photonic devices.

6.3 Defect states

As mentioned in the introduction, the property that makes topological modes unique is their resistance to defects. Since topological modes originate from the bulk properties of the two crystals rather than from the interface itself, the interface should play little to no role in their propagation.

One way to disturb topological modes would be to introduce additional modes in the same energy region, allowing scattering. This is mitigated by designing the topological modes within a photonic band gap in both complementary PCs. One could argue that within the band gap, additional surface modes could arise due to the local breaking of symmetry at the interface between the two geometrically different PCs. However, this is not the case, as shown in figure 5.17, where two inverted designs are matched and no modes appear within the band gap, which remains fully open. We present this scenario to illustrate that although the true gap was closed in figure 6.7, it was not due to the creation of topological modes, but because the selected geometrical parameters led to a narrow overlap of the photonic band gaps in the first place.

Next, we investigate the design under perturbation. To do this, we use FDTD simulations, where we construct a large interface and employ a technique in which we import the source of the topological modes from an additional simulation based on the specific unit cell geometries used in the interface, as discussed in section 2.2.2.

The first set of simulations examines whether the modes behave symmetrically when facing a disturbance on the left or right side of the interface. We created large-scale interfaces of 40×40 cells to study left and right turns, and smaller 25×20-cell interfaces to investigate perturbations created by switching cells next to the interface with their complementary counterparts. The geometry and the resulting field profiles are shown in figure 6.13.

Even from the field profiles, there is a slight asymmetry between the left and right side perturbations. Defects placed on the right side do not seem to affect the topological modes significantly, while defects on the left side cause the mode to almost vanish. The transmission values are shown in figure 6.14, where we also include the transmission of the undisturbed interface to provide a reference for the oscillation scale. The reason the values exceed 100% is explained in section 2.2.2, so we focus on the transmission value around which the data oscillate. The figure shows that the right defect (panel d) produces nearly the same transmission as the defect-free interface, and the right turn (panel c) slightly increases the oscillation, but the average transmission remains unchanged. The left turn (panel a) and the left defect (panel b), however, significantly disturb the mode.

The defects used in the simulations are, however, extremely severe, as replacing some unit cells with a completely different topology is not a realistic fabrication defect one could expect. To better model the effect of fabrication imperfections, we investigate how the shape, size, and position of the defect affect the interface. The results of eight different defect simulations are shown in figure 6.15.

We observe that defects placed at the center of the interface do not affect the modes enough to distinguish the transmission behavior from that of the undisturbed interface. Interestingly, the small defect on the right side of the interface (green square) has a stronger effect on the modes than the small defect

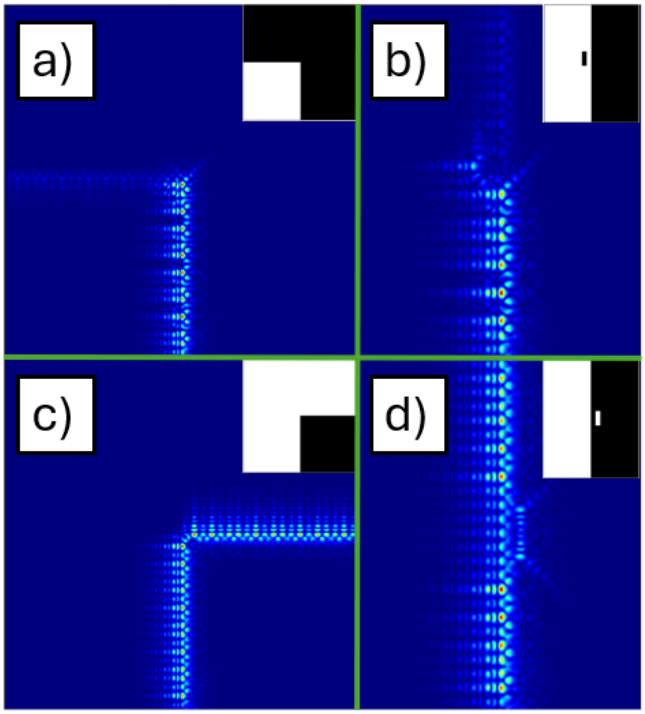


Figure 6.13 Large-scale interface perturbation simulations. Each panel shows the E_z field profile obtained from FDTD simulations, illustrating mode propagation along the perturbed interface using the color scale. The black–white inset in the upper right corner of each panel represents the unit cell distribution, where white indicates topologically trivial cells and black indicates topologically non-trivial (inverted) ones. The defect interfaces consist of 20×25 unit cells, while the turn interfaces consist of 40×40 unit cells. The unit cell design used here is the one introduced in Fig. 6.4. Panels (a–d) test different interface configurations, including 90° turns to the left and right, as well as replacements of three cells one cell away from the interface with the opposite topological type.

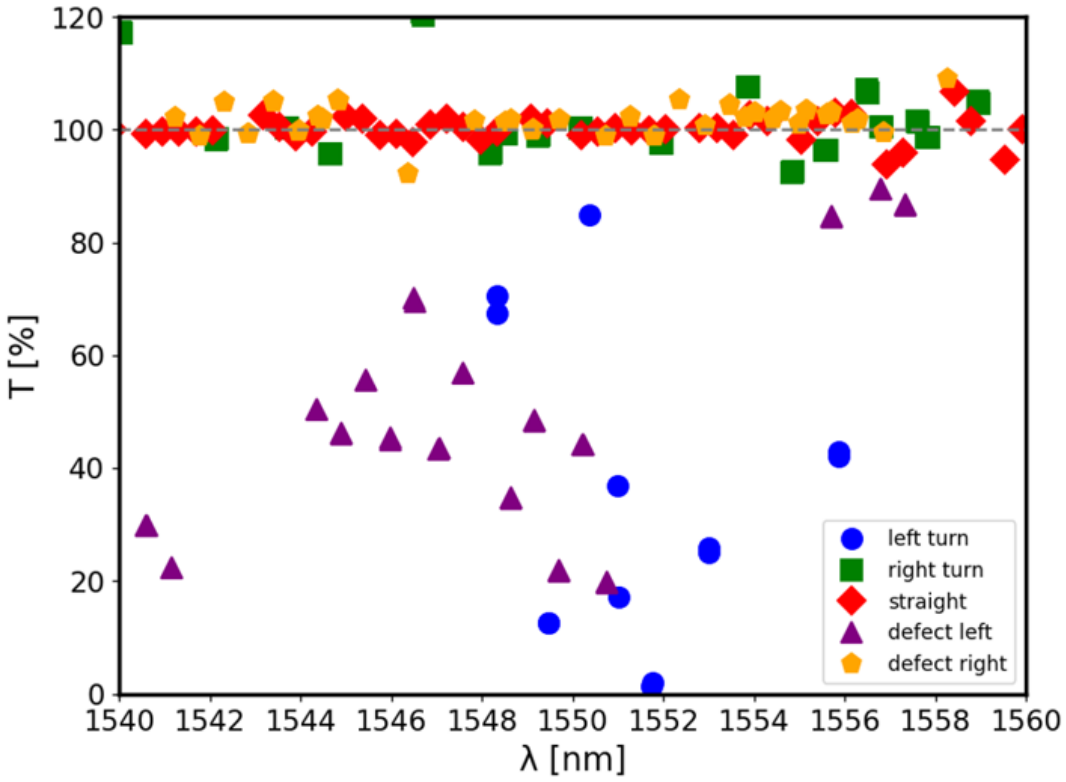


Figure 6.14 Transmission spectra of the geometries shown in Fig. 6.13, including the straight undisturbed interface for reference. The results are qualitative rather than quantitative, as discussed in Sec. 2.2.2, which explains why some values exceed 100%. The relevant information is the transmission level around which the data oscillate.

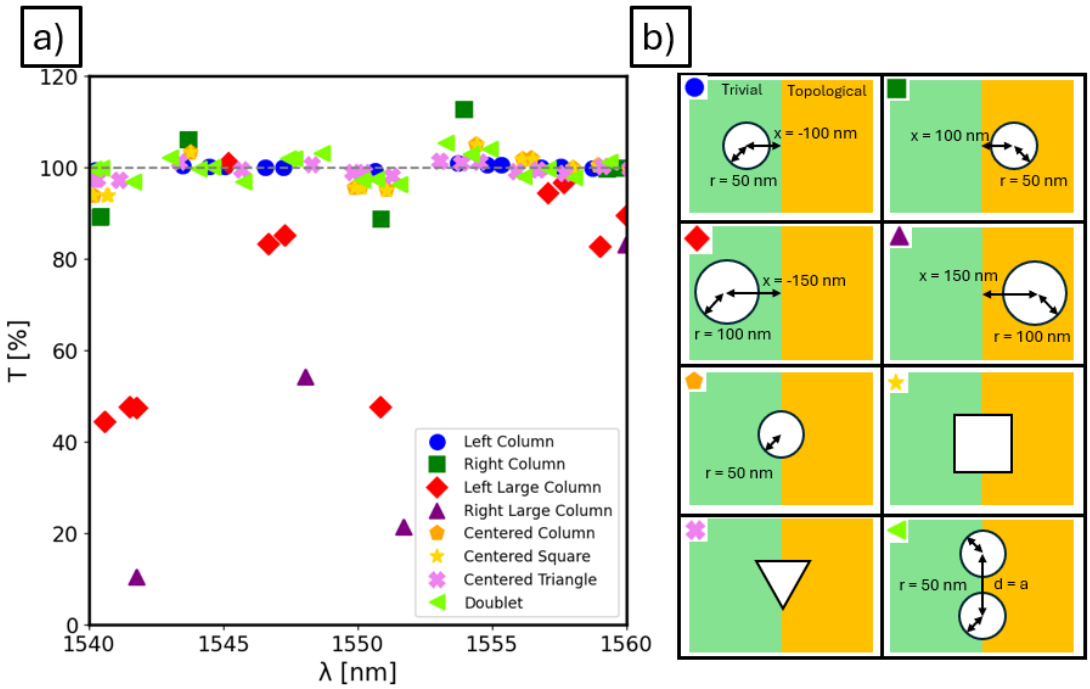


Figure 6.15 A set of defect configurations placed relative to the center of the interface. Panel (a) shows the resulting transmission spectra, which exhibit the same qualitative behavior as in the previous figure. Panel (b) illustrates the corresponding defect geometries. The designs of the trivial and topological unit cells are identical to those introduced in Fig. 6.4 and Fig. 6.13. The defects are made of the same material as the surrounding photonic crystal.

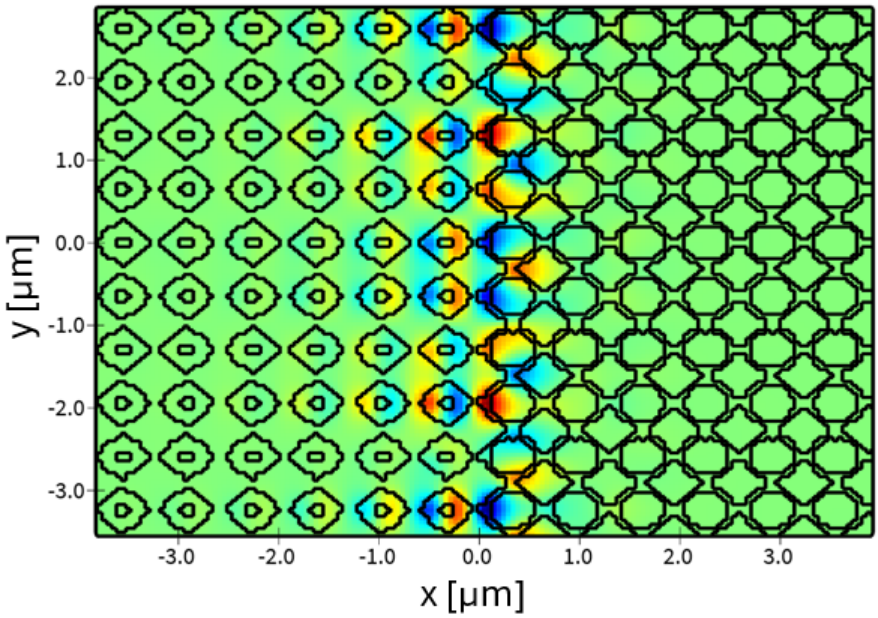


Figure 6.16 E_z field profile obtained from FDTD simulation at a wavelength of 1550 nm, showing the mode propagation along the topological interface. The interface separates the topologically trivial (left) and non-trivial (right) photonic crystal regions.

on the left side (blue circle). Increasing the size of these defects (red diamond and purple triangle) further amplifies the effect: the defect on the right side of the interface has a stronger influence on mode transmission. This observation disagrees with the result shown in figure 6.14.

To provide an explanation, we examine the near-field mode distribution within the interface shown in figure 6.16. The field is distributed asymmetrically between the two sides of the interface. The lobes of the mode on the right side have significantly higher amplitudes, but the right tails of the mode do not extend as far as the left tails, which have smaller amplitudes. We therefore suspect that the modes are more affected by nearby distortions on the right side, as shown in figure 6.15, while defects located one lattice parameter away on the right side are too distant to influence the modes in our configuration, explaining why the modes in figure 6.13 remain unaffected. On the other hand, the left side has longer tails that are influenced even by distant defects, as seen in figure 6.13, but the lower amplitude of the lobes makes them less sensitive to nearby defects, as observed in figure 6.15. We also suspect that tail interference is responsible for the turns being significantly more efficient to the right side than to the left, since there is essentially no tail overlap in the right turn (figure 6.13c).

Unfortunately, this analysis shows that this particular design is not suitable for integrated circuit applications, where inefficient turns become a limiting factor. It is possible that a different combination of geometrical parameters of the PC unit cells could affect the mode's defect sensitivity. However, these modes still exhibit greater robustness than a conventional waveguide and provide a promising platform for slow-light applications due to the tunable dispersion of the topological mode, as demonstrated in the following section.

6.4 Band-gap vs mode dispersion

In the previous chapter, particularly in figure 5.14, we established that using a single unit cell design (in this case the one introduced in figure 5.12), we have the freedom to choose any combination of trivial and topological geometries as long as they produce a sufficient band-gap overlap. In this chapter, we have already mentioned two such combinations: one that resulted in a large photonic band gap with very small dispersion (figure 6.2) and another with a smaller band gap but significantly larger dispersion (figure 6.4). We intentionally chose the parameters to reduce the band-gap overlap while aiming for higher dispersion. We now propose a more systematic way to characterize the relationship between the band-gap size and the dispersion.

The idea is as follows: selecting a trivial and a nontrivial geometry pair in the inversion diagram (figure 5.14) defines a line between these points. Along this line lie geometries that gradually transform from topological to trivial as the band gap reduces until it closes, where the p and d modes become degenerate, and then reopens, removing the eigenmode inversion. It is reasonable to expect that the endpoints of this line produce the largest band-gap overlap, while choosing pairs closer to the inversion closure will gradually reduce the resulting band-gap overlap. We describe this transition along the line by introducing a mixing coefficient $M \in [0, 1]$, which is used to calculate the geometry pairs based on the initial endpoints V_{max} and V_{min}:

$$\begin{aligned} V_1(M) &= MV_{max} + (1 - M)V_{min} \\ V_2(M) &= (1 - M)V_{max} + MV_{min} \end{aligned} \tag{6.1}$$

The scheme is demonstrated on figure 6.17.

To provide a concrete example, we set the values of the endpoints to $V_{min} = [0.425, 0.45, 0.12]$ and $V_{max} = [0.025, 0.325, 0.06]$, which correspond to the case of the highest band-gap inversion without any restriction and the largest band-gap overlap. The mixing values $M \in [0.75, 1]$ then define pairs with a band-gap overlap shown in figure 6.18. Note that the gap would close at $M = 0.5$, where both geometries become identical, corresponding to the case of p–d degeneracy. However, we must consider not the individual band gaps in each complementary PC, but rather their band-gap overlap, which may close earlier. We then plot the maximum dispersion slope along the topological mode for various values of M and compare it to the corresponding band-gap size.

However, recording the highest dispersion slope has its limitations. Examining the gradient of the topological bands for various values of M shows that the maximum can occur at different values of $\mathbf{k}$. Selecting a particular $\mathbf{k}$ value does not seem reasonable, so instead, we defined a different metric: the energy difference between the Γ and N points, since this is the region of interest for the dispersion.

Using this metric, we demonstrate three scenarios of the dispersion versus band-gap dependency. In figure 6.19a, we show the results from figure 6.18 using the new metric, which displays the same monotonic trend that does not reach zero. In panel b), we present a different set of initial points derived from the geometry selected for simplified fabrication, where the ring in the inverted design is omitted (see figure 6.2). In this case, it is possible to achieve almost perfectly flat bands,

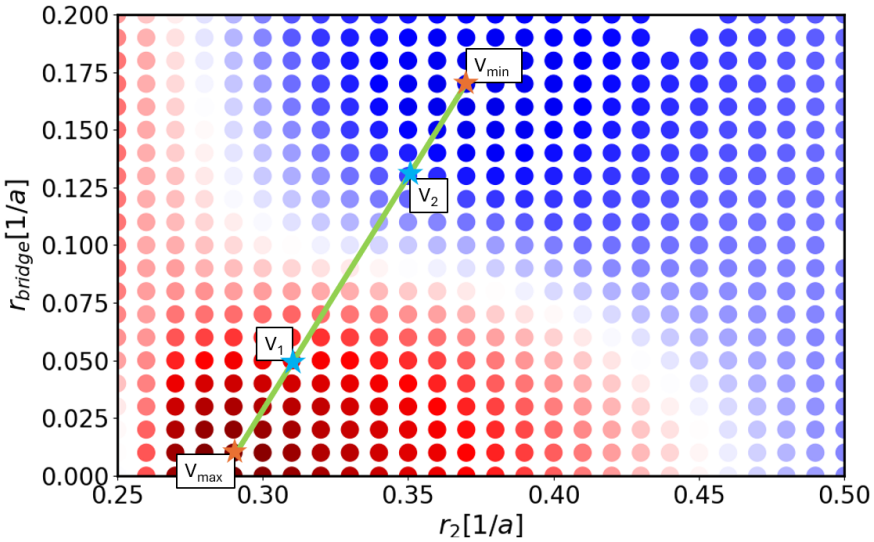


Figure 6.17 Illustration of the geometry interpolation scheme used to define a continuous path between the trivial and topological phases in the inversion diagram (Fig. 5.14). The line connecting V_{max} and V_{min} represents a gradual transformation from the topological to the trivial geometry through band-gap closure and reopening. The intermediate geometries V_1 and V_2 correspond to points along this line, parameterized by the mixing coefficient $M \in [0, 1]$, which determines their position between the two end points. The figure serves only as a conceptual demonstration and does not represent precise point placement.

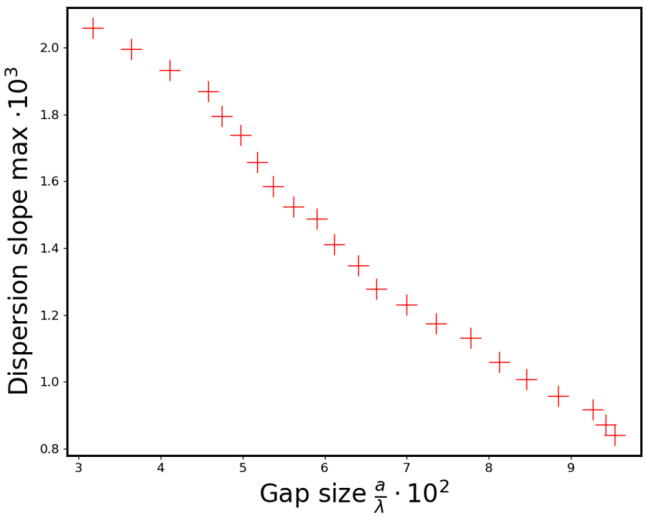


Figure 6.18 Dependence of the maximum dispersion slope of the topological edge mode on the size of the band-gap overlap for geometry pairs defined by the mixing coefficient $M \in [0.75, 1]$. The end points $V_{min} = [0.425, 0.45, 0.12]$ and $V_{max} = [0.025, 0.325, 0.06]$ correspond to the configurations with the highest band-gap inversion and the highest band-gap overlap. The observed trend shows a monotonic decrease of the dispersion slope with increasing band-gap size.

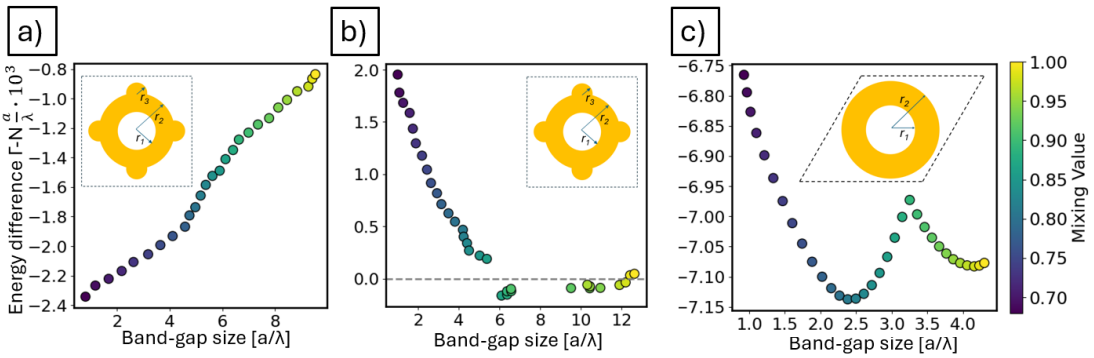


Figure 6.19 Dependence of the $\Gamma - N$ energy difference on band-gap size for several interface designs. The vertical axis shows the energy difference $\Delta E_{\Gamma\text{–}N} \equiv E(\Gamma) - E(N)$ of the relevant band (in normalized-frequency units). The horizontal axis is the band-gap size $[a/\lambda]$. Points are colored by the mixing value used to linearly interpolate between the inverted and regular unit cells (0.70–1.00); the horizontal dashed line denotes $\Delta E_{\Gamma\text{–}N} = 0$. All structures use indium phosphide [120]. **a)** Interface from Fig. 5.12: inverted ($r_1 = 0.425a,\ r_2 = 0.45a,\ r_3 = 0.12a$) vs. regular ($r_1 = 0.025a,\ r_2 = 0.325a,\ r_3 = 0.06a$); this pair yields the largest band-gap overlap. **b)** Fabrication-simplified variant with cylinders replacing rings: inverted ($r_1 = 0.5a,\ r_2 = 0.5a,\ r_3 = 0.14a$) vs. regular ($r_1 = 0.1a,\ r_2 = 0.275a,\ r_3 = 0.06a$). **c)** Interface derived from a hexagonal (C_6) lattice [51]: inverted ($r_1 = 0.38a,\ r_2 = 0.45a$) vs. regular ($r_1 = 0.27a,\ r_2 = 0.36a$)

as the energy difference reaches zero, consistent with the design shown in figure 6.2. The trend remains monotonic until zero dispersion is reached. Finally, in panel c), we demonstrate that the trend does not always have to be monotonic. We show a different design of periodically arranged rings in a triangular lattice, where local minima and maxima in the band dispersion are observed.

We believe that the precise selection of the dispersion of the topological mode plays a crucial role in specific applications, and the tradeoff between dispersion and band-gap size should therefore be carefully considered.

Conclusion

This work presents the complete process of designing and characterizing a topological interface in two-dimensional photonic crystals. It describes the theoretical background and computational tools necessary for both the design and the selection of the most suitable approach. The thesis introduces an automated band-connection method together with a band eigenfunction classification technique for eigenmode inversion recognition. It outlines the available degrees of freedom in topological design and demonstrates the trade-offs that must be considered when optimizing geometrical and physical parameters. Beyond the final methods and conclusions, the work also includes exploratory directions and documents the unsuccessful or preliminary attempts that contributed to reaching the final understanding.

The first chapter established the theoretical and conceptual foundation for the study of topological photonic crystals. It introduced the fundamental principles of photonic band theory and the analogy between electronic and photonic topological systems, emphasizing how concepts such as the Berry phase, Chern number, and bulk–edge correspondence translate into the photonic domain. The chapter also reviewed the current state of the art in topological photonics, summarizing the main experimental and theoretical achievements as well as their practical limitations. Different classes of photonic topologies, including Chern, Valley-Chern, and Obstructed Atomic Limit phases, were discussed with respect to their physical mechanisms and material requirements.

The second chapter introduced the numerical methods and computational tools used throughout this thesis. It described the implementation and validation of the eigenmode solver based on the MIT Photonic Bands package and the time-domain analysis performed using the Finite-Difference Time-Domain method. Together, these approaches provided complementary insights into the frequency- and time-domain behavior of photonic crystals, enabling both band structure analysis and direct field propagation studies. The chapter also detailed the workflow automation and data handling developed in Python, which allowed efficient exploration of large parameter spaces and reproducibility of the results. By benchmarking the simulations against known photonic structures from the literature, the reliability and accuracy of the implemented methods were verified.

The third chapter focused on the investigation of Chern-type photonic topology and the development of automated tools for its numerical identification. It introduced an algorithm for automated band connection based on eigenmode similarity, enabling consistent tracking of eigenmodes across the Brillouin zone and reliable detection of band crossings and degeneracies. Using this framework, the parameter space of gyrotropic photonic crystals was systematically explored to identify configurations supporting nontrivial Chern numbers. The results demonstrated the theoretical feasibility of Chern-type topology but also revealed its practical limitations at optical frequencies, where the required gyromagnetic response is unrealistically strong. This finding highlighted the need for alternative

topological mechanisms compatible with dielectric materials. Consequently, the conclusions of this chapter motivated a shift in focus toward symmetry-protected topologies, such as the obstructed atomic limit, which can be realized without breaking time-reversal symmetry.

The fourth chapter introduced a generalized method for automated recognition of eigenmode inversion in photonic crystals, independent of the specific lattice symmetry. It presented a classification approach based on eigenfunction comparison, where the spatial distribution and sign pattern of the field components were used to quantify the similarity between modes. This method enabled reliable identification of symmetry inversions that mark transitions between topologically distinct phases. By combining this technique with the previously developed band-connection algorithm, the analysis of complex parameter spaces became fully automated and scalable. The approach was tested on representative photonic crystal geometries, confirming its ability to detect mode inversions corresponding to topological transitions.

The fifth chapter applied the developed automated analysis methods to search for eigenmode inversions in two-dimensional photonic crystals with C_4 symmetry. A range of geometrical configurations was investigated to identify structures capable of supporting the desired p–d mode inversion associated with the obstructed atomic limit phase. Through systematic parameter exploration, the "bridged ring" geometry emerged as the most effective design, allowing continuous tuning of the inversion by adjusting the bridge width and cavity radius. Supercell simulations confirmed the formation of a topological interface state when two complementary geometries with inverted symmetries were combined, demonstrating clear bulk–edge correspondence. The chapter also discussed the role of lattice periodicity, symmetry constraints, and material parameters in determining the robustness and manufacturability of the design. Overall, this chapter established a practical realization of the topological interface and provided the central example on which the subsequent characterization was based.

The final chapter focused on the detailed characterization of the topological modes formed at the interface between the complementary photonic crystal structures. Using both frequency-domain and time-domain simulations, the existence, spatial localization, and dispersion of the interface states were confirmed. The analysis demonstrated that these modes are confined within a few lattice periods around the interface and remain robust in the presence of structural imperfections, validating their topological origin. The Wilson loop calculations further verified that the observed modes arise from a displacement of Wannier centers characteristic of the obstructed atomic limit phase, rather than from local symmetry breaking. Additional studies examined the dependence of mode confinement and group velocity on the size of the band-gap overlap, revealing a trade-off between localization and dispersion slope that can be tuned geometrically. Together, these results provided a comprehensive understanding of the physical behavior of OAL topological modes and confirmed the success of the design and analysis framework developed throughout the thesis.

A natural continuation of this research is to extend the automated analysis framework beyond the specific C_4 OAL case studied here. The band-connection algorithm based on eigenmode similarity provides a general mechanism for tracking eigenstates across the Brillouin zone, enabling reliable detection of crossings, degeneracies, and symmetry changes without manual intervention. Combined with automated eigenfunction-based classification, this approach can be adapted to other lattice symmetries, higher-order topological phases, and potentially three-dimensional photonic crystals, where band connectivity becomes more complex and mode mixing is more common. In parallel, a systematic investigation of robustness under experimentally realistic conditions remains essential. While the interface modes were shown to persist under severe perturbations, the observed asymmetry in defect sensitivity and the reduced performance of certain turns indicate that robustness is geometry-dependent and must be quantified in a controlled way. Extending the defect studies to fabrication-relevant variations, including smooth shape perturbations, positional disorder, and material losses, would allow a more complete mapping between unit-cell parameters, mode localization asymmetry, and practical suitability for integrated implementations.

In addition to these direct extensions, the thesis opens several opportunities for expanding the design space and targeting application-driven functionality. The demonstrated trade-off between band-gap overlap and interface-mode dispersion suggests that low-dispersion and near-flat modes can be engineered intentionally, which could be useful for slow-light applications and protection systems where reduced group velocity is beneficial. At the design level, fractional lattice-parameter matching provides an additional tuning knob for band-gap alignment without changing material composition, potentially enabling interface formation between designs that would otherwise be incompatible under a 1:1 scaling constraint. Although this strategy increases computational cost and introduces multiple edge bands, it broadens the range of viable complementary pairs and motivates more efficient supercell workflows. Finally, the exploratory generative geometry approach suggests a route toward automated unit-cell synthesis guided by eigenmode ordering and field–material overlap, which could reduce reliance on heuristic geometry selection. While the initial implementation suffered from local optima and did not achieve the targeted ordering, the underlying idea can be developed using more stable optimization strategies, enabling future inverse-design pipelines that couple automated band tracking, mode classification, and geometry generation into a single closed-loop design process.

Bibliography

1. Tkachov, Gregory. *Topological insulators: The physics of spin helicity in quantum transport*. CRC Press, 2015.
2. Ozawa, Tomoki; Price, Hannah M; Amo, Alberto; Goldman, Nathan; Hafezi, Mohammad; Lu, Ling; Rechtsman, Mikael C; Schuster, David; Simon, Jonathan; Zilberberg, Oded, et al. Topological photonics. *Reviews of Modern Physics*. 2019, vol. 91, no. 1, p. 015006.
3. Lu, Ling; Joannopoulos, John D; Soljačić, Marin. Topological photonics. *Nature photonics*. 2014, vol. 8, no. 11, pp. 821–829.
4. Berry, Michael Victor. Quantal phase factors accompanying adiabatic changes. *Proceedings of the Royal Society of London. A. Mathematical and Physical Sciences*. 1984, vol. 392, no. 1802, pp. 45–57.
5. Wang, Zhong; Qi, Xiao-Liang; Zhang, Shou-Cheng. Equivalent topological invariants of topological insulators. *New journal of physics*. 2010, vol. 12, no. 6, p. 065007.
6. Hasan, M Zahid; Kane, Charles L. Colloquium: topological insulators. *Reviews of modern physics*. 2010, vol. 82, no. 4, pp. 3045–3067.
7. Hatsugai, Yasuhiro. Chern number and edge states in the integer quantum Hall effect. *Physical review letters*. 1993, vol. 71, no. 22, p. 3697.
8. Haldane, F Duncan M. Model for a quantum Hall effect without Landau levels: Condensed-matter realization of the" parity anomaly". *Physical review letters*. 1988, vol. 61, no. 18, p. 2015.
9. Liu, Wenjing; Hwang, Minsoo; Ji, Zhurun; Wang, Yuhui; Modi, Gaurav; Agarwal, Ritesh. Z2 photonic topological insulators in the visible wavelength range for robust nanoscale photonics. *Nano Letters*. 2020, vol. 20, no. 2, pp. 1329–1335.
10. Arora, Sonakshi; Bauer, Thomas; Parappurath, Nikhil; Barczyk, René; Verhagen, Ewold; Kuipers, L. Breakdown of spin-to-helicity locking at the nanoscale in topological photonic crystal edge states. *Physical Review Letters*. 2022, vol. 128, no. 20, p. 203903.
11. Li, Mengyao; Sinev, Ivan; Benimetskiy, Fedor; Ivanova, Tatyana; Khestanova, Ekaterina; Kiriushechkina, Svetlana; Vakulenko, Anton; Guddala, Sriram; Skolnick, Maurice; Menon, Vinod M, et al. Experimental observation of topological Z2 exciton-polaritons in transition metal dichalcogenide monolayers. *Nature communications*. 2021, vol. 12, no. 1, p. 4425.
12. Funayama, Keita; Yatsugi, Kenichi; Miura, Atsushi; Iizuka, Hideo. Control of coupling between micromechanical topological waveguides. *International Journal of Mechanical Sciences*. 2022, vol. 236, p. 107755.
13. Wang, Zheng; Chong, Yidong; Joannopoulos, John D; Soljačić, Marin. Observation of unidirectional backscattering-immune topological electromagnetic states. *Nature*. 2009, vol. 461, no. 7265, pp. 772–775.

14. Hafezi, Mohammad; Demler, Eugene A; Lukin, Mikhail D; Taylor, Jacob M. Robust optical delay lines with topological protection. *Nature Physics*. 2011, vol. 7, no. 11, pp. 907–912.

15. Ma, Tzuhsuan; Shvets, Gennady. All-Si valley-Hall photonic topological insulator. *New Journal of Physics*. 2016, vol. 18, no. 2, p. 025012.

16. Dong, Jian-Wen; Chen, Xiao-Dong; Zhu, Hanyu; Wang, Yuan; Zhang, Xiang. Valley photonic crystals for control of spin and topology. *Nature materials*. 2017, vol. 16, no. 3, pp. 298–302.

17. Xie, Bi-Ye; Wang, Hong-Fei; Wang, Hai-Xiao; Zhu, Xue-Yi; Jiang, Jian-Hua; Lu, Ming-Hui; Chen, Yan-Feng. Second-order photonic topological insulator with corner states. *Physical Review B*. 2018, vol. 98, no. 20, p. 205147.

18. Mittal, Sunil; Orre, Venkata Vikram; Zhu, Guanyu; Gorlach, Maxim A; Poddubny, Alexander; Hafezi, Mohammad. Photonic quadrupole topological phases. *Nature Photonics*. 2019, vol. 13, no. 10, pp. 692–696.

19. Feng, Liang; El-Ganainy, Ramy; Ge, Li. Non-Hermitian photonics based on parity–time symmetry. *Nature Photonics*. 2017, vol. 11, no. 12, pp. 752–762.

20. Blanco de Paz, Maria; Devescovi, Chiara; Giedke, Geza; Saenz, Juan José; Vergniory, Maia G; Bradlyn, Barry; Bercioux, Dario; García-Etxarri, Aitzol. Tutorial: computing topological invariants in 2D photonic crystals. *Advanced Quantum Technologies*. 2020, vol. 3, no. 2, p. 1900117.

21. Jones, Douglas Samuel. *The theory of electromagnetism*. Elsevier, 2013.

22. Watanabe, Haruki. A proof of the Bloch theorem for lattice models. *Journal of Statistical Physics*. 2019, vol. 177, no. 4, pp. 717–726.

23. Joannopoulos, John D; Johnson, Steven G; Winn, Joshua N; Meade, Robert D. Molding the flow of light. *Princet. Univ. Press. Princeton, NJ [ua]*. 2008, vol. 12.

24. Johnson, Steven G; Joannopoulos, John D. Block-iterative frequency-domain methods for Maxwell's equations in a planewave basis. *Optics express*. 2001, vol. 8, no. 3, pp. 173–190.

25. Sullivan, Dennis M. *Electromagnetic simulation using the FDTD method*. John Wiley & Sons, 2013.

26. Inan, Umran S; Marshall, Robert A. *Numerical electromagnetics: the FDTD method*. Cambridge University Press, 2011.

27. Oskooi, Ardavan F; Roundy, David; Ibanescu, Mihai; Bermel, Peter; Joannopoulos, John D; Johnson, Steven G. MEEP: A flexible free-software package for electromagnetic simulations by the FDTD method. *Computer Physics Communications*. 2010, vol. 181, no. 3, pp. 687–702.

28. Guide, Installation. Comsol Multiphysics. *5.6, COMSOL AB*. 1998, pp. 204–8.

29. Chern, Shiing-shen. Characteristic classes of Hermitian manifolds. *Annals of Mathematics*. 1946, vol. 47, no. 1, pp. 85–121.

30. Raghu, Srinivas; Haldane, Frederick Duncan Michael. Analogs of quantum-Hall-effect edge states in photonic crystals. *Physical Review A–Atomic, Molecular, and Optical Physics*. 2008, vol. 78, no. 3, p. 033834.

31. Stone, Michael. *Quantum Hall Effect*. World Scientific, 1992.

32. Vanderbilt, David. *Berry phases in electronic structure theory: electric polarization, orbital magnetization and topological insulators*. Cambridge University Press, 2018.

33. Pancharatnam, Shivaramakrishnan. Generalized theory of interference, and its applications: Part I. Coherent pencils. In: *Proceedings of the Indian Academy of Sciences-Section A*. Springer, 1956, vol. 44, pp. 247–262. No. 5.

34. Zak, J. Berry's phase for energy bands in solids. *Physical review letters*. 1989, vol. 62, no. 23, p. 2747.

35. Katz, Victor J. The history of Stokes' theorem. *Mathematics Magazine*. 1979, vol. 52, no. 3, pp. 146–156.

36. Bouckaert, Louis P; Smoluchowski, Roman; Wigner, Eo. Theory of Brillouin zones and symmetry properties of wave functions in crystals. *Physical Review*. 1936, vol. 50, no. 1, p. 58.

37. Chadi, D Jetal; Cohen, Marvin L. Special points in the Brillouin zone. *Physical Review B*. 1973, vol. 8, no. 12, p. 5747.

38. Benalcazar, Wladimir A; Li, Tianhe; Hughes, Taylor L. Quantization of fractional corner charge in C n-symmetric higher-order topological crystalline insulators. *Physical Review B*. 2019, vol. 99, no. 24, p. 245151.

39. Marzari, Nicola; Vanderbilt, David. Maximally localized generalized Wannier functions for composite energy bands. *Physical review B*. 1997, vol. 56, no. 20, p. 12847.

40. Bradlyn, Barry; Elcoro, L; Vergniory, MG; Cano, Jennifer; Wang, Zhijun; Felser, C; Aroyo, MI; Bernevig, B Andrei. Band connectivity for topological quantum chemistry: Band structures as a graph theory problem. *Physical Review B*. 2018, vol. 97, no. 3, p. 035138.

41. Skirlo, Scott A; Lu, Ling; Igarashi, Yuichi; Yan, Qinghui; Joannopoulos, John; Soljačić, Marin. Experimental observation of large Chern numbers in photonic crystals. *Physical review letters*. 2015, vol. 115, no. 25, p. 253901.

42. Chen, Wen-Jie; Xiao, Meng; Chan, Che Ting. Photonic crystals possessing multiple Weyl points and the experimental observation of robust surface states. *Nature communications*. 2016, vol. 7, no. 1, p. 13038.

43. Wang, Zheng; Chong, YD; Joannopoulos, John D; Soljačić, Marin. Reflection-free one-way edge modes in a gyromagnetic photonic crystal. *Physical review letters*. 2008, vol. 100, no. 1, p. 013905.

44. Fang, Chen; Gilbert, Matthew J; Bernevig, B Andrei. Bulk topological invariants in noninteracting point group symmetric insulators. *Physical Review B—Condensed Matter and Materials Physics*. 2012, vol. 86, no. 11, p. 115112.

45. Liu, Feng; Deng, Hai-Yao; Wakabayashi, Katsunori. Topological photonic crystals with zero Berry curvature. *Physical Review B*. 2018, vol. 97, no. 3, p. 035442.

46. Wang, Hai-Xiao; Jiang, Jian-Hua. A short review of all-dielectric topological photonic crystals. *Frontiers in Physics*. 2022, vol. 10, p. 866552.

47. Tang, Guo-Jing; He, Xin-Tao; Shi, Fu-Long; Liu, Jian-Wei; Chen, Xiao-Dong; Dong, Jian-Wen. Topological photonic crystals: physics, designs, and applications. *Laser & Photonics Reviews*. 2022, vol. 16, no. 4, p. 2100300.

48. Zhirihin, Dmitry V; Kivshar, Yuri S. Topological photonics on a small scale. *Small Science*. 2021, vol. 1, no. 12, p. 2100065.

49. Wang, Hongfei; Gupta, Samit Kumar; Xie, Biye; Lu, Minghui. Topological photonic crystals: a review. *Frontiers of Optoelectronics*. 2020, vol. 13, pp. 50–72.

50. Wu, Long-Hua; Hu, Xiao. Scheme for achieving a topological photonic crystal by using dielectric material. *Physical review letters*. 2015, vol. 114, no. 22, p. 223901.

51. Xu, Lin; Wang, Hai-Xiao; Xu, Ya-Dong; Chen, Huan-Yang; Jiang, Jian-Hua. Accidental degeneracy in photonic bands and topological phase transitions in two-dimensional core-shell dielectric photonic crystals. *Optics express*. 2016, vol. 24, no. 16, pp. 18059–18071.

52. Palmer, Samuel J; Giannini, Vincenzo. Berry bands and pseudo-spin of topological photonic phases. *Physical Review Research*. 2021, vol. 3, no. 2, p. L022013.

53. Huang, Jing-Yu; Xu, Xiao-Fang; Zhang, Hao; Zhai, Nan; Liu, Ya-Qi. Topological boundary states of two-dimensional restricted isosceles triangular photonic crystals. *Applied Optics*. 2022, vol. 61, no. 5, pp. 1254–1260.

54. Jin, Meng-Cheng; Gao, Yong-Feng; Huang, Guang-Yao; He, Yi-Han; Sun, Jia-Ping; Song, He. Manipulation of coupling between waveguide and ring resonator in topological photonic crystals. *Physica E: Low-dimensional Systems and Nanostructures*. 2022, vol. 136, p. 115013.

55. Du, Zongliang; Ding, Xianggui; Chen, Hui; Liu, Chang; Zhang, Weisheng; Luo, Jiachen; Guo, Xu. Optimal design of topological waveguides by machine learning. *Frontiers in Materials*. 2022, vol. 9, p. 1075073.

56. He, Liu; Lan, Zhihao; Yang, Yuting; Ren, Qun; You, Jian Wei; Sha, Wei EI; Liang, Wu; Yao, Jianquan. Wavelength division multiplexing based on the coupling effect of helical edge states in two-dimensional dielectric photonic crystals. *Optics Express*. 2024, vol. 32, no. 7, pp. 11259–11270.

57. Sharma, Arvind K; Madhusudan, Meghna; Burns, Steven M; Mukherjee, Parijat; Yaldiz, Soner; Harjani, Ramesh; Sapatnekar, Sachin S. Common-centroid layouts for analog circuits: Advantages and limitations. In: *2021 Design, Automation & Test in Europe Conference & Exhibition (DATE)*. IEEE, 2021, pp. 1224–1229.

58. He, Yi-Han; Gao, Yong-Feng; Lin, Hao-Zhe; Jin, Meng-Cheng; He, Yue; Qi, Xiao-Fei. Topological edge and corner states based on the transformation and combination of photonic crystals with square lattice. *Optics Communications*. 2022, vol. 512, p. 128038.

59. Xiong, Langlang; Liu, Yufu; Zhang, Yu; Zheng, Yaoxian; Jiang, Xunya. Topological properties of a two-dimensional photonic square lattice without C 4 and M x (y) symmetries. *Acs Photonics*. 2022, vol. 9, no. 7, pp. 2448–2454.

60. Zhang, Qichen; Chen, Jianzhi; Liu, Dongyang; Liu, Jianjun. Topological states in Penrose-square photonic crystals. *Journal of the Optical Society of America A*. 2024, vol. 41, no. 8, pp. 1611–1615.

61. Devescovi, Chiara; Morales-Pérez, Antonio; Blanco de Paz, Maria; Luis Mañes, Juan; Bradlyn, Barry; Vergniory, Maia G; García-Etxarri, Aitzol. Tutorial 2.0: computing topological invariants in 3D photonic crystals. *Optical Materials Express*. 2024, vol. 14, no. 9, pp. 2161–2177.

62. Wang, Hai-Xiao; Guo, Guang-Yu; Jiang, Jian-Hua. Band topology in classical waves: Wilson-loop approach to topological numbers and fragile topology. *New Journal of Physics*. 2019, vol. 21, no. 9, p. 093029.

63. Christiansen, Rasmus E; Wang, Fengwen; Sigmund, Ole; Stobbe, Søren. Designing photonic topological insulators with quantum-spin-Hall edge states using topology optimization. *Nanophotonics*. 2019, vol. 8, no. 8, pp. 1363–1369.

64. Christiansen, Rasmus E; Wang, Fengwen; Sigmund, Ole. Topological insulators by topology optimization. *Physical Review Letters*. 2019, vol. 122, no. 23, p. 234502.

65. Kagami, Hibiki; Amemiya, Tomohiro; Okada, Shou; Nishiyama, Nobuhiko; Hu, Xiao. Topological converter for high-efficiency coupling between Si wire waveguide and topological waveguide. *Optics Express*. 2020, vol. 28, no. 22, pp. 33619–33631.

66. Kagami, Hibiki; Amemiya, Tomohiro; Okada, Sho; Nishiyama, Nobuhiko; Hu, Xiao. Highly efficient vertical coupling to a topological waveguide with defect structure. *Optics Express*. 2021, vol. 29, no. 21, pp. 32755–32763.

67. Zhang, Furong; He, Lu; Zhang, Huizhen; Kong, Ling-Jun; Xu, Xingsheng; Zhang, Xiangdong. Experimental realization of topologicallyall-optical logic gates based on silicon photonic crystal slabs. *Laser & Photonics Reviews*. 2023, vol. 17, no. 8, p. 2200329.

68. Xie, Xin; Yan, Sai; Dang, Jianchen; Yang, Jingnan; Xiao, Shan; Wang, Yunuan; Shi, Shushu; Yang, Longlong; Dai, Danjie; Yuan, Yu, et al. Topological cavity based on slow-light topological edge mode for broadband Purcell enhancement. *Physical Review Applied*. 2021, vol. 16, no. 1, p. 014036.

69. Kumar, Abhishek; Tan, Yi Ji; Navaratna, Nikhil; Gupta, Manoj; Pitchappa, Prakash; Singh, Ranjan. Slow light topological photonics with counter-propagating waves and its active control on a chip. *Nature Communications*. 2024, vol. 15, no. 1, p. 926.

70. Hammond, Alec M; Oskooi, Ardavan; Chen, Mo; Lin, Zin; Johnson, Steven G; Ralph, Stephen E. High-performance hybrid time/frequency-domain topology optimization for large-scale photonics inverse design. *Optics Express*. 2022, vol. 30, no. 3, pp. 4467–4491.

71. Knyazev, Andrew V. Toward the optimal preconditioned eigensolver: Locally optimal block preconditioned conjugate gradient method. *SIAM journal on scientific computing*. 2001, vol. 23, no. 2, pp. 517–541.

72. Andueza, Ángel; Sevilla, Joaquín; Pérez-Conde, Jesús; Wang, Kang. Shear based gap control in 2D photonic quasicrystals of dielectric cylinders. *Optics Express*. 2021, vol. 29, no. 14, pp. 22159–22169.

73. Kittel, Charles; McEuen, Paul. *Introduction to solid state physics*. John Wiley & Sons, 2018.

74. *MPB: Python User Interface* [`https://mpb.readthedocs.io/en/latest/Python_User_Interface/`]. 2025. Accessed: 2025-12-01.

75. Bray, MG; Werner, DH. A simple dispersive Chiral FDTD formulation implemented on a Yee grid. In: *2005 IEEE Antennas and Propagation Society International Symposium*. IEEE, 2005, vol. 1, pp. 126–129.

76. Palik, Edward D. *Handbook of optical constants of solids*. Vol. 3. Academic press, 1998.

77. Palik, Edward D et al. *Handbook of optical constants of solids II*. Academic press New York, 1991.

78. Joannopoulos, John D; Villeneuve, Pierre R; Fan, Shanhui. Photonic crystals. *Solid State Communications*. 1997, vol. 102, no. 2-3, pp. 165–173.

79. Yablonovitch, Eli. Photonic crystals. *Journal of Modern Optics*. 1994, vol. 41, no. 2, pp. 173–194.

80. Multiphysics, COMSOL. Introduction to COMSOL multiphysics®. *COMSOL Multiphysics, Burlington, MA, accessed Feb*. 1998, vol. 9, p. 2018.

81. He, Wen-Yu; Chan, CT. The emergence of Dirac points in photonic crystals with mirror symmetry. *Scientific reports*. 2015, vol. 5, no. 1, p. 8186.

82. Novák, Ondřej; Herranz, Gervasi; Veis, Martin. Methodology for Topological Interface Engineering in 2D Photonic Crystals. *Advanced Photonics Research*. 2025, e202500135.

83. Xu, Rui; Wunsch, Donald. Survey of clustering algorithms. *IEEE Transactions on neural networks*. 2005, vol. 16, no. 3, pp. 645–678.

84. Ahuja, Ravinder; Chug, Aakarsha; Gupta, Shaurya; Ahuja, Pratyush; Kohli, Shruti. Classification and clustering algorithms of machine learning with their applications. *Nature-inspired computation in data mining and machine learning*. 2020, pp. 225–248.

85. He, Cheng; Sun, Xiao-Chen; Liu, Xiao-Ping; Lu, Ming-Hui; Chen, Yulin; Feng, Liang; Chen, Yan-Feng. Photonic topological insulator with broken time-reversal symmetry. *Proceedings of the National Academy of Sciences*. 2016, vol. 113, no. 18, pp. 4924–4928.

86. Wang, Chenyang; Zhang, Hongyu; Yuan, Hongyi; Zhong, Jinrui; Lu, Cuicui. Universal numerical calculation method for the Berry curvature and Chern numbers of typical topological photonic crystals. *Frontiers of Optoelectronics*. 2020, vol. 13, pp. 73–88.

87. Tsutaoka, Takanori; Kasagi, Teruhiro; Hatakeyama, Kenichi. Permeability spectra of yttrium iron garnet and its granular composite materials under dc magnetic field. *Journal of Applied Physics*. 2011, vol. 110, no. 5.

88. Bush, Gary G. The complex permeability of a high purity yttrium iron garnet (YIG) sputtered thin film. *Journal of applied physics*. 1993, vol. 73, no. 10, pp. 6310–6311.

89. Li, Shuo; Lin, Han; Meng, Fei; Moss, David; Huang, Xiaodong; Jia, Baohua. On-demand design of tunable complete photonic band gaps based on bloch mode analysis. *Scientific reports*. 2018, vol. 8, no. 1, p. 14283.

90. Malỳ, Petr. *Optika*. Charles University in Prague, Karolinum Press, 2020.

91. Singh, Leena; Singh, Ranjan; Zhang, Weili. Ultra-high terahertz index in deep subwavelength coupled bi-layer free-standing flexible metamaterials. *Journal of Applied Physics*. 2017, vol. 121, no. 23.

92. Smith, DR; Vier, DC; Koschny, Th; Soukoulis, CM. Electromagnetic parameter retrieval from inhomogeneous metamaterials. *Physical Review E—Statistical, Nonlinear, and Soft Matter Physics*. 2005, vol. 71, no. 3, p. 036617.

93. Arslanagić, Samel; Hansen, Troels Vejle; Mortensen, N Asger; Gregersen, Anders Heidemann; Sigmund, Ole; Ziolkowski, Richard W; Breinbjerg, Olav. A review of the scattering-parameter extraction method with clarification of ambiguity issues in relation to metamaterial homogenization. *IEEE Antennas and Propagation Magazine*. 2013, vol. 55, no. 2, pp. 91–106.

94. Krauss, Thomas F. Slow light in photonic crystal waveguides. *Journal of Physics D: Applied Physics*. 2007, vol. 40, no. 9, p. 2666.

95. Noda, Susumu; Baba, Toshihiko. *Roadmap on photonic crystals*. Springer Science & Business Media, 2013.

96. Rong, Bifeng; Drift, Emile van der; Heijden, Rob W van der; Salemink, Huub WM. 2D InP photonic crystal fabrication process development. In: *Nanoengineering: Fabrication, Properties, Optics, and Devices III*. SPIE, 2006, vol. 6327, pp. 245–254.

97. Halioua, Yacine; Karle, TJ; Raineri, F; Monnier, P; Sagnes, I; Roelkens, Günther; Van Thourhout, Dries; Raj, R. Hybrid InP-based photonic crystal lasers on silicon on insulator wires. *Applied Physics Letters*. 2009, vol. 95, no. 20.

98. Ek, Sara; Lunnemann, Per; Chen, Yaohui; Semenova, Elizaveta; Yvind, Kresten; Mork, Jesper. Slow-light-enhanced gain in active photonic crystal waveguides. *Nature Communications*. 2014, vol. 5, no. 1, p. 5039.

99. Sakoda, Kazuaki; Sakoda, K. *Optical properties of photonic crystals*. Vol. 2. Springer, 2005.

100. Wang, HaiXiao; Xu, Lin; Chen, HuanYang; Jiang, Jian-Hua. Three-dimensional photonic Dirac points stabilized by point group symmetry. *Physical Review B*. 2016, vol. 93, no. 23, p. 235155.

101. Ochiai, Tetsuyuki. Gapless surface states originating from accidentally degenerate quadratic band touching in a three-dimensional tetragonal photonic crystal. *Physical Review A*. 2017, vol. 96, no. 4, p. 043842.

102. Sakoda, Kazuaki. Proof of the universality of mode symmetries in creating photonic Dirac cones. *Optics express*. 2012, vol. 20, no. 22, pp. 25181–25194.

103. Wu, Long-Hua; Hu, Xiao. Topological properties of electrons in honeycomb lattice with detuned hopping energy. *Scientific reports*. 2016, vol. 6, no. 1, p. 24347.

104. Chen, Yang; Chen, Xiaoman; Ren, Xifeng; Gong, Ming; Guo, Guang-can. Tight-binding model in optical waveguides: Design principle and transferability for simulation of complex photonics networks. *Physical Review A*. 2021, vol. 104, no. 2, p. 023501.

105. Wang, Ziyao; Meng, Yan; Yan, Bei; Zhao, Dong; Yang, Linyun; Chen, Jingming; Cheng, Minqi; Xiao, Tao; Shum, Perry Ping; Liu, Gui-Geng, et al. Realization of a three-dimensional photonic higher-order topological insulator. *Nature Communications*. 2025, vol. 16, no. 1, p. 3122.

106. Cui, Mengyao et al. Introduction to the k-means clustering algorithm based on the elbow method. *Accounting, Auditing and Finance*. 2020, vol. 1, no. 1, pp. 5–8.

107. Syakur, Muhammad Ali; Khotimah, B Khusnul; Rochman, EMS; Satoto, Budi Dwi. Integration k-means clustering method and elbow method for identification of the best customer profile cluster. In: *IOP conference series: materials science and engineering*. IOP Publishing, 2018, vol. 336, p. 012017.

108. Novák, Ondřej; Veis, Martin; Herranz, Gervasi. Obstructed atomic limit topological protection in C4-symmetricphotonic crystals for optical communications. *Journal of Optics*. 2025.

109. Lai, Zhen; Liu, Yufu; Li, Yunlin; Wang, Xuezhi; Jiang, Xunya. The Nested Topological Band-Gap Structure for the Periodic Domain Walls in a Photonic Super-Lattice. *Crystals*. 2024, vol. 14, no. 9, p. 757.

110. Sharma, Richa; Jena, Shuvendu; Udupa, Dinesh V. Coupling of topological interface states in 1D photonic crystal. *Optical Materials*. 2023, vol. 137, p. 113508.

111. Dios-Leyva, Melquiades de; Márquez-González, Andy; Duque, Carlos Alberto. Exploring photonic crystals: Band structure and topological interface states. *Condensed Matter*. 2023, vol. 8, no. 3, p. 63.

112. Borges-Silva, Daniel; Costa, Carlos Humberto Oliveira; Bezerra, Claudionor Gomes. Robust topological edge states in C 6 photonic crystals. In: *Photonics*. MDPI, 2023, vol. 10, p. 961. No. 9.

113. Tamm, Kert; Peets, Tanel; Engelbrecht, Jüri; Kartofelev, Dmitri. Negative group velocity in solids. *Wave Motion*. 2017, vol. 71, pp. 127–138.

114. Cheng, Qi; Wang, Shutao; Lv, Jiangtao; Liu, Na. Topological photonic crystal biosensor with valley edge modes based on a silicon-on-insulator slab. *Optics Express*. 2022, vol. 30, no. 7, pp. 10792–10801.

115. El. Soliman, Sayed; Abood, Israa; All, Naglaa Abdel; Chen, Chii-Chang. Topological Rainbow Trapping with Expanded Bandwidth in Valley Photonic Crystals. In: *Photonics*. MDPI, 2025, vol. 12, p. 487. No. 5.

116. Yoshimi, Hironobu; Yamaguchi, Takuto; Katsumi, Ryota; Ota, Yasutomo; Arakawa, Yasuhiko; Iwamoto, Satoshi. Experimental demonstration of topological slow light waveguides in valley photonic crystals. *Optics Express*. 2021, vol. 29, no. 9, pp. 13441–13450.

117. Lin, Yu-Chuan; Chien, Yi-Chia; Hsueh, Wen-Jeng. Topological slow-light in one-dimensional conjugated photonic systems. *Optics Communications*. 2024, vol. 558, p. 130369.

118. Wang, Yanan; Wang, Hai-Xiao; Liang, Li; Zhu, Weiwei; Fan, Longzhen; Lin, Zhi-Kang; Li, Feifei; Zhang, Xiao; Luan, Pi-Gang; Poo, Yin, et al. Hybrid topological photonic crystals. *Nature Communications*. 2023, vol. 14, no. 1, p. 4457.

119. Landers, Serena; Tuxbury, William; Vitebskiy, Ilya; K̃ottos, Tsampikos. Robust nonlinear isolators based on frozen mode exceptional point degeneracies. *Physical Review Research*. 2025, vol. 7, no. 1, p. 013110.

120. Adachi, Sadao. Optical dispersion relations for GaP, GaAs, GaSb, InP, InAs, InSb, Al x Ga1- x As, and In1- x Ga x As y P1- y. *Journal of Applied Physics*. 1989, vol. 66, no. 12, pp. 6030–6040.

List of Figures

1.1 An example of an unconnected photonic band structure obtained using MPB is shown for a system of rods arranged in a triangular lattice with a relative permittivity of $\varepsilon = 10$ and a rod radius of $r_{\text{rod}} = 0.3075 \cdot a$. The calculation is performed for TM modes for the first five eigenvalues. 11

1.2 Interface between the topological and trivial photonic crystal . . . 12

1.3 **a)** An illustration of a band structure in a quantum Hall system showing a single gapless edge mode. **b)** An illustration of a two-dimensional electron system with an external magnetic field, which induces a chiral edge state by breaking time-reversal symmetry. . 12

1.4 Discretization of the Brillouin zone for Berry phase calculations. **a)** A single plaquette, whose edges define the path γ. **b)** Discretization of the Brillouin zone into an $N \times N$ grid of plaquettes. 13

1.5 Example of Wilson loops. a) Wilson loop of a single trivial band, showing no winding, corresponding to a Chern number $\mathbb{C} = 0$. b) Wilson loop of a topologically non-trivial band where the Wannier centers wind in the negative direction, corresponding to $\mathbb{C} = -1$. c) Wilson loop of a topologically non-trivial band where the Wannier centers wind twice in the positive direction, corresponding to $\mathbb{C} = 2$. d) Wilson loops of a set of two bands, where the Wannier centers are slightly displaced but show no winding, corresponding to $\mathbb{C} = 0$. 16

2.1 Geometry of the unit cell of the PC defined in [53]. Free parameters are displacement d, triangular base b, triangular height h and the rotation of triangles Θ. **a)** $\Theta = 0°$ **b)** $\Theta = 180°$ 20

2.2 The depiction illustrates the MPB base vectors in real space. The vectors $\boldsymbol{a}_1 = a\left(\frac{\sqrt{3}}{2}, \frac{1}{2}\right)$ and $\boldsymbol{a}_2 = a\left(\frac{\sqrt{3}}{2}, -\frac{1}{2}\right)$ define a triangular lattice. Red markers indicate positions in the new basis with coordinates $\boldsymbol{p}_1 = (1, -1)$ and $\boldsymbol{p}_2 = \left(0, -\frac{1}{2}\right)$. The blue parallelogram represents the unit cell of the photonic crystal. 21

2.3 The formation of the Brillouin zone and the irreducible Brillouin zone based on the basis vectors defined in Figure 2.2. The reciprocal lattice vectors are $\boldsymbol{b}_1 = \frac{2\pi}{a}\left(\frac{1}{\sqrt{3}}, 1\right)$ and $\boldsymbol{b}_2 = \frac{2\pi}{a}\left(\frac{1}{\sqrt{3}}, -1\right)$. The high-symmetry points in this reciprocal space basis are $\boldsymbol{\Gamma} = (0, 0)$, $\boldsymbol{M} = \left(0, \frac{1}{2}\right)$, and $\boldsymbol{K} = \left(-\frac{1}{3}, \frac{1}{3}\right)$. 22

2.4 Plot of permittivity of the geometry defined in the code above. Black color represents material. Parameters used were same as in [53]. $(H = 0.2a; D = 0.3a; B = 0.28a; \varepsilon_r = 12)$. Resolution of the solver was increased to 128 for better plot quality. 25

2.5 Bandstructures of PC unit cells designed by Huang in [53]. Fixed parameters are: $H = 0.2a; D = 0.3a; B = 0.28a; \varepsilon_r = 12$, the PC geometry is depicted in the bottom right corner. (a) $\Theta = 0°$, the PC is in topologically trivial state (b) $\Theta = 122°$, the band-gap closes, the PC is in a process of topological tzransition (c) $\Theta = 180°$, the PC is in topologicaly non-trivial state 27

2.6 Eigenmodes of the PC designed by Huang [53] at Γ. Countours of the underlying structure are shown. The images depicts the real part of E_z field with a fixed phase. 28
2.7 Example of a unit-cell for interface MPB calculations. **a)** single unit-cell defined in MPB geometry list. **b)** Pattern prodiced by periodical repetition of the Unit-cell, mimicing the topological interface. 29
2.8 Reproduction of the topological interface band structure calculation done by Huang [53]. 8 topologically trivial PC unit cells and 8 topologically non-trivial PC unit cells was used in a supercell. . . 30
2.9 Schematic representation of a single grid cell in the 2D Yee grid before reindexing the sub-grids. The diagram illustrates the field components of the transverse magnetic (TM) mode, including the electric field E_z at the grid points and the magnetic field components H_x and H_y at staggered half-grid positions. 31
2.10 Relative permittivity of InP used in the FDTD simulation. The figure demonstrates a strong agreement between the data published by Pelik and the model implemented in the FDTD simulation. . . 32
2.11 Schematic representation of the FDTD interface transmission simulation setup. Green squares indicate trivial photonic crystal unit cells, while orange squares denote topological photonic crystal unit cells. The interface consists of two photonic crystal regions, each containing $N \times M$ unit cells. The red line represents the electromagnetic field source within the simulation domain. Blue lines indicate monitors T_1 and T_2, positioned K unit cells apart, for recording field data. 34
2.12 Transmission of the topological interface designed by Huag [53] calculated by FDTD method. The oscillations are cause by the finite time windon of the simulation as described in sec. 2.2.2 . . . 35
2.13 Schematic representation of a FDTD band-structure simulation setup. The orange shape represents the photonic crystal unit cell structure, while the pink region denotes the FDTD simulation domain. The purple dashed line indicates the Bloch boundary condition, which determines the position in $\boldsymbol{k}$-space. Red stars mark the randomly selected positions of dipole sources, ensuring excitation of all modes. Blue crosses represent time monitors, which measure the field decay rate to capture the resonant eigenfrequencies. 36
2.14 Schematic representation of the FDTD interface band-structure simulation setup. Orange squares represent topologically non-trivial photonic crystal unit cells, while green squares denote trivial photonic crystal unit cells. The simulation domain consists of $2N \times M$ such cells. In this study, we set $N = 10$ and $M = 5$ to maintain an aspect ratio of approximately 4:1. Twenty dipole sources (red stars) are randomly positioned to excite all modes, and twenty time monitors (blue crosses) are randomly placed to measure the field decay rate. Bloch boundary conditions (purple dashed lines) are applied. 37

2.15 Band structure obtained by FDTD method of the photonic interface designed by Huang [53]. 38

3.1 Visualization of periodic functions from the Bloch form in a photonic crystal composed of dielectric rings arranged in a triangular lattice. Each subfigure (**a**–**l**) represents a different standing wave mode, calculated at the Γ point. The red and blue color gradients indicate phase variations, while the black outlines highlight the structural elements. 42

3.2 Illustration of the role of proper band connection, using a simple photonic crystal system that exhibits a band crossing [81]. The structure is a two-dimensional square lattice of dielectric rods with permittivity $\varepsilon = 7.2$ and radius $r = 0.2a$ in air. **a)** Band structure calculated with MPB, where bands are ordered only by eigenvalue index. An apparent anti-crossing can be seen between the red and green bands along the X–M line. **b)** Magnified view of the possible crossing region. The discrete eigenvalues at each k-point are shown as dots, with the corresponding eigenmodes presented in the (c) panel. **c)** Normalized field patterns of the eigenmodes from b). A symmetry change occurs after the third mode, revealing an incorrect band labeling caused by eigenvalue-only tracking. **d)** Corrected band structure produced by our automated method, which considers both eigenvalue closeness and mode similarity [82]. 43

3.3 Illustration of the ζ path in the Brillouin zone, connecting high-symmetry points Γ, X, and M. The discretized $\boldsymbol{k}$ points along the path are labeled as $k_0, k_1, k_2, \ldots, k_{\max}$. 44

3.4 Flowchart of the band connection algorithm for individual $\boldsymbol{k}$-space segments. The process begins by solving the eigenproblem along the ζ path, selecting the $\boldsymbol{k}$ point with the highest separation S, and constructing an initial set of bands based on the distance d. The mean eigenfunctions are computed iteratively, and bands are updated based on $\bar{d}$. The algorithm repeats until the mean eigenfunctions remain unchanged, indicating convergence. Segments are finally stitched together at shared edge points to reconstruct full bands. 45

3.5 Chern photonic crystal acting as a topological insulator, designed by Blanco [20]. **a)** Geometrical definition of the square unit cell with lattice parameter a, containing a central cylinder with radius r. The material parameters are $\mu_{r,d} = 14$, $\mu_{r,od} = 12.4i$, and $\varepsilon_r = 15$. **b)** Band structure of the photonic crystal with the Chern numbers of the individual bands indicated. 47

3.6 Boundaries of the topological phase $C = (0, 1, -2)$ in the material configuration space of a square lattice photonic crystal with a central cylinder of radius $r = 0.1a$. The size of the dots represents the size of the second photonic band gap (see Fig. 3.5b). The phase does not extend to small values of $\mu_{r,d}$ and $\mu_{r,od}$. 48

3.7 Boundaries of the topological phase $C = (0, 1, -2)$ in the material configuration space of a square lattice photonic crystal with a central cylinder of radius $r = 0.15a$. The size of the dots represents the size of the second photonic band gap (see Fig. 3.5b). Compared to $r = 0.1a$, the topological phase has expanded, but it still does not reach small values of $\mu_{r,d}$ and $\mu_{r,od}$. 51

4.1 Demonstration of eigenfunction amplitude inconsistency in the same mode of a photonic crystal under geometrical variation, obtained using MPB. **a)** The bottom lobe exhibits a higher amplitude. **b)** Both lobes have equal amplitude. **c)** The top lobe exhibits a higher amplitude. In all cases, the underlying symmetry is identical, motivating the use of the sign function. 53

4.2 Flowchart of eigenmode labeling and comparator generation. The eigenproblem is solved at the Γ point for all geometries. Eigenmodes from the mean geometry initialize the comparator set. Each unlabeled eigenmode is compared to the comparators. If the scalar product with a comparator exceeds $\frac{2}{3}r_e^2$, the eigenmode is labeled accordingly. Otherwise, it becomes a new comparator. 55

5.1 Schematic of a photonic crystal composed of rings arranged in a triangular lattice. The design follows the work of Xu [51], which employs a dielectric material with relative permittivity $\varepsilon_r = 9$. The configuration space is defined by the inner radius r_1 and the outer radius r_2 of the rings. 57

5.2 Photonic band gap characteristics of the structure proposed by Xu et al. [51], plotted as a function of the geometric parameters r_1 and r_2. The units of the variables used are given as fractions of the lattice parameter a. Each subplot corresponds to a distinct band gap, indexed by the lower photonic band (a: index 0; b: index 2; c: index 4; d: index 5). The color scale shows the central frequency (gap position) of the band gap in normalized units $\omega a/(2\pi c)$, while the dot size indicates the gap width in the same units. Only non-zero gaps are shown. The diagonal white region corresponds to the geometrical limit where $r_1 = r_2$, representing a vacuum with no structure. Below this limit, the material is inverted, meaning air rings embedded in a dielectric. 57

5.3 Schemes of various 2D photonic crystal square unit cell designs with lattice constant a. **a)** Array of cylinders displaced from a square grid by a distance d, with radius r. **b)** Cylinders positioned on a square grid with varying displacement d, and radius r. **c)** Concentric ring inclusion with inner radius r_1 and outer radius r_2. **d)** Circular sector inclusion with inner radius r_1, outer radius r_2, and an angular span of $\frac{3}{2}\pi$. 58

5.4 Photonic band gap characteristics of the structure defined in Figure 5.3a, shown as a function of the geometric parameters r (cylinder radius) and d (cylinder displacement). The units of the variables used are given as fractions of the lattice parameter a. The plots display the first four band gaps with indices 3, 5, 7, and 8 (band indices start from zero). The color scale represents the central frequency (gap position) in normalized units $\omega a/(2\pi c)$, and the dot size indicates the gap width in the same units. 59
5.5 Photonic band gap characteristics of the structure defined in Figure 5.3c, shown as a function of the geometric parameters r_1 (inner radius) and r_2 (outer radius). Both radii are expressed in normalized units as fractions of the lattice parameter a. The plots display the first four band gaps with indices 3, 5, 7, and 8. The color scale in each panel indicates the central frequency (gap position) in the same normalized units used throughout the work, $\omega a/(2\pi c)$, and the dot size represents the corresponding gap width in these units. The region where $r_1 > r_2$ again corresponds to the material-inverted design described in Figure 5.2. 60
5.6 Analysis of band gap index five for the design defined in Figure 5.3d. **a)** Gap distribution over the parameter space defined by r_1 (inner radius) and r_2 (outer radius). The units of the variables used are given as fractions of the lattice parameter a. **b)** Number of field lobes in the eigenmodes corresponding to the band below the investigated band gap. **c)** Number of field lobes in the eigenmodes corresponding to the band above the investigated band gap. . . . 61
5.7 Demonstration of the use of the *skimage.measure.find_contour* function to identify the number of field lobes in eigenfunctions. **a)** Example where the method successfully detects distinct lobes. **b)** Example where the method fails due to noise or fragmentation of the eigenfunctions. 62
5.8 Use of a clustering algorithm to determine the number of field lobes in an eigenfunction. **a)** Photonic eigenfunction visualized as a 2D probability map, where brighter areas indicate higher probability density. **b)** 1000 points randomly sampled according to the probability distribution from a). **c)** Clustering applied to the sampled points, showing cluster centers (crosses) and standard deviations (circles). **d)** Elbow plot of within-cluster distances versus the number of clusters, indicating 8 as the optimal choice. 63
5.9 Demonstration of the clustering algorithm used for eigenmode classification. Cases **a**, **b**, **c**, **d**, **g**, **h**, and **k** were correctly classified, while the algorithm failed to correctly place the centroids in cases **e**, **f**, **i**, **j**, and **l**. 64
5.10 Use of a local maxima search algorithm for eigenfunction classification. Among all the presented cases, only case **d)** correctly identifies the field lobes. 64
5.11 Examples of eigenfunction classification comparators based on a clustering algorithm, incorporating constraints on the number of field lobes per cluster and accounting for oriented deviation. . . . 65

5.12 **a)** Photonic crystal unit cell design aimed at lowering the energy of the $d_{x^2-y^2}$ mode below that of the two p modes. **b)** The targeted d mode. 65
5.13 Demonstration of the material–field lobe overlap effect based on the design of dielectric rings with four bridging cylinders, as defined in Figure 5.12. **a)** Eigenmode ordering for different values of r_3, with the corresponding unit cell structures shown below each mode. **b)** Band structures of the geometries for varying values of r_3, with the band corresponding to the $d_{x^2-y^2}$ mode highlighted in red. . . 66
5.14 Band-symmetry inversion phase diagram for the ring with cylindrical bridges photonic crystal design defined in Figure 5.12. The color bar indicates the energy separation between the p_x mode and the $d_{x^2-y^2}$ mode at the Γ point. Three slices through the configuration space are shown. Missing values correspond to geometrical configurations where the algorithm described in Section 4.1.4 failed to identify the mode types or the required modes were not present. 68
5.15 Band structure of the design exhibiting the highest degree of band-symmetry inversion and its complementary design, which yields the largest band gap overlap. Both designs are based on the structure defined in Figure 5.12. Regular structure parameters: $[r_1 = 0.025 \cdot a,\ r_2 = 0.325 \cdot a,\ r_3 = 0.06 \cdot a]$; inverted structure parameters: $[r_1 = 0.425 \cdot a,\ r_2 = 0.45 \cdot a,\ r_3 = 0.12 \cdot a]$. The material used is $\mathrm{InP}_{\lambda=1550\ \mathrm{nm}}$, with lattice constant $a = 700$ nm. . 69
5.16 Band structure of a topological interface composed of 20 unit cells of each type defined in Figure 5.15. The two nearly degenerate topological modes are highlighted in red. 70
5.17 Band structure and eigenmode ordering of an interface formed by two geometries resulting in a band-symmetry inverted configuration. Left structure parameters: $[r_1 = 0.4 \cdot a,\ r_2 = 0.45 \cdot a,\ r_3 = 0.12 \cdot a]$; right structure parameters: $[r_1 = 0.425 \cdot a,\ r_2 = 0.45 \cdot a,\ r_3 = 0.06 \cdot a]$. The design parameters are defined in Figure 5.12. The material used is $\mathrm{InP}_{1550\ \mathrm{nm}}$, and the supercell forming the interface consists of 15 unit cells of each geometry type. A boundary between crystals belonging to the same topology class does not host in-gap modes. Therefore, the observed in-gap modes are not defect-related but topological. 71
5.18 Demonstration of a photonic crystal with a lattice parameter ratio of 3:2 between the two structures. 72
5.19 Band structure of a photonic crystal with a lattice parameter ratio of 3:2. The regular structure parameters are $[r_1 = 0.175 \cdot a,\ r_2 = 0.25 \cdot a,\ r_3 = 0.04 \cdot a]$, while the inverted structure parameters are $[r_1 = 0.425 \cdot a,\ r_2 = 0.45 \cdot a,\ r_3 = 0.14 \cdot a]$. The interface consists of five unit cell columns of each type. For lattice constants $a_{\mathrm{regular}} = 750$ nm and $a_{\mathrm{inverted}} = 500$ nm, and using $\mathrm{InP}_{1200\mathrm{nm}}$ as the material, the resulting common band gap spans from 1000 nm to 1270 nm. 73

5.20 Band structure and eigenmode ordering of an interface formed by two geometries resulting in a band-symmetry inverted configuration. Left structure parameters: $[r_1 = 0.375 \cdot a,\ r_2 = 0.4 \cdot a,\ r_3 = 0.12 \cdot a]$; right structure parameters: $[r_1 = 0.425 \cdot a,\ r_2 = 0.45 \cdot a,\ r_3 = 0.12 \cdot a]$. The design parameters are defined in Figure 5.12. The material used is $\mathrm{InP}_{1550\ \mathrm{nm}}$. 74
5.21 Four independent optimization runs of the same target configuration. Panels a)–d) show different but related dielectric patterns, illustrating that the algorithm is not fully stable and converges to distinct local optima. The white regions correspond to air, while the dark gray areas represent the high-permittivity material. . . . 76

6.1 **a)** definition of geometrical parameters of the bridged ring design. **b)** Example of a seed state which can lead to a topologically trivial or non-trivial case, depending on the way of tuning the geometrical parameters. 78
6.2 Band structure of the design exhibiting the highest degree of band-symmetry inversion and its complementary design, which yields the largest band gap overlap with restriction $r_1 = r_2$ for the inverted structure. The pattern corresponds to the bridged ring design defined in 6.1. Regular structure parameters: $[r_1 = 0.1 \cdot a,\ r_2 = 0.275 \cdot a,\ r_3 = 0.06 \cdot a]$; inverted structure parameters: $[r_1 = 0.5 \cdot a,\ r_2 = 0.5 \cdot a,\ r_3 = 0.14 \cdot a]$. The material used is $\mathrm{InP}_{1550\ \mathrm{nm}}$. 78
6.3 Band structure of a topological interface composed of 16 unit cells of each type defined in Figure 6.2 The two nearly degenerate topological modes are highlighted in magenta, while the original bad-gap is depicted in pink. The mode dispersion detail reveals abnormal dispersion slope. 79
6.4 Band structure of the design that produces topologically non-trivial interface, but produces narrower band-gap then the design in figure 6.2. The pattern corresponds to the bridged ring design defined in 6.1. Regular structure parameters: $[r_1 = 0.105 \cdot a,\ r_2 = 0.35 \cdot a,\ r_3 = 0.072 \cdot a]$; inverted structure parameters: $[r_1 = 0.345 \cdot a,\ r_2 = 0.425 \cdot a,\ r_3 = 0.108 \cdot a]$. The material used is $\mathrm{InP}_{1550\ \mathrm{nm}}$. 80
6.5 **a)** Band structure of a topological interface composed of 16 unit cells of each type defined in Figure 6.4 The two nearly degenerate topological modes are highlighted in magenta, while the original bad-gap is depicted in pink. The mode dispersion detail reveals regular dispersion slope. **b)** Transmission of the interface calculated by the FDTD method. 81
6.6 Wilson spectra of the set of bands below the photonic band gap of the PC design introduced in figure 6.4. The flat but displaced bands indicate the obstructed atomic limit topological effect. . . . 82

6.7 Interface modes and Wilson loop analysis for three photonic crystal combinations. Each column corresponds to an interface formed by joining two photonic crystals with distinct unit cell parameters, denoted as Left PC and Right PC. Top row: Interface band structures computed using a supercell geometry. Gap-localized modes are observed only in case b). Middle and bottom rows: Wilson loop spectra for the left and right photonic crystals forming each interface, respectively, calculated for the photonic bands below the band gap. Case a) shows an interface between two trivial configurations with matching Wilson loops and no interface modes. Case b) corresponds to a mismatch between a trivial and an obstructed atomic limit phase, indicated by a shift in the Wilson loop; this results in a pair of interface-localized modes within the band gap. Case c) involves two OAL phases with identical Wannier center positions and therefore no protected interface modes. This analysis demonstrates that the presence of localized interface states originates from a polarization mismatch between the adjoining bulk phases. 83
6.8 Schematic representation of supercell configurations used to simulate topological interfaces. **a)** An original supercell arrangement with one interface placed at the center and a second appearing at the boundary due to periodicity. **b)** Modified supercell with both interfaces symmetrically located within the cell, allowing for clearer analysis of interface-localized modes. **c)** Enclosed configuration where photonic crystal A is embedded in PC B, showing how the same topological mode (Mode 1) propagates in opposite directions depending on the orientation of the interface. 84
6.9 Dependence of mode localization on the number of photonic crystal unit cells between topological interfaces. **a)** *First topological mode*: Bloch mode profile magnitude (summed over the transverse direction) plotted along the position between two interfaces for various numbers of unit cells N, color-coded from 1 to 10. As N increases, the mode transitions from being spread over both interfaces to being localized predominantly around one. **b,c)** *Second topological mode*: Field distribution for **(b)** $N = 6$, showing the mode extends over both interfaces, indicating lack of unidirectionality, and **(c)** $N = 14$, where the mode is fully localized at Interface 2, demonstrating unidirectional propagation consistent with a topologically protected state. 86
6.10 Directionality of the first topological mode as a function of the number of unit cells N between two interfaces. The supercell (defined in Fig.6.8b) is divided into two spatial regions: one containing Interface 1 (first half of the x-axis) and the other containing Interface 2 (second half of the x-axis). The blue points indicate the fraction of the total field energy located around Interface 1, corresponding to forward propagation, while the red points indicate the energy near Interface 2, corresponding to backward propagation. The design is based on the one shown in Fig.6.4. 87

6.11 Standard deviation (STD) of the field distribution for the first topological mode in the upper band channel as a function of the number of unit cells N. Clockwise (blue) and counter-clockwise (red) components correspond to regions around Interfaces 1 and 2, respectively. 87
6.12 Band structure evolution for different numbers of unit cells N in the supercell, showing the convergence of the topological modes in the upper band channel. As N increases from 1 to 10, the initially split topological bands gradually merge and become nearly degenerate around $N = 6$, indicating stabilization of the mode frequency. . . 88
6.13 Large-scale interface perturbation simulations. Each panel shows the E_z field profile obtained from FDTD simulations, illustrating mode propagation along the perturbed interface using the color scale. The black–white inset in the upper right corner of each panel represents the unit cell distribution, where white indicates topologically trivial cells and black indicates topologically non-trivial (inverted) ones. The defect interfaces consist of 20×25 unit cells, while the turn interfaces consist of 40×40 unit cells. The unit cell design used here is the one introduced in Fig. 6.4. Panels (a–d) test different interface configurations, including 90° turns to the left and right, as well as replacements of three cells one cell away from the interface with the opposite topological type. 90
6.14 Transmission spectra of the geometries shown in Fig. 6.13, including the straight undisturbed interface for reference. The results are qualitative rather than quantitative, as discussed in Sec. 2.2.2, which explains why some values exceed 100%. The relevant information is the transmission level around which the data oscillate. 91
6.15 A set of defect configurations placed relative to the center of the interface. Panel (a) shows the resulting transmission spectra, which exhibit the same qualitative behavior as in the previous figure. Panel (b) illustrates the corresponding defect geometries. The designs of the trivial and topological unit cells are identical to those introduced in Fig. 6.4 and Fig. 6.13. The defects are made of the same material as the surrounding photonic crystal. 92
6.16 E_z field profile obtained from FDTD simulation at a wavelength of 1550 nm, showing the mode propagation along the topological interface. The interface separates the topologically trivial (left) and non-trivial (right) photonic crystal regions. 93
6.17 Illustration of the geometry interpolation scheme used to define a continuous path between the trivial and topological phases in the inversion diagram (Fig. 5.14). The line connecting V_{max} and V_{min} represents a gradual transformation from the topological to the trivial geometry through band-gap closure and reopening. The intermediate geometries V_1 and V_2 correspond to points along this line, parameterized by the mixing coefficient $M \in [0, 1]$, which determines their position between the two end points. The figure serves only as a conceptual demonstration and does not represent precise point placement. 95

6.18 Dependence of the maximum dispersion slope of the topological edge mode on the size of the band-gap overlap for geometry pairs defined by the mixing coefficient $M \in [0.75, 1]$. The end points $V_{min} = [0.425, 0.45, 0.12]$ and $V_{max} = [0.025, 0.325, 0.06]$ correspond to the configurations with the highest band-gap inversion and the highest band-gap overlap. The observed trend shows a monotonic decrease of the dispersion slope with increasing band-gap size. . . 95

6.19 Dependence of the $\Gamma - N$ energy difference on band-gap size for several interface designs. The vertical axis shows the energy difference $\Delta E_{\Gamma\text{–}N} \equiv E(\Gamma) - E(N)$ of the relevant band (in normalized-frequency units). The horizontal axis is the band-gap size $[a/\lambda]$. Points are colored by the mixing value used to linearly interpolate between the inverted and regular unit cells (0.70–1.00); the horizontal dashed line denotes $\Delta E_{\Gamma\text{–}N} = 0$. All structures use indium phosphide [120]. **a)** Interface from Fig. 5.12: inverted ($r_1 = 0.425a,\ r_2 = 0.45a,\ r_3 = 0.12a$) vs. regular ($r_1 = 0.025a,\ r_2 = 0.325a,\ r_3 = 0.06a$); this pair yields the largest band-gap overlap. **b)** Fabrication-simplified variant with cylinders replacing rings: inverted ($r_1 = 0.5a,\ r_2 = 0.5a,\ r_3 = 0.14a$) vs. regular ($r_1 = 0.1a,\ r_2 = 0.275a,\ r_3 = 0.06a$). **c)** Interface derived from a hexagonal (C_6) lattice [51]: inverted ($r_1 = 0.38a,\ r_2 = 0.45a$) vs. regular ($r_1 = 0.27a,\ r_2 = 0.36a$) 96

List of Abbreviations

OAL	Obstructed Atomic Limit
PC	Photonic Crystal
TE	Transverse Electric
TM	Transverse Magnetic
TRS	Time-Reversal Symmetry
BZ	Brillouin Zone
MPB	MIT Photonic Bands
FDTD	Finite Difference Time Domain
PML	Perfectly Matched Layer
InP	Indium Phosphide
GUI	Graphical User Interface
2DTI	Two dimensional topological insulator
YIG	Yttrium iron garnet
TBM	Tight-binding Model
STD	Standard deviation
irrep	Irreducible representation

List of Publications

1. Xia, Shuang; Ignatyeva, Daria O; Liu, Qing; Wang, Hanbin; Yang, Weihao; Qin, Jun; Chen, Yiqin; Duan, Huigao; Luo, Yi; Novák, Ondřej, et al. Circular displacement current induced anomalous magneto-optical effects in high index Mie resonators. *Laser & Photonics Reviews*. 2022, vol. 16, no. 8, p. 2200067.
2. Novák, Ondřej; Veis, Martin; Herranz, Gervasi. Obstructed atomic limit topological protection in C4-symmetricphotonic crystals for optical communications. *Journal of Optics*. 2025.
3. Novák, Ondřej; Herranz, Gervasi; Veis, Martin. Methodology for Topological Interface Engineering in 2D Photonic Crystals. *Advanced Photonics Research*. 2025, e202500135.